ADVANCED METASURFACE DESIGN AND INTEGRATION FOR ELECTROMAGNETIC SYSTEMS

by

Kristy Alexandra Hecht

A dissertation submitted to the faculty of
The University of North Carolina at Charlotte
in partial fulfillment of the requirements
for the degree of Doctor of Philosophy in
Electrical Engineering

Charlotte

2023

Approved by:

Dr. Mario Junior Mencagli

Dr. Tino Hofmann

Dr. Mike Fiddy

Dr. Aidan Browne

ABSTRACT

KRISTY ALEXANDRA HECHT. Advanced Metasurface Design and Integration for Electromagnetic Systems. (Under the direction of DR. MARIO JUNIOR MENCAGLI)

In the realm of metamaterials and electromagnetic engineering, a metasurface is a two-dimensional array of subwavelength-scale structures meticulously engineered to manipulate electromagnetic waves. Unlike conventional bulky optical elements, metasurfaces represent a novel approach, providing ultra-compact, planar solutions capable of controlling the wave's phase, amplitude, and polarization across a broad spectrum. This transformative technology finds multifaceted applications, spanning from high-efficiency optical devices and advanced imaging systems to next-generation communication systems and sensing platforms.

Within the context of this dissertation, I delve into four different designs and applications of metasurface research, each poised to push the boundaries of electromagnetic engineering. These include a metascreen, two antennas, and a time-varying capacitor, each contributing to the evolving landscape of metasurface technologies.

One of the pivotal contributions explored in this research is the development of a dual-polarization metascreen. This innovation holds significant importance in the realm of electromagnetic engineering and communication systems. A dual-polarization metascreen, capable of manipulating both horizontal and vertical polarizations of electromagnetic waves simultaneously, unlocks a range of practical advantages. Firstly, it enables versatile control over the polarization state of transmitted or received signals, making it invaluable for applications such as radar systems, where the ability to switch between polarizations rapidly can enhance target detection and tracking. Moreover, in wireless communication, dual-polarization metascreens offer increased spectral efficiency by accommodating multiple data streams through polarization multiplexing. This results in improved data rates and network capacity. Additionally,

these metascreens find applications in satellite communication and remote sensing, where the capability to simultaneously capture diverse polarizations enhances data acquisition and accuracy. In essence, the development and implementation of dual-polarization metascreens pave the way for advanced and versatile electromagnetic systems with enhanced performance and capabilities.

Building upon the breakthrough of dual-polarization metascreens, the subsequent chapter in this dissertation embarks on the exploration of a dual-layered, Ka and W band sinusoidally modulated antenna. These frequency bands, while individually vital, have never been addressed together in a single antenna design. This novel approach ventures into uncharted territory, as the integration of dual-band functionality across these relatively far-apart frequencies presents unique challenges and opportunities. This research breaks new ground by delving into the intricate design, characterization, and implementation of such dual-band metasurface antennas, making significant contributions to the advancement of connectivity technology and broader applications in radar systems, remote sensing, and millimeter-wave technologies. The exploration of this territory not only expands the boundaries of electromagnetic engineering but also holds the promise of unlocking new capabilities for advanced communication and sensing systems, thereby solidifying the progressive trajectory of metasurface technologies in the field.

Furthermore, another sinusoidally modulated antenna examined within this dissertation provides valuable insights into the calculation of dispersion characteristics for a 3D printable antenna. The rapid calculation of dispersion curves and the swift fabrication of antennas through 3D printing are pivotal advancements in the field of electromagnetic engineering. Calculating dispersion curves efficiently allows for comprehensive characterization of the propagation properties of electromagnetic waves within various materials and structures. Conversely, 3D printing offers a fast and cost-effective method for prototyping and manufacturing antennas with intricate ge-

ometries and tailored properties. This rapid turnaround time accelerates the research and development process, fostering innovation and enabling the swift deployment of custom-designed antennas for emerging technologies. Together, the expedited dispersion curve calculations and 3D printing capabilities seamlessly streamline the antenna design process, thereby propelling advancements in communication, sensing, and connectivity technologies. This approach to antenna research underscores the interdisciplinary nature of this dissertation and its significant contributions to the evolving field of electromagnetic engineering.

As we delve further into the realms of electromagnetics and photonics research, one of the forefront areas involves the study of structures with time-varying parameters, such as permittivity and permeability. This exploration of time as a new degree of freedom for controlling electromagnetic waves has yielded structures with fascinating functionalities, including time-Floquet topological insulators, temporal-based nonreciprocity, and static-to-dynamic field conversion. These innovations have addressed challenges faced by time-invariant structures, promising new avenues for wave-matter interactions. Recently, the fusion of time-varying media with the concept of metamaterials has opened another intriguing pathway to control and achieve desired functionalities in electromagnetic systems. This work, however, focuses on a specific subset of time-varying media, namely time-varying networks composed of lumped elements like resistors, capacitors, and inductors with time-dependent properties. These networks offer an accessible platform for experimental demonstrations and have sparked significant research interest. While previous studies predominantly explored periodically modulated lumped elements, this work introduces a novel approach employing aperiodic time modulation of a single capacitor to capture the energy of arbitrary pulses. This advancement addresses practical challenges and significantly expands the potential applications of time-varying lumped elements in electromagnetic energy accumulation, highlighting the interdisciplinary and innovative spirit that drives

research in this field.

In summary, this dissertation represents a comprehensive exploration of diverse aspects within the field of electromagnetic engineering and photonics. From the development of advanced metasurface technologies and their applications in communication and sensing systems to the utilization of time-varying media for innovative energy accumulation techniques, this research underscores the multifaceted nature of contemporary electromagnetics and photonics. Through theoretical analysis and innovative design, this work not only contributes to the academic understanding of these fields but also holds the potential to catalyze technological advancements with far-reaching implications.

DEDICATION

I dedicate this dissertation to my puppies, Azalea and Baloo, and Cereal, the best desk cat.

ACKNOWLEDGEMENTS

I would like to express my deep gratitude and appreciation to the many individuals and organizations that have contributed to the completion of this Ph.D. dissertation. This journey has been a transformative and enriching experience, and I am sincerely thankful to all those who have supported and guided me along the way.

I would like to extend my heartfelt thanks to the members of my dissertation committee, Dr. Mike Fiddy, Dr. Tino Hofmann, and Dr. Aidan Browne, for their insightful feedback and critical evaluation of this work. Your collective expertise has helped refine and strengthen this research and my abilities as a presenter and writer.

I am grateful to my colleagues and fellow researchers, Nacer Chahat, Gaurangi Gupta, and Goutam Chattopadhyay at Jet Propulsion Laboratory for their discussions, collaboration, and support. I am also thankful for the opportunities presented to me from our collaborative efforts.

I want to express my appreciation to all my friends who have stood by me, offering emotional support and letting me rant about my cool antennas to you. Your encouragement has been a source of motivation and inspiration.

To my partner, Charles Layman, I extend my deepest gratitude for your unwavering love, encouragement, and understanding that have sustained me through the challenges of this doctoral journey. Throughout this journey, you have been putting up with the long and often unpredictable hours I have worked and the high-stress situations I have encountered. I appreciate your unwavering support ensuring I had the opportunity to pursue every academic endeavor that came my way. Your support has been invaluable.

I am deeply indebted to my advisor, Dr. Mario Junior Mencagli, whose unwavering support, guidance, and mentorship have been invaluable throughout this research journey. Your expertise, patience, and dedication to my academic and personal growth have played a pivotal role in shaping this dissertation. There are no words

that can fully express how much I appreciate your guidance, both academically and personally. You have consistently pushed me out of my comfort zone, challenging me to take on new and sometimes uncomfortable situations, such as presenting at international conferences alone. These experiences have contributed immeasurably to my personal and professional development. Thanks to your mentorship, I have grown in confidence and competence, far beyond what I could have achieved on my own. Embarking on both my Master's and Ph.D. under your guidance has been an extraordinary and transformative experience. I am profoundly grateful for the knowledge and wisdom you have shared and for the unwavering belief you have had in my potential. Thank you, Dr. Mario, for your exceptional mentorship and for being an inspiring role model. I will be forever grateful for the privilege of learning and growing under your guidance.

This dissertation represents the culmination of years of dedication and hard work, and I am deeply grateful to everyone who has played a role in its realization. Thank you for believing in me and for being part of this significant milestone in my academic journey.

TABLE OF CONTENTS

LIST OF FIGURES

LIST OF SYMBOLS

ϵ	A symbol for permitivity
η	A symbol for characteristic impedance
μ	A symbol for permeability
μm	An abbreviation for micrometers
∇	A symbol for del operator
Ω	A symbol for ohms
ϕ	A symbol for phi
ρ	A symbol for rho
θ	A symbol for theta
dB	An abbreviation for decibels
deg	An abbreviation for degrees
EM	An abbreviation for electromagnetic
GHz	An abbreviation for Gigahertz
Hz	An abbreviation for Hertz
IBC	An acronym for Impedance Boundary Conditions
m	An abbreviation for meters
mm	An abbreviation for millimeter
MTS	An abbreviation for metasurface
PEC	An acronym for Perfect Electric Conductor

PMC An acronym for Perfect Magnetic Conductor

rad An abbreviation for radians

RF An acronym for Radio Frequency

S An abbreviation for Siemens

TE An acronym for Transverse Electric

TM An acronym for Transverse Magnetic

X_s A symbol for surface reactance

Z_s A symbol for surface impedance

CHAPTER 1: INTRODUCTION

Metamaterials are specially engineered materials that exhibit properties not found in naturally occurring substances. The concept of an electromagnetic metamaterial was first introduced by Viktor G. Veselago in 1968 [2], who proposed the idea of a material with negative permittivity and permeability, often referred to as a "left-handed" material. However, it was not until many decades later that John Pendry developed a theoretical framework for determining the effective permittivity of a material using microstructures made from non-magnetic sheets [3]. This work provided a foundation for understanding how to create materials with unique electromagnetic properties. A significant milestone in the field of metamaterials occurred in 2001 when D. R. Smith achieved the physical realization of a material with a negative refractive index by employing split ring resonators [4]. This groundbreaking experiment marked the first successful creation of an electromagnetic metamaterial.

Metamaterials have inspired a two-dimensional counterpart known as metasurfaces (MTSs), a concept originally proposed by Oliner in 1959 [5]. Oliner introduced the idea of a sinusoidally modulated surface impedance, which laid the foundation for the development of metasurfaces. In recent years, metasurfaces have gained significant attention due to their versatility and the advantage of being low profile and lightweight. A metasurface structure is comprised of periodic, sub-wavelength elements that collectively create a surface impedance capable of manipulating incident waves. This manipulation can involve controlling the amplitude, phase, or polarization of the waves. The exploration of metasurfaces, particularly at millimeter wavelengths, has been on the rise. They offer a range of benefits, setting them apart from other electromagnetic devices, such as phased arrays. As a result, there is growing interest in

employing metasurfaces in various applications, including space technology, communication systems, flat optical components, energy harvesting, and terahertz devices.

There are three distinct approaches to designing MTS for controlling electromagnetic waves: aperture antennas, wavefront control, and transmission field control. Aperture antennas have been extensively explored for various applications. For instance, in the work by Sievenpiper et al. [6], an innovative approach is presented, leveraging the holographic principle to design artificial surface impedance. Another method for designing MTS antennas is described in Maci's research [7], which offers a closed-form approach to design circularly polarized spiral leaky wave antennas. Additionally, aperture antennas can be utilized to create isoflux shaped beams with polarization control, as demonstrated in [8]. The utilization of MTS for aperture antennas presents several advantages over traditional methods, addressing common design challenges. These benefits include improved aperture efficiency, enhanced polarization purity, and the ability to shape the radiation beam. Notably, one of the key advantages of aperture antennas with MTSs is their integrated feed system. Unlike conventional antennas that require an external feed system, adding weight and complexity, these antennas can be excited using a simple coaxial excitation or a waveguide typically placed at the center of the antenna. This feed system excites a wave that couples the surface wave to the surface impedance, exciting a transverse magnetic (TM) wave. The power of the surface wave is then gradually modulated, allowing for controlled leakage by exciting the -1 indexed Floquet mode. These modulations are achieved through variations in the size or angle of the subwavelength metallic patches.

Another type of application is designing a MTS in order to control the wavefront of the surface wave (SW). One such application involves the creation of a Luneberg lens, which can be achieved more efficiently and cost-effectively using MTSs compared to the traditional method of layering dielectrics [9]. Several approaches can be taken

to design a Luneberg lens with a MTS. One method involves altering the effective permittivity through small cavities inside a parallel plate waveguide [10, 11, 12]. Another approach is to modify the surface impedance using metallic posts [13, 14]. Additionally, a Luneberg lens can be achieved with MTSs by adjusting the equivalent boundary conditions for one wall of the parallel plate waveguide through changes in the geometrical parameters of the metallic cladding [15]. The control of a wavefront can be extended to MTSs utilizing specific materials, such as antimony sulfide [16] and graphene [17], which offer the advantage of tunability.

A MTS can also be designed to function as a screen for controlling the transmission field. One effective approach to achieve this is by employing a three-layer configuration of unit cells. Each layer is engineered with specific impedance or phase properties that interact with the incident wave, resulting in transformations of its polarization [18]. This technique has been instrumental in various applications, including controlling light transmission over subwavelength distances [19], beam steering [20, 21], and other spatial wave transformations. The three-layer approach has gained prominence due to its versatility. Each layer introduces additional design parameters, thereby increasing the degrees of freedom and enabling precise control over the reflection and transmission of the incident wave.

Leveraging the distinctive properties of metasurfaces, antennas have emerged as a promising avenue for transforming various applications in electromagnetic wave manipulation. The unique attributes and engineered structures of metasurfaces provide an unprecedented level of control over incident wave properties, including amplitude, phase, and polarization. This capability allows for the creation of compact, lightweight, and highly efficient antenna systems. The fine-grained control of electromagnetic waves at the subwavelength scale opens up exciting possibilities across numerous fields.

The objective of this dissertation is to make a meaningful contribution to the ex-

panding body of knowledge in this domain. Through a combination of innovative design methodologies, theoretical analyses, and practical implementations, this research seeks to advance the comprehension of metasurface antenna performance and its diverse applications. Comprehensive studies and numerical simulations are integral components of this effort, aimed at furthering the understanding of metasurface antennas and their real-world potential.

CHAPTER 2: CONTRIBUTION

Metasurfaces (MTSs), a two-dimensional (2D) version of metamaterials, have gained significant attention in recent years. They provide unprecedented degrees of freedom in controlling and manipulating electromagnetic waves with low profile, low weight, planar structures. MTSs are composed of periodic, sub-wavelength elements that manipulate incident waves by controlling their amplitude, phase, or polarization. In the microwave and millimeter-wave range, MTSs usually consist of a collection of metallic and/or dielectric textures arranged in a regular lattice. This dissertation focuses on four different and innovative projects that push the boundaries of current research of such MTSs. The findings of these projects may find applications in wireless communications, imaging, sensing, Earth science, and more.

While existing metascreens consisting of a stack of three MTSs have demonstrated the ability to manipulate a single incident wave, the proposed metascreen pushes the boundaries by enabling the manipulation of two distinct types of waves simultaneously. I designed and numerically tested a metascreen capable of steering at two different arbitrary angles coming from two orthogonally polarized incident waves. By expanding the capabilities of metasurfaces to independently control two orthogonally polarized waves, a wide range of new applications become possible such as for imaging systems and radars in applications such as concealed weapons detection, automotive collision avoidance, missile guidance, and satellite tracking [22, 23]. By incorporating this novel metascreen into such applications, it can achieve enhanced functionality, improved performance, and greater versatility. In addition to the expanded range of applications, the proposed metascreen offers practical advantages in terms of weight and complexity reduction. By integrating the capability to independently manipu-

late two orthogonal waves into a single flat structure, the need for multiple separate metascreens is eliminated. This reduction in the number of required metasurfaces not only simplifies the overall system design but also leads to a significant reduction in weight and complexity.

The second project focuses on a dual-layered MTS antenna capable of operating at two significantly different frequencies. Dual-frequency MTS antennas have been studied in literature, but the frequencies covered by existing designs are usually within a limited range. Previous approaches involve superimposing two different modulated surface impedances or cascading two surface impedances obtained through optimization techniques. However, these methods face challenges in discretizing continuous impedance profiles accurately or require external excitation, leading to poor device form factors. My proposed antenna overcomes these limitations by leveraging Foster's reactance theorem to independently control the performance of each layer, enabling operation at widely separated frequencies excited with co-planar feed. This cutting-edge technology opens up new possibilities in the field of multi-frequency antennas with large frequency separations with finalized integration into space mission technology. The antenna proposed breaks new ground in the field by exploiting Foster's reactance theorem to isolate the performance of each layer and enable dual-frequency operation across a significantly broader frequency range.

The final antenna that I propose incorporates commonly available 3D printing materials, making it highly accessible for design and manufacturing purposes. Through the utilization of a numerical design approach, the antenna can be numerically designed swiftly, taking only a matter of seconds. This approach addresses the limitations posed by time constraints and restricted access to conventional fabrication methods. The time-saving aspect of this approach is particularly beneficial during the initial design phase, as it enables rapid design and adjustments to the antenna's parameters and overall structure. Moreover, the antenna's design is specifically tai-

lored to be compatible with any commercially accessible 3D printer, ensuring ease, speed, and cost-effectiveness in the fabrication process. This feature eliminates the need for specialized equipment or complex manufacturing procedures, making the antenna readily available for all uses.

The final project presented examines the analysis of a time varying capacitor for energy trapping applications. Time-varying media offer intriguing functionalities that surpass the limitations of time-invariant structures. Combining the concept of time-varying media with metamaterials has opened up new possibilities for controlling wave-matter interaction. While most studies have focused on periodically modulated lumped elements, aperiodic time modulation of these elements can provide an additional degree of freedom to engineer networks with novel functionalities. In particular, this work addresses the use of time-varying lumped elements for electromagnetic energy accumulation. Previous approaches have demonstrated the absorption of incoming signals by modulating reactive elements, such as capacitors and inductors. However, these approaches often require extreme values of capacitance, including negative values, which may be challenging to achieve in practice. To overcome this limitation, a proposed approach involves applying non-periodic modulation to a single capacitor at the end of a transmission line. By combining an incoming pulse with a DC signal, the extreme capacitance values can be avoided. The study explores the reasons behind the challenges faced by previous approaches and demonstrates how the combination of pulse and DC signal enables the capture of energy.

CHAPTER 3: DESIGN OF METASURFACES

Metasurfaces are fascinating structures that have gained significant attention in recent years due to their unique ability to control electromagnetic waves at sub-wavelength scales. These planar metamaterials consist of a periodic arrangement of unit cells, which are typically much smaller than the operating wavelength of the incident wave. By carefully designing the geometry and composition of these unit cells, MTSs can manipulate various properties of electromagnetic waves, including polarization, phase, and direction of propagation. One of the key advantages of MTSs is their ability to impose impedance boundary conditions (IBC) on the electric and magnetic fields. These boundary conditions govern the interaction of electromagnetic waves with the MTS, allowing for precise control over the reflection, transmission, and scattering of the incident waves. By engineering the impedance properties of the individual metasurfaces, it is possible to achieve different functionalities and tailor the electromagnetic response according to specific requirements. To fully understand and characterize the electromagnetic behavior of periodic planar MTSs, various analytical techniques are employed to apply Maxwell's equations to solve for the scattering and reflection properties of the MTSs. Analytical models and numerical methods, such as the method of moments, finite element analysis, and rigorous coupled-wave analysis, are commonly used to study the interaction between incident waves and metasurfaces. This chapter will explore the physics and mathematical background needed to design metasurface antennas.

In the analysis and design of MTSs, several assumptions are commonly made to simplify the calculations. One key assumption is the concept of local periodicity, as illustrated in Fig. 3.1. This concept is employed to describe the analysis of a unit cell,

which serves as the fundamental building block of the periodic structure. The local periodicity assumption enables the analysis of a single unit cell through the consideration that this unit cell is replicated infinitely in both the x and y directions. This simplifying assumption is justifiable because, when extended to the entire antenna structure, the variations in the unit cell's geometry between adjacent unit cells are small enough to uphold the assumption's validity.

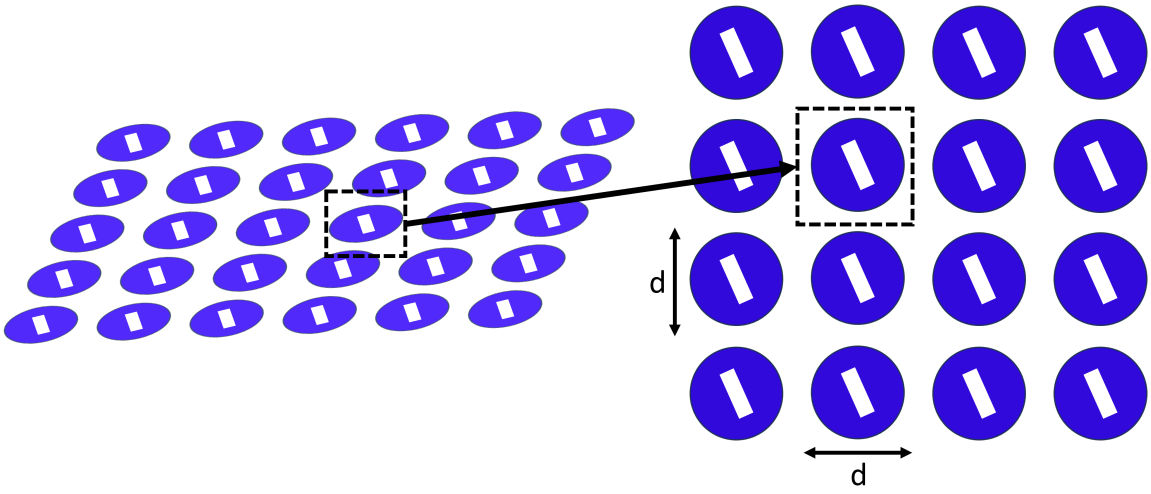

Figure 3.1: The concept of the local periodicity assumption in the analysis of metasurfaces, enabling the examination of dispersion characteristics within a single unit cell. By introducing a phase gradient ranging from 0 to π rad across parallel sides of the unit cell, it becomes possible to investigate the impedance behavior. This assumption remains valid due to the gradual transitions present within the metasurface structure. These gradual changes ensure that variations between neighboring unit cells remain sufficiently minimal, thereby preserving the precision of the analysis.

The unit cell analysis involves imposing a phase delay across two parallel walls, ranging from 0 to π rad. The resulting dispersion curve from the phase analysis establishes a relationship between the phase and the frequency for a specific variation of the unit cell's geometry. Extrapolating from this dispersion curve provides the impedance at a specific frequency. To encompass a comprehensive range of impedance values achievable by the unit cell, the dispersion analysis is conducted across various geometric variations of the unit cell. In this manner, the analysis based on the local periodicity assumption and their resulting dispersion curves facilitates the impedance

characteristics over a spectrum of a large range geometrical variations for a chosen frequency.

Another commonly employed assumption involves focusing on the dominant Floquet modes. These modes are characterized by their significant contributions to the overall behavior of the metasurface. By concentrating the analysis on the zeroth-order Floquet mode, where $n = m = 0$, the fields and boundary conditions can be homogenized, leading to a simplification of computation. This simplification streamlines the analysis of the metasurface making it more manageable.

With a homogenized, periodic structure, the Floquet-Bloch theorem can be incorporated for analysis. The Floquet-Bloch theorem is a fundamental concept used to study periodic differential equations and their application in understanding these structures. The theorem facilitates the representation of fields within a periodic structure through a linear combination of Bloch waves. These Bloch waves are essentially plane waves modulated by a periodic function, effectively encapsulating the periodic nature of the structure. By leveraging the Floquet-Bloch theorem, it becomes possible to extract dispersion relations of periodic structures to help realize the surface impedance. This theorem serves as a crucial tool for comprehending how periodic structures interact with electromagnetic waves and will be discussed in detail in section 3.1.

Transitioning from the section on periodic differential equation, the focus will shift towards surface impedance characterization and surface wave dispersion characteristics. Surface impedance refers to the effective impedance that an electromagnetic wave encounters at the boundary of a material or structure. This characteristic has a pivotal influence in dictating how the interface reflects, transmits, or absorbs electromagnetic waves. The comprehension of surface impedance underpins the capacity to craft and fine-tune structures engineered to manipulate the behavior of electromagnetic waves at their interface. Concurrently, the examination of surface wave

dispersion characteristics unfolds. These surface waves, which traverse along the interface between the interfaces of medium, possess a dispersion relation linking their wavevector and frequency.

The final section of this chapter hones in on the type of impedance the surface wave experiences defined by the impedance boundary conditions (IBCs). The surface impedance can be designed to either exhibit isotropic or anisotropic surface impedance. An isotropic metasurface maintains consistent constitutive properties, such as permittivity and permeability, in all directions. This uniform behavior is captured by a constant or can also be described with a unity tensor, making it invariant to incident wave's direction. On the contrasting side, anisotropic modulated metasurfaces emerge with properties that are directionally dependent. These properties are described through an impedance tensor, as they can vary across different directions. This anisotropic design bestows a higher degree of control over electromagnetic waves. The result is enhanced efficiency and the ability to achieve specific functionalities with tailored precision.

Overall, the following three sections within this chapter provide a comprehensive overview of the analysis of periodic structures using the Floquet-Bloch theorem, the characterization of surface impedance and surface wave dispersion characteristics, and the distinctions between isotropic and anisotropic modulated metasurfaces for impedance boundary conditions.

3.1 Floquet-Bloch Theorem For Describing Periodic Structures

In the late 19^{th} century, mathematician Gaston Floquet made significant contributions to the field by publishing his research and derivation for solving one-dimensional differential equations with periodic coefficients [24]. His work provided a mathematical framework for analyzing one-dimensional systems with periodic properties. A periodic structure is one that exhibits periodic expansion in a defined direction, characterized by variations in shape, size, and material properties. Periodicity represents

a fundamental concept in various fields, ranging from electromagnetics to mechanics and crystallography. Almost fifty years after Floquet published his research on one-dimensional periodic differential equations, Felix Bloch further advanced Floquet's work by extending it to three-dimensional systems, specifically focusing on electrons traveling across periodic crystal lattices [25]. Bloch's seminal work revealed that the solution for a three-dimensional periodic function can be expressed as the product of a plane wave and a periodic function, with both components sharing the same periodicity as the lattice. This mathematical framework is particularly useful when studying the behavior of electrons in crystal lattices, where Bloch wave functions provide a comprehensive description of their periodic properties and behavior. The contributions of Floquet and Bloch have had a profound impact on the understanding of periodic structures and their mathematical analysis. Their works serve as pillars in the study of various physical phenomena, facilitating the exploration of electromagnetic waves, mechanical systems, and quantum mechanics in periodic structures.

With this historical groundwork in mind, the discussion shifts toward an exploration of the concept of an infinite structure characterized by a spatial periodicity designated as D_x along the x axis of a Cartesian coordinate system. This structure is represented by a wave vector (k_x^i, k_y^i, k_z^i), which serves as the embodiment of a plane wave. Within this structure, the diffraction phenomenon unfolds between two clearly defined sections indicated by x_1 and x_2. Notably, the interval $x_1 - x_2$ aligns with nD_x, an indicator of periodic behavior. In the context of a one-dimensional derivation, the relationship of the electric field is solely dependent on the coordinate x as expressed in Eq. 3.1.

$$E(x_2) = E(x_1 + nD_x) = E(x_1)e^{-jk_x^i nD_x} \tag{3.1}$$

Equation 3.1 demonstrates that the field at position x_2 can be expressed as the field at position x_1 multiplied by a phase factor $e^{-jk_x^i nD_x}$. This phase factor accounts for

the difference in position along the periodic structure. It is important to note that in this one-dimensional derivation, the relationship between fields is not influenced by either the y or z coordinates. This equation highlights the periodic behavior of the fields within the structure. The diffracted field at x_2 is related to the field at x_1 through the phase factor, which depends on the wave vector and the periodicity of the structure.

Equation 3.1 can be manipulated into a generic equation for a diffracted field, as shown in Eq. 3.2:

$$E(x) = E^{(\rho)}(x)e^{-jk_x^i} \tag{3.2}$$

In this equation, $E^{(\rho)}(x)$ represents a function that satisfies the periodicity property, such that $E^{(\rho)}(x) = E^{(\rho)}(x + nD_x)$ for any integer n. Consequently, for any integer multiple of D_x along the x axis, the boundary conditions for the diffraction problem are identical. The only difference is seen in the phase factor when excited by an incident wave. According to Maxwell's equations and the properties of uniqueness, it can be assumed that the fields at these distances are the same, differing only by the aforementioned phase factor. The property of uniqueness refers to the principle that a physical system or a solution to a problem is uniquely determined by its defining characteristics or boundary conditions. In other words, if a certain set of conditions or constraints are specified, there can only exist one solution that satisfies those conditions.

Taking advantage of the uniqueness properties of Maxwell's equations, the expression $E^{(\rho)}(x)$ can be developed into a Fourier series expansion, as expressed in Eq. 3.3:

$$E^{(\rho)}(x) = \sum_{n=-\infty}^{\infty} E_n^{(\rho)} e^{j2\pi n \frac{x}{D_x}} \tag{3.3}$$

In this equation, $E_n^{(\rho)}$ represents the coefficient of the Fourier series, which can be

obtained by evaluating the integral given in Eq. 3.4:

$$E_n^{(\rho)} = \frac{1}{D_x} \int_0^{D_x} E^{(\rho)}(x) e^{j2\pi n \frac{x}{D_x}} dx \tag{3.4}$$

The Fourier series expansion allows the representation of $E^{(\rho)}(x)$ as a sum of complex exponential functions, each with a specific spatial frequency determined by the integer n. The coefficients $E_n^{(\rho)}$ capture the contribution of each spatial frequency component to the overall field.

This Fourier series representation is valuable in the analysis of periodic structures as it provides a systematic way to describe the diffracted field and its harmonic components. By determining the coefficients $E_n^{(\rho)}$, the field can be fully characterize within the periodic structure.

By substituting Eq. 3.3 into Eq. 3.2, the field for the periodic structure can be rewritten as:

$$E(x) = \sum_{n=-\infty}^{\infty} E_n^{(\rho)} e^{-j\left(k_x^i - \frac{2\pi n}{D_x}\right)x} \tag{3.5}$$

Equation 3.5 represents the summation of plane waves with constant propagation along the x axis. Each term in the summation corresponds to a specific spatial frequency component characterized by the coefficient $E_n^{(\rho)}$. These coefficients capture the contribution of each spatial frequency component to the overall diffracted field.

The term k_x in Eq. 3.5 represents the spatial periodicity of the structure propagating along the x axis. It is given by Eq. 3.6:

$$k_x = k_x^i - \frac{2\pi n}{D_x} \tag{3.6}$$

Here, k_x^i represents the transverse wave vector of the incident plane wave, and the term $\frac{2\pi n}{D_x}$ accounts for the possible different modes dependent on n. Depending on whether the wave number is real or imaginary determines if the plane wave is an

oblique propagating wave or an evanescent mode respectively.

The spatial periodicity of a planar periodic structure, characterized by a purely real wave vector, plays a crucial role in determining the direction of propagation for transmitted and reflected waves, as illustrated in Fig. 3.2. The figure depicts the wave vectors that arise when a metasurface is modulated with a spatial periodicity β_ρ, where spatial harmonics (represented here as $-3 \leq m \leq 1$) propagate while others become evanescent with $\Re = k_{x,m} > k_0$.

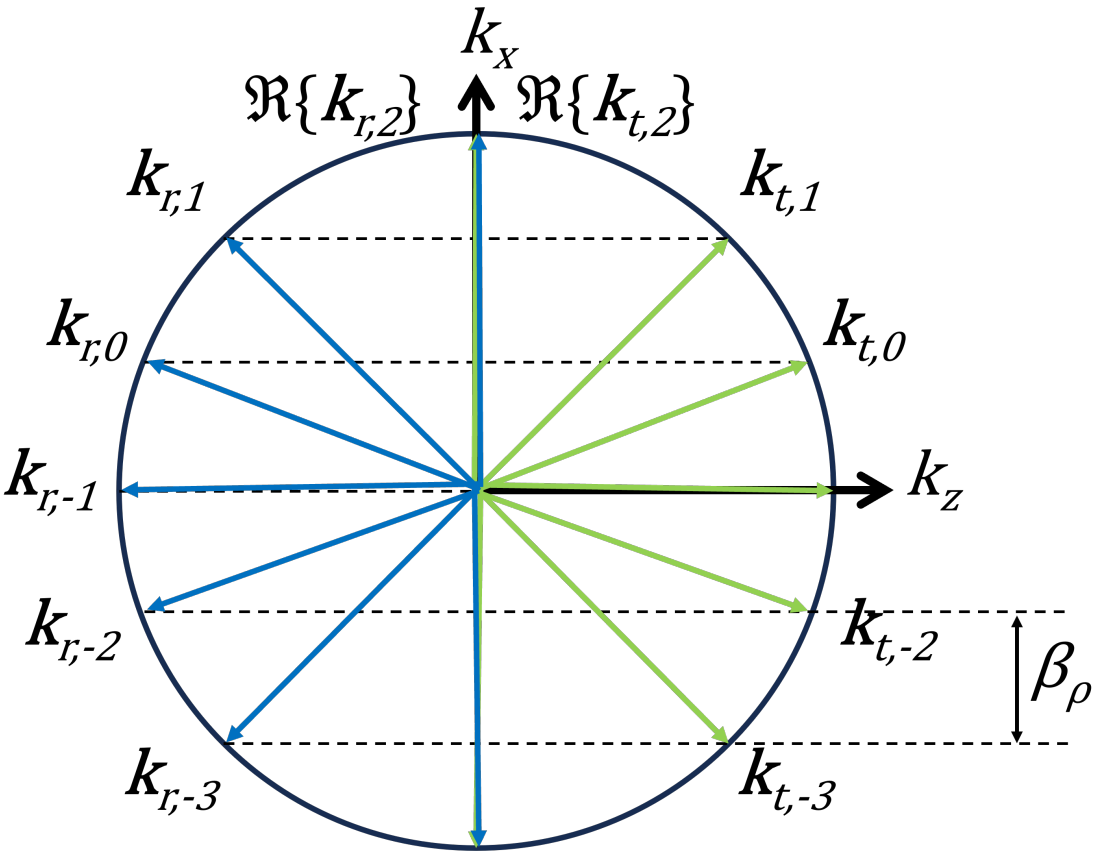

Figure 3.2: Wave vectors describing the spatial harmonics that arise when a metasurface is modulated with a spatial frequency

According to Maxwell's equations, the propagation vectors for Floquet modes must match the wave number in the medium through which they propagate. This principle dictates that the propagation vectors terminate at the curvature of the circle.

However, it is important to note that due to the limitations of Maxwell's equations and the properties of uniqueness, the direction of wave propagation along the x axis is ultimately determined by Equation 3.6.

The foundational principles of Floquet's theorem, originally developed for one-dimensional structures, find extension in both two-dimensional and three-dimensional periodic systems. In particular, the two-dimensional version is highly relevant to metasurfaces, while the three-dimensional adaptation is pertinent to metamaterials.

To illustrate this concept for a metasurface, consider a scenario in which a plane wave with the wave vector (k_x^i, k_y^i, k_z^i) impinging upon an infinite, impenetrable structure characterized by spatial periodicity along the x and y directions. The periodic nature of this structure is determined by the parameters D_x and D_y, respectively. An example of such a periodic structure is visually represented in Fig. 3.3, wherein the unit cell is replicated in both the x and y directions, with additional considerations for variations in rotation, which will be discussed further in this dissertation.

Recall Eq. 3.2 used to describe a one dimensional periodic structure propagating along the x direction which can be expanded to a metasurface or a metamaterial by adding more dimensions. With new spatial dimensions, the electric field, E, is dependent on the variables x, y, and z. With the added dimension of periodicity in the y direction, the spatial periodicity of the field is now described with both D_x and D_y for the x and y directions, respectively. This extension into the y direction is also seen in the description of the phase. The phase dependence of the electric field is given by $e^{-j(k_x^i x + k_y^i y)}$, where k_x^i and k_y^i are the wave vectors of the incident plane wave giving the electric field below.

$$E(x, y, z) = E^{(\rho)}(x, y, z)e^{-j(k_x^i x + k_y^i y)} \tag{3.7}$$

This two-dimensional periodic structure can be studied through a plane wave passing through a two-dimensional structure in free space at an arbitrary angle. The

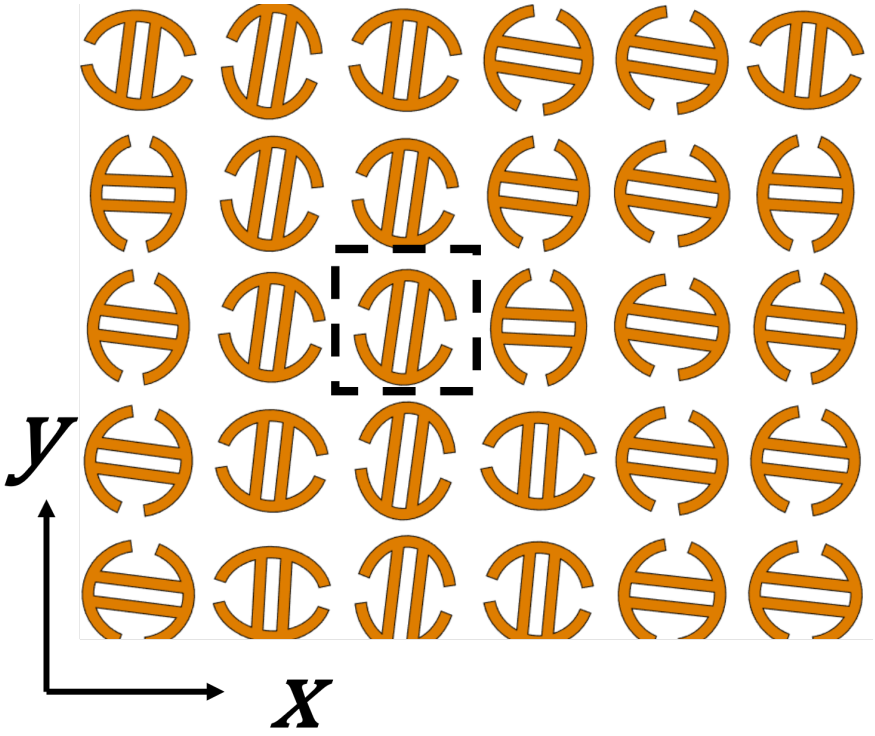

Figure 3.3: Example of a structure periodic along x and y

electric field is analyzed through imposing periodic boundary conditions and port boundary conditions while defining the direction of propagation and polarization of the incident wave.

Similarly to its one-dimensional counterpart, the electric field can be expressed as a summation of different modes described with its equivalent Fourier series expansion shown in Eq. 3.8.

$$E^{(\rho)}(x,y,z) = \sum_{n=-\infty}^{\infty} \sum_{m=-\infty}^{\infty} E_{nm}^{(\rho)} e^{j2\pi\left(n\frac{x}{D_x}+m\frac{y}{D_y}\right)} \tag{3.8}$$

The electric field in this two-dimensional periodic structure can be expressed as a summation of different modes through its equivalent Fourier series expansion, as shown in Eq. 3.8. The coefficients of this Fourier series expansion, denoted as $E_{nm}^{(\rho)}(z)$, are given by the following expression:

$$E_{nm}^{(\rho)}(z) = \frac{1}{D_x D_y} \int_0^{D_x} \int_0^{D_y} E^{(\rho)}(x, y, z) e^{j2\pi\left(n\frac{x}{D_x} + m\frac{y}{D_y}\right)} dxdy \tag{3.9}$$

Upon substituting Eq. 3.8 into Eq. 3.7, the electric field can be represented as:

$$E(x, y, z) = \sum_{n=-\infty}^{\infty} \sum_{m=-\infty}^{\infty} E_{nm}^{(\rho)}(z) e^{-j(k_{xn}x + k_{ym}y)} \tag{3.10}$$

Here, k_{xn} and k_{ym} represent the wave numbers in the x and y directions, respectively, and are defined as:

$$k_{xn} = k_x^i - \frac{2\pi n}{D_x} \tag{3.11}$$

$$k_{ym} = k_y^i - \frac{2\pi m}{D_y} \tag{3.12}$$

The wave number k corresponds to the wave number of the medium in which the structure is situated. Additionally, it is worth emphasizing that the electric field described by Equation 3.10 must adhere to the Helmholtz equation, which is derived from Maxwell's equations. This Helmholtz equation, as denoted by Eq. 3.13, governs the behavior of the electric field, denoted as E, within the periodic structure.

By substituting Equation 3.10 into Equation 3.13, the Helmholtz equation simplifies to:

$$\nabla^2 E + k^2 E = 0 \tag{3.13}$$

The above equation can be expanded as shown in Equation 3.14, where the terms have been separated and rearranged:

$$\sum_{n=-\infty}^{\infty} \sum_{m=-\infty}^{\infty} \left[\frac{\partial^2}{\partial z^2} E_{nm}^{(\rho)}(z) - k_{xn}^2 E_{nm}^{(\rho)}(z) - k_{ym}^2 E_{nm}^{(\rho)}(z) + k^2 E_{nm}^{(\rho)}(z) \right] = 0 \tag{3.14}$$

To simplify further and combine constant terms while introducing a variable to represent the wave numbers, Eq. 3.14 can be rewritten as:

$$\sum_{n=-\infty}^{\infty}\sum_{m=-\infty}^{\infty}\left[\frac{\partial^2}{\partial z^2}E_{nm}^{(\rho)}(z)+k_{znm}^2E_{nm}^{(\rho)}(z)\right]=0 \tag{3.15}$$

In this refined form, the variable k_{znm}^2 is explicitly defined as:

$$k_{znm}^2=k^2-k_{xn}^2-k_{ym}^2 \tag{3.16}$$

Solving the wave equation presented in Equation 3.15 leads to the following solution:

$$E_{nm}^{(\rho)}(z)=E_{nm}^{(\rho_0)}e^{-jk_{znm}z} \tag{3.17}$$

Here, $E_{nm}^{(\rho_0)}$ represents a constant. Substituting Equation 3.17 into Equation 3.10 results in the final expression for the electric field within a two-dimensional periodic structure:

$$E(x,y,z)=\sum_{n=-\infty}^{\infty}\sum_{m=-\infty}^{\infty}E_{nm}^{(\rho_0)}e^{-j(k_{xn}x+k_{ym}y+k_{znm}z)} \tag{3.18}$$

Equation 3.18 represents the electric field within a two-dimensional periodic structure as a superposition of plane waves. Each plane wave is characterized by distinct coefficients denoted as $E_{nm}^{(\rho_0)}$ and associated wave vectors $(k_{xn}, k_{ym}, k_{znm})$. When both n and m equal zero, this corresponds to exciting the fundamental Floquet mode. These wave vectors collectively account for the periodicity along the x, y, and z directions and dictate the spatial variation of the electric field within the periodic structure.

In scenarios where the sum of the squares of the wave vectors in the x and y directions, namely k_{xn}^2 and k_{ym}^2, is less than the square of the wave number k (as

expressed in Equation 3.19), it results in the z component of the wave vector being a real quantity.

$$k_{xn}^2 + k_{ym}^2 \leq k^2 \tag{3.19}$$

This condition ensures that the z component of the wave vector, denoted as k_{znm}, can be expressed as:

$$k_{znm} = \sqrt{k^2 - k_{xn}^2 - k_{ym}^2} \tag{3.20}$$

When Eq. 3.20 yields a real value for k_{znm}, it signifies that the harmonics represent conventional plane waves. These waves are characterized as homogeneous and non-evanescent. In this context, the phase of the wave remains constant across the entire wavefront, and the amplitude is also constant within the plane perpendicular to the direction of propagation.

Conversely, when the sum of the squares of the x and y components of the wave vector exceeds the square of the wave number of the medium, as outlined in Equation 3.21, the z component of the wave vector becomes purely imaginary.

$$k_{xn}^2 + k_{ym}^2 > k^2 \tag{3.21}$$

In such cases, the wave vector k_{znm} is expressed as:

$$k_{znm} = -j\sqrt{k^2 - k_{xn}^2 - k_{ym}^2} \tag{3.22}$$

When the z component of the wave vector becomes purely imaginary, it indicates the propagation of evanescent modes. These waves propagate in a direction orthogonal to a surface while maintaining a constant phase. Their magnitude decreases exponentially perpendicular to the surface. In the absence of losses, these waves

propagate primarily within the xy plane and attenuate as they extend along the z direction.

Understanding these evanescent modes is crucial for the characteristics and functionalities of metasurfaces and other periodic structures, forming the foundation for exploring their properties and applications in electromagnetic phenomena.

3.2 Surface Wave Characteristics and Analysis

Building upon the insights gained in the previous section regarding evanescent waves and their significance in periodic structures, this section delves deeper into the analysis of waves and more specifically the characterization of surface waves. The initial part of this section is dedicated to the analysis and characterization of surface waves, exploring their properties and behaviors in various contexts. The latter half of this section, discusses the application of equivalent circuit theory for studying transverse electric (TE) and transverse magnetic (TM) waves to help construct the dispersion curves for the unit cells that carry the surface waves.

3.2.1 Surface Impedance and Wave Characterization

A surface wave is an electromagnetic wave that is bound to the interface of two materials, typically air and a metallic surface in the context of MTSs. Typically, the surface impedance between the two interfaces control the properties of the electromagnetic wave. In particular, when dealing with metallic surfaces, the surface impedance can be effectively manipulated by introducing textures or patterns. This manipulation allows for precise control over various surface wave properties, including whether the surface behaves inductively or capacitively, as well as controlling the magnitude and phase of the surface wave.

For instance, consider a surface with an impedance denoted as Z_s and an associated electric field with an attenuation constant, α, as illustrated in Fig. 3.4. Controlling the parameters, such as the attenuation controls the rate at which the wave exponentially

decays as it travels across the surface.

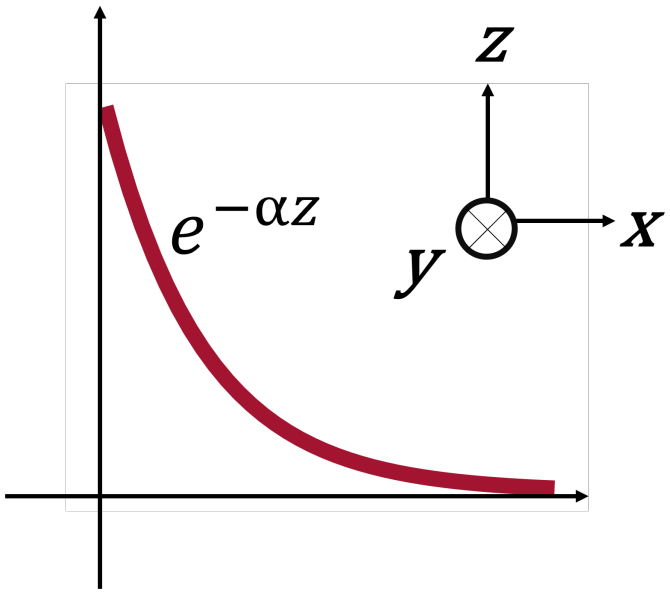

Figure 3.4: Surface impedance, Z_s, controls the electric field through an associated attenuation constant α, showcasing the ability to control the decay rate of surface waves, influencing their behavior and properties.

The classification of a surface wave is based on whether the impedance is positive or negative, which, in turn, influences the type of surface wave that occurs. According to Maxwell's equations applied to the context of surface impedance and its relation to surface waves, TM waves are observed on inductive surfaces. This behavior is mathematically expressed as:

$$Z_{s,TM} = \frac{j\alpha}{\omega\epsilon} \tag{3.23}$$

Conversely, TE waves are found on capacitive surfaces, and this is mathematically described as:

$$Z_{s,TE} = \frac{-j\omega\mu}{\alpha} \tag{3.24}$$

In the above equations, μ and ϵ represent the permeability and permittivity, re-

spectively, of the materials involved, while ω denotes the angular frequency of the electromagnetic wave. It is important to note that both equations describe purely reactive components and adhere to Foster's reactance theorem, which is a fundamental principle in electromagnetic theory discussed more extensively in a later chapter.

TE waves, excited with an inductive reactive surface, are a category of electromagnetic waves characterized by having an electric field perpendicular to the direction of wave propagation. For instance, in the case of a wave propagating along the x direction, the electric field will oscillate in the y direction. TM waves, on the other hand, share the same fundamental concept but exhibit a magnetic field that is perpendicular to the direction of wave propagation. Again, using the example of a wave traveling along the x direction, the magnetic field will be oriented in the transverse direction, typically in the y or z direction [26].

In the realm of metasurfaces, the effective impedance of the surface hinges on the design of its metallic patches and the spacing that separates them. When these patches feature narrow gaps, the effective impedance takes on a capacitive nature. Conversely, when there's oscillating current between neighboring patches due to metallic patches with apertures, the impedance becomes inductive. In many practical cases, the surface exhibits a combination of both capacitive and inductive elements, and this complex behavior can be modeled using a parallel LC resonant circuit expressed by the following equation:

$$Z_s = \frac{j\omega L}{1 - \omega^2 LC} \tag{3.25}$$

Figure 3.5(a) illustrates the capacitance due to the presence of a gap and inductance arising from the circulation of current. These reactances can be effectively modeled as a parallel resonant circuit, as demonstrated in Fig. 3.5(b). It is important to emphasize that the values relevant to this model are not the capacitance and inductance of individual components but rather the sheet capacitance and sheet inductance, which

are employed to characterize the surface impedance. These properties depend on both the inherent attributes of each element and their specific spatial arrangement for to resonance of the surface.

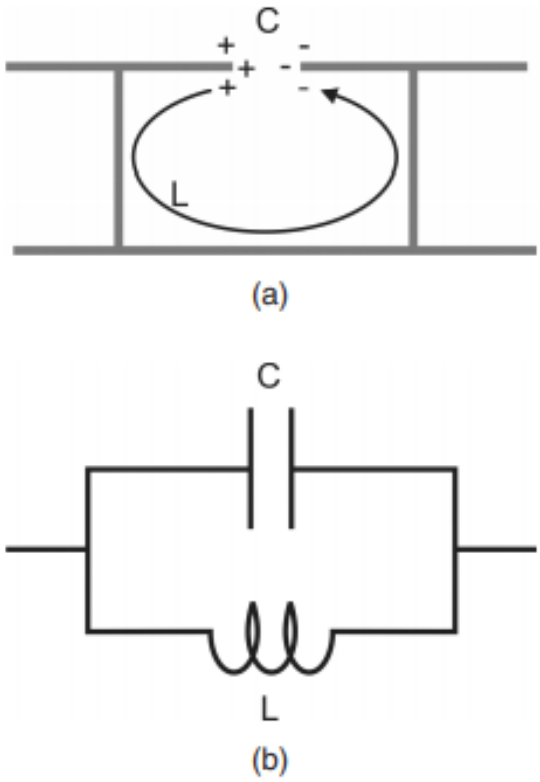

Figure 3.5: (a) Illustration of the capacitance acquired through the presence of a gap and the inductance arising from the circulation of current within the structure. (b) Representation of the structure's behavior as a parallel resonant circuit, emphasizing the importance of sheet capacitance and sheet inductance in characterizing the surface impedance.

The resonant frequency, denoted as ω_0, is determined by $1/\sqrt{LC}$. As per Eq. 3.25, below the resonant frequency, the surface exhibits inductive behavior, which supports TM waves. Conversely, above the resonant frequency, it displays capacitive characteristics, supporting TE waves. As the frequency approaches the resonant value, the impedance tends to become purely real, indicating a lack of support for surface waves.

To describe the impedance characteristics of these surfaces, an effective surface impedance model is often employed. This approach, utilizing an equivalent lumped

element circuit, remains valid when the unit cells of the metasurface are significantly smaller than the wavelength. The behavior of these unit cells can be described through their dispersion characteristics, as shown in the equation below.

$$k^2 = \mu_0 \epsilon_0 \omega^2 + \alpha^2 \tag{3.26}$$

In Eq. 3.26, the symbol k corresponds to the wave number, μ_0 denotes the permeability of free space, ϵ_0 represents the permittivity of free space, ω stands for the angular frequency, and α is the attenuation constant, also known as the decay constant.

By combining Eq. 3.23 and Eq. 3.26, the wave number for a TM wave can be expressed as a function of the angular frequency and the free space impedance, denoted as η, which equals the $\sqrt{\mu_0 \epsilon_0}$, with c, defined as $\sqrt{\mu_0 / \epsilon_0}$, representing the speed of light in a vacuum:

$$k_{TM} = \frac{\omega}{c} \sqrt{1 - \frac{Z_s^2}{\eta^2}} \tag{3.27}$$

A similar approach can be applied to TE waves by combining Eq. 3.24 and Eq. 3.26:

$$k_{TE} = \frac{\omega}{c} \sqrt{1 - \frac{\eta^2}{Z_s^2}} \tag{3.28}$$

Substituting Eq. 3.25 into both Eq. 3.27 and Eq. 3.28 yields the dispersion diagram used to find the impedance values of the unit cells. An example of a dispersion diagram is presented in Fig. 3.6, with the resonant frequency denoted as f_0. Below the resonance frequency, the diagram shows support for TM modes, while TE waves are supported for frequencies above the resonance point. It is worth noting that at the lower end of the dispersion curve, the waves closely align with the light line and exhibit weaker binding to the surface. However, as the frequency increases, the curves

deviate from the light line, indicating a stronger binding of waves to the surface.

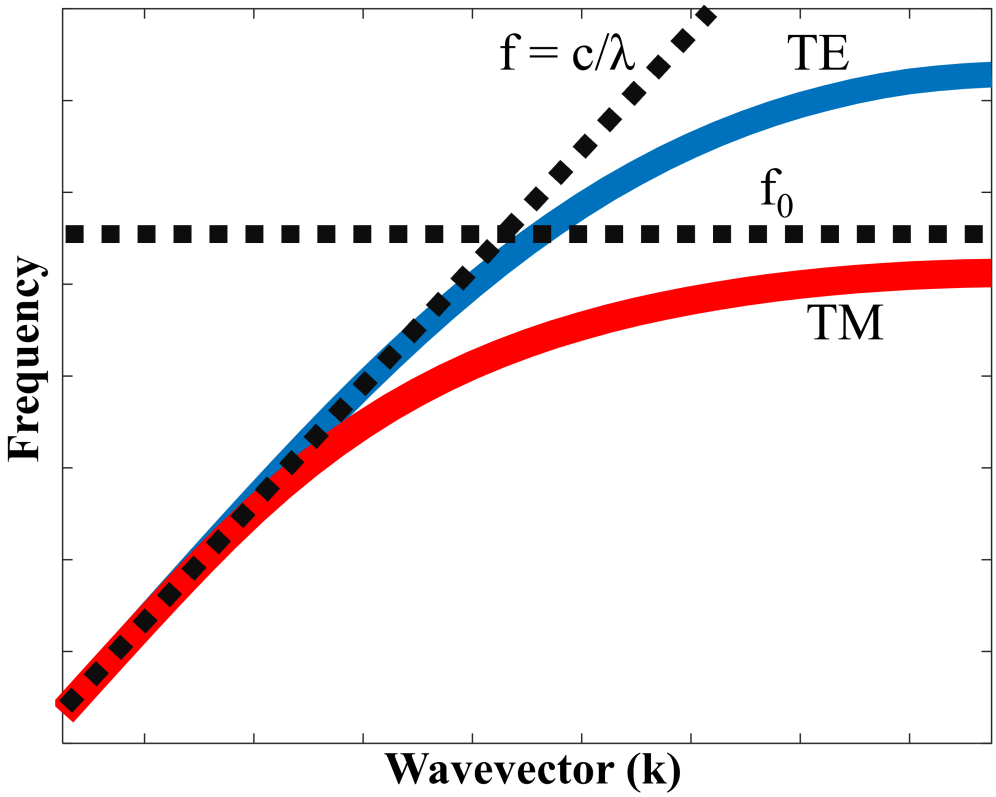

Figure 3.6: Example of a surface wave dispersion diagram for a surface wave displaying the light line, f, the design frequency, f_0, and a TE and TM wave

The model discussed above provides a means to predict electromagnetic properties, including beam shape, polarization, and reflection phase, based on the surface impedance of the metasurface. It offers insights into surface wave behavior and facilitates the design and optimization of metasurface-based devices.

3.3 Incorporation of Modulated Metasurfaces for Achieving Wave Manipulation

This section delves into the concept of impedance boundary conditions, which govern the interaction of surface waves with material interfaces. Impedance boundary conditions, categorized as isotropic and anisotropic, establish the relationship between electric and magnetic fields at these boundaries. The section explores their theoretical foundations, mathematical expressions, and highlights the key differences between

these two categories.

3.3.1 Impedance Boundary Conditions

Metamaterials and metasurfaces make clever use of wave scattering within a medium to achieve specific characteristics. However, modeling this phenomenon can be quite challenging. The complexity arises because the electromagnetic field extends both inside and outside the scattering material. This necessitates the use of volume integrals to solve for the field behavior. Nevertheless, a simplification becomes possible when an electromagnetic wave interacts with a surface. This simplification is achieved through the incorporation of impedance boundary conditions.

These boundary conditions establish a relationship between the tangential components of the electric and magnetic fields. They depend on surface properties like capacitance and inductance, as well as the characteristics of the incident field. When analyzing the interface between two non-perfectly conducting, isotropic, and homogeneous media in the context of electromagnetic wave interactions, specific boundary conditions can be applied.

These boundary conditions are characterized by two properties. The first property states that the cross product between the normal vector to the electric field and the normal vector to the magnetic field must equal zero at the surface. The second property states that the dot product between the normal vector to the electric field density and the normal vector dotted with the magnetic field density must also be zero at the surface. Importantly, these properties are interdependent and together establish an impedance boundary condition. This condition serves to relate the characteristics of the first medium to those of the second.

However, when the second medium is a perfect electric conductor (PEC), the analysis narrows down to the fields in free space or dielectric. In this context, the initial conditions for these boundary conditions become as follows:

$$\hat{n} \times \mathbf{E} = 0 \tag{3.29}$$

$$\hat{n} \cdot \mathbf{B} = 0 \tag{3.30}$$

$$\hat{n} \cdot \mathbf{D} = \delta \tag{3.31}$$

$$\hat{n} \times \mathbf{H} = \mathbf{K} \tag{3.32}$$

where δ is the charge distribution and K is the current distribution. Particularly, when the refractive index of the PEC significantly exceeds that of free space, it simplifies the situation, with only Eq. 3.29 and Eq. 3.30 manifesting in free space.

To comprehend the radiative properties of metasurfaces, a common approach involves investigating scattering from an infinite two-dimensional dielectric slab, as illustrated in Fig. 3.7. On the left side of the illustration, an electric field parallel to the direction of propagation excites a TM wave. Conversely, on the right side, the electric field is perpendicular to the propagation dire ion, characterizing it as a TE wave. These incident waves interact with a grounded dielectric, which can be effectively modeled and analyzed using an equivalent local transmission line model. In this model, a grounded dielectric slab is considered, with the colored arrows (both purple and red) representing the transmitted waves for both TM and TE polarizations, and the grey arrow indicating the reflected wave. Additionally, the yellow components in the local transmission line model represent the dielectric in the slab, while the grey components represent the air above it.

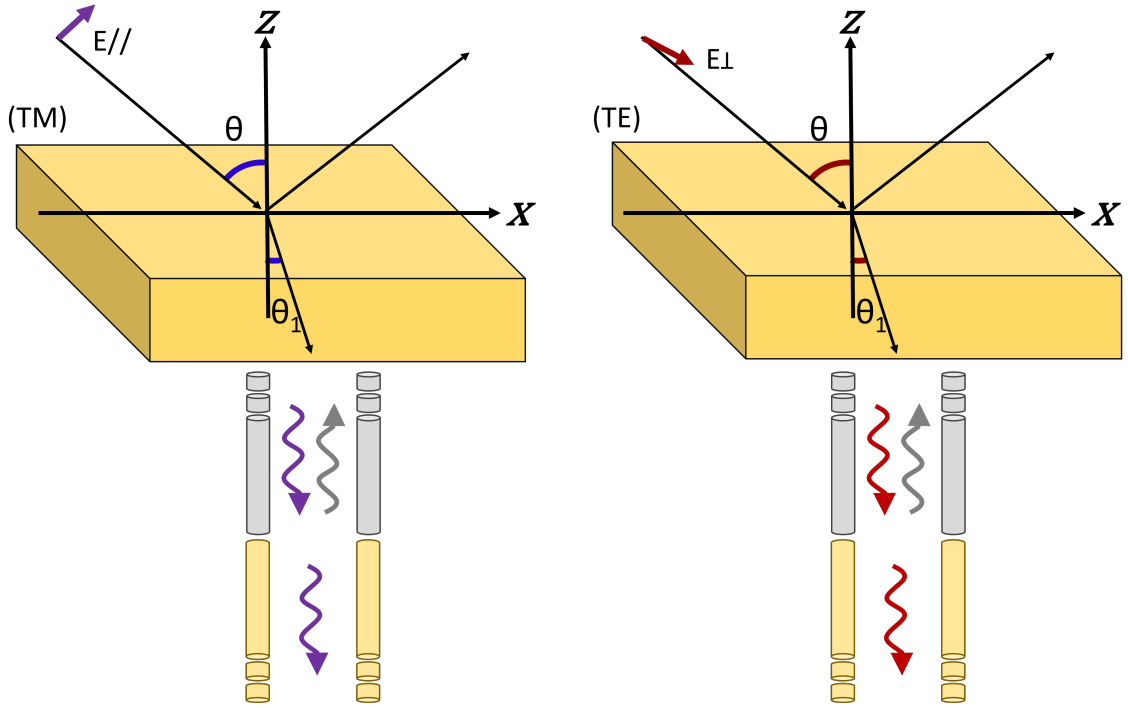

Figure 3.7: An incident wave impinging on a grounded dielectric slab, illustrating TM (left) and TE (right) wave configurations. These scenarios can be equivalently modeled as a local transmission line setup for the study of scattering characteristics on a MTS as shown below the slab where the colored arrows show the transmission and the grey arrows show reflection.

3.3.2 Sinusoidal Modulation of Impedance

By introducing a textured metallic surface to the grounded dielectric slab, a reactive element is incorporated into the model as an IBC which can either consist of isotropic or anisotropic reactance.

3.3.2.1 Isotropic Modulated Metasurfaces

Under the assumption of a sinusoidally modulated surface with a uniform IBC characterized by a constant inductive reactance, this surface is considered isotropic. In this case, the impedance factor denoted as X_s takes on the form of a positive scalar value, determining the inductive reactance of the surface. The primary wave excited on this surface is the TM wave, as discussed in Section 3.2.1. Consequently, this implies that the relationship between the tangential components of the electric field

and the tangential components of the magnetic field can be expressed as follows:

$$jX_s z \times (H \times z)|_{z=0} = E \times z|_{z=0} \tag{3.33}$$

This equation establishes connection between the tangential electric and magnetic fields at the surface, derived directly from Maxwell's equations. The tangential components of the electric and magnetic surface waves are given by:

$$E_{sw}^{tan} = I_{TM} j X_s H_1^{(2)}(\beta_{sw}\rho)\hat{\rho} \tag{3.34}$$

$$H_{sw}^{tan} = -I_{TM} X_s H_1^{(2)}(\beta_{sw}\rho)\hat{\Phi} \tag{3.35}$$

In the above equations, key variables are defined as follows: I_{TM} stands for the current, X_s represents the surface impedance, $H_1^{(2)}$ is the first-order Hankel function of the second kind, and $\hat{\rho}$ and $\hat{\Phi}$ denote the unit vectors in the radial and azimuthal directions, respectively, within a cylindrical coordinate system. In addition, the phase constant characterizing the surface wave, is denoted as β_{sw}, determined by achieving resonance for a free space propagating TM wave. The phase constant of the surface is described by its relationship of X_s, ζ,and k.

$$\beta_{sw} = k\sqrt{1 + \left(\frac{X_s}{\zeta}\right)^2} \tag{3.36}$$

In the equation of the phase constant, k signifies the wave number, while ζ corresponds to the characteristic impedance of the medium. The phase constant can be tailored by adjusting the surface impedance in order to aid in the design of a MTS in order to match to specifications such as realizability.

The surface impedance gradient is commonly implemented through metallic cladding on top of the dielectric slab transforming the grounded dielectric slab and equivalent

transmission line model in Fig. 3.7 to Fig. 3.8. This additional element introduces a novel reactive component into the transmission line model that accounts for the sheet reactance on the dielectric. Considering the reactance is uniform as stated earlier, the metallic cladding similarly has to be symmetric with the direction of propagation for the supported mode. In this regard, the direction of propagation does not alter the results of the metasurface because the shape and impedance appears identical to the wave.

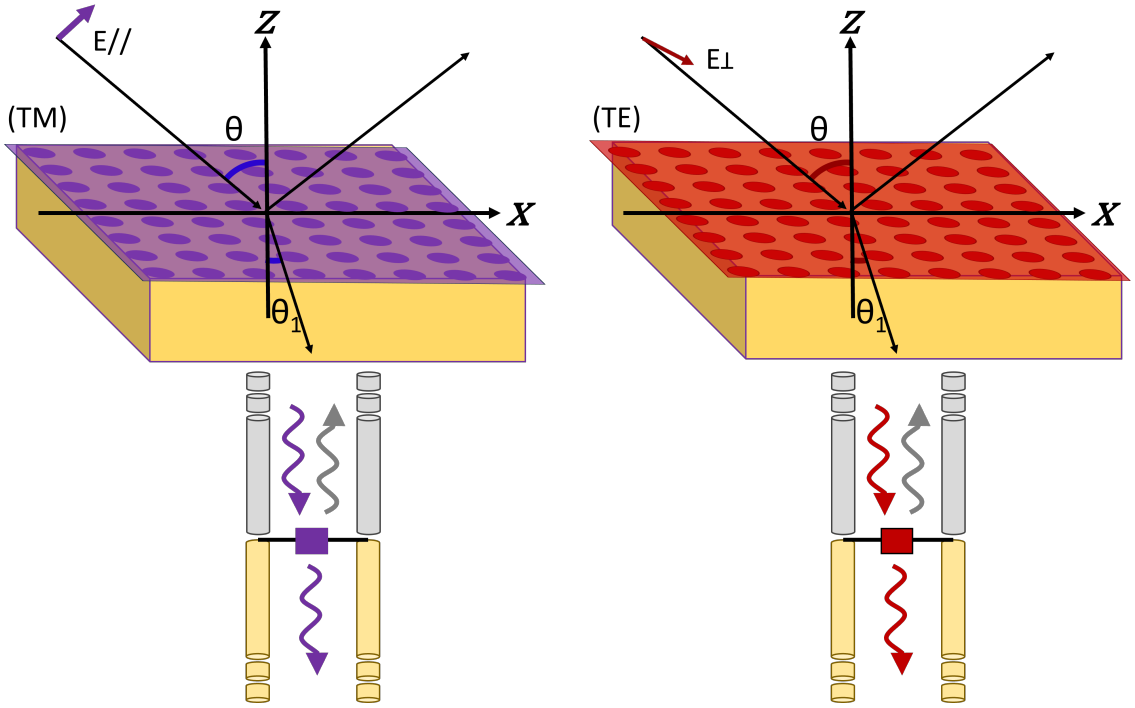

Figure 3.8: An incident wave impinging on a grounded dielectric slab with metallic cladding, illustrating TM (left) and TE (right) wave configurations. The structure can be locally modelled as a transmission line with a shunt impedance representing X_s.

Two examples of this type of symmetry producing an isotropic impedance is illustrated in Fig. 3.9. In the first example, the antenna is designed with square metallic elements of varying sizes embedded on a dielectric slab. For this type of element, the shape is symmetric for the orthogonal polarizations resulting in the same radiation

pattern for both polarizations. Similarly, the metallic elements on the right side of the figure, also embedded on a dielectric slab, have a radial symmetry. In both of these antenna designs, circular polarization is the designed polarization. It is worth noting that the individual elements that compose this antenna are significantly smaller than the wavelength of the operating frequency, allowing the surface wave to travel across the antenna. The isotropic nature of the modulated surface impedance enables it to interact with the incident waves in a consistent manner, irrespective of the direction of propagation.

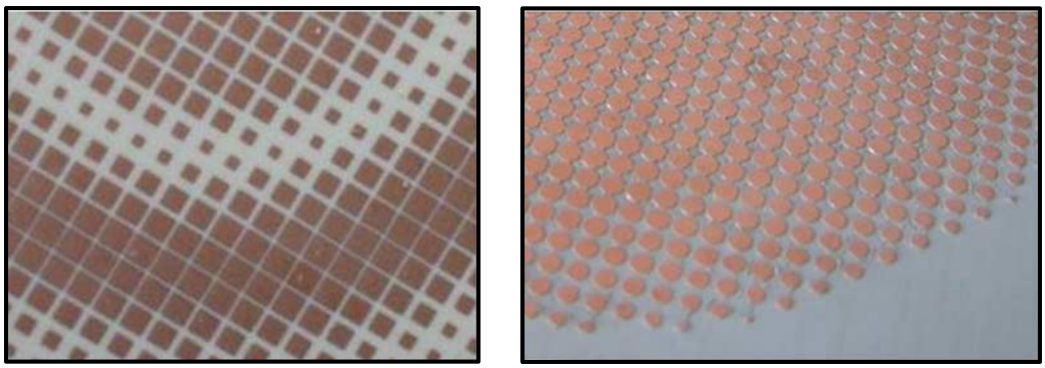

Figure 3.9: Two antenna designs of metallic patches embedded on a grounded dielectric slab demonstrating symmetry for isotropic impedance for a circularly polarized wave with square(left) and circle (right) unit cells used to discretize the surface impedance [1]

The modulated surface impedance is defined through a sinusoidal pattern and implemented with the elements, such as those exemplified in Fig. 3.9. These elements, called unit cells, are used to discretize the impedance of the surface in order to realize the sinusoidal modulation. Through various geometric varieties of the unit cell, the range of impedance values can be created in order to match to the discetized surface. Each unit cell is mapped to the surface impedance to have a specific geometry at each point on the antenna creating a smooth and continuous modulation of the surface impedance. Due to the symmetry of the unit cell, lending to the impedance being isotropic, the impedance, X_s, is considered a scalar. The scalar factor $jX_s(\rho)$

relates the transverse components of the electric and magnetic fields.

In the context of TE and TM waves, the amplitude of the transverse wave vector is defined as $k_t = k_t(\rho)\hat{k}_t(\rho)$, where $k_t(\rho)$ represents the radial dependence, and $\hat{k}_t(\rho)$ is the corresponding unit vector. This wave vector plays a crucial role in describing the dispersion equation, denoted as Eq. 3.37, which is derived using the transverse resonance method.

$$k_{tn}(\rho) = k\sqrt{1 + \left(\frac{X_s(\rho)}{\zeta}\right)^2} \tag{3.37}$$

The transverse resonance method is a valuable technique employed to ascertain the propagation constant of waves. This method capitalizes on the presence of standing waves occurring in a specific direction, which is transverse to the primary propagation direction. These standing waves emerge as a consequence of purely reactive loads positioned at both ends of the transmission line, symbolizing the path of wave propagation. Under these circumstances, the transmission line terminated with reactive loads is considered a resonant structure. This resonance condition dictates that the input impedance when looking forward, must be equal in magnitude but opposite in sign to the input impedance, when looking backward. In other words, the sum of these two impedance values must equal zero to satisfy the conditions for resonance.

Recalling back to Eq. 3.37, the term $k_{tn}(\rho)$ characterizes the modified transverse wave vector associated with the modulated impedance. This equation reveals that when k_{tn} exceeds the wave number in free space, the fields undergo exponential attenuation perpendicular to the metasurface. This phenomenon is illustrated in Fig. 3.10, where the spiral pattern indicates the presence of impedance modulation.

The exponential attenuation observed in fields perpendicular to the metasurface is a consequence of the interaction between the incident wave and the modulated impedance profile. This modulation of impedance effectively alters the local refractive index and phase velocity, consequently influencing the propagation path of the

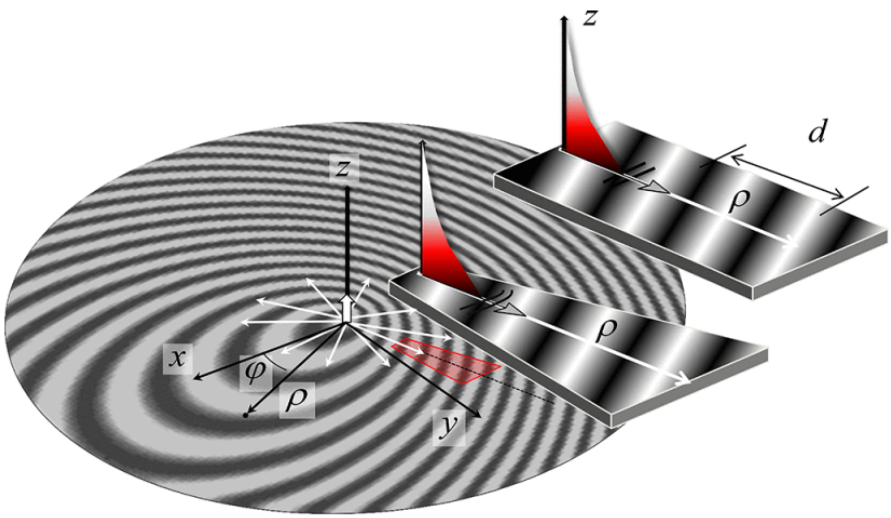

Figure 3.10: Field attenuating exponentially normal to a metasurface with a spiral pattered impedance [1]

supported surface wave.

The modulation of the wave vector, achieved through the introduction of a modulated surface impedance, brings about changes in the phase velocity and propagation trajectory of the surface wave supported by the metasurface. This modulation is realized by imposing boundary conditions that locally adjust the value of k_t, ensuring that the wave follows the evolving impedance profile. The path of the propagating wave is dictated by the local refractive index, adhering to Fermat's principle, which dictates that the wave follows the minimum optical path. Through precise control of surface impedance modulation, the metasurface gains the capability to manipulate the direction and behavior of the surface wave, allowing for the achievement of specific desired functionalities.

3.3.2.2 Anisotropic Modulated Metasurfaces

When transitioning from isotropic to anisotropic impedance, a fundamental shift occurs in the complexity of boundary conditions. Unlike isotropic impedance, which exhibits uniform characteristics in all directions, anisotropic impedance introduces an interplay of field behaviors. An anisotropic impedance boundary condition is created

when the tangential fields on the surface satisfy the relationship: $E_{sw}|z = 0^+ = Z \cdot (z \times Hsw)|_{z=0^+}$. In this case, the impedance is described by a tensor that captures the relationship between the tangential electric and magnetic fields on the surface. This coupling of TE and TM modes, facilitated by the impedance tensor, results in a more intricate wave propagation environment. It allows for tailoring the response of the electromagnetic wave to possibly improve the behavior of the antenna or present other design benefits.

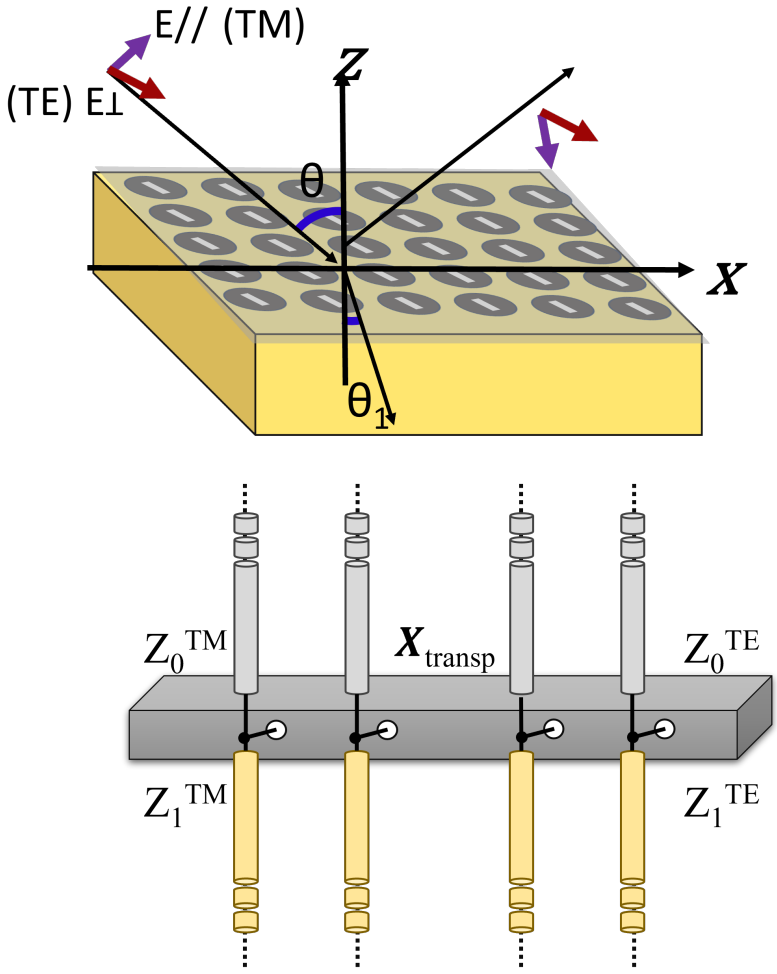

Figure 3.11: Anisotropic surface impedance on an infinite dielectric slab showing the TE and TM coupling effect. The equivalent transmission line model accounts for both modes which adjusts the local model such that both modes are included in the analysis.

Figure 3.11 visually illustrates the anisotropic nature of such impedance conditions, emphasizing the interaction of both the TE and TM modes and the two corresponding transmission line models used to describe them which takes into account both the inductance and capacitance of the surface exciting both a TE and TM wave.

Anisotropy is achieved through the use of metallic cladding, which introduces asymmetry, allowing different angles of propagation to interact with the surface in unique ways. This asymmetry necessitates the use of an impedance tensor, as mentioned in the preceding paragraph.

To design an anisotropic surface, it is crucial to create shapes that lack symmetry in relation to surface wave propagation. Figure 3.12 illustrates this concept with four different unit cell examples, each designed to fulfill anisotropic boundary conditions. Notably, these unit cells exhibit differences in symmetry compared to the examples provided in the section on isotropy. These four unit cells lack both orthogonal and radial symmetry, which means that different directions of propagation will encounter the unit cell's properties differently.

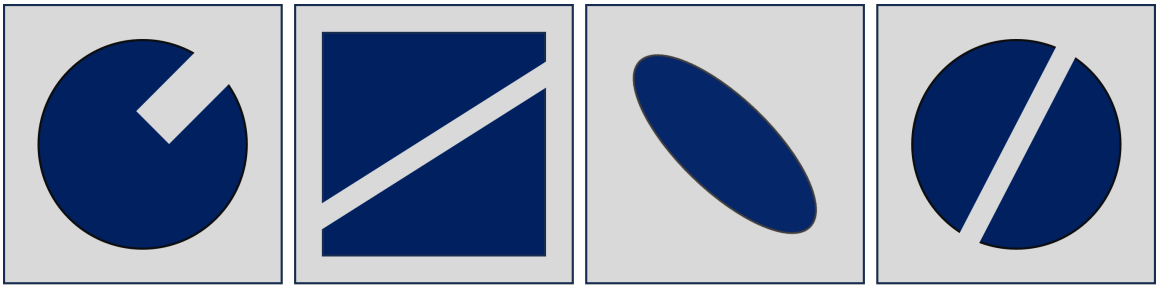

Figure 3.12: Four unit cell examples demonstrating designs for achieving anisotropic boundary conditions. These unit cells lack symmetry, allowing different directions of propagation to interact with them in distinct ways. The asymmetry also introduces the capability to rotate the unit cell, providing an additional parameter for expanding the impedance profile.

The introduced asymmetry also brings forth an intriguing capability: the ability to rotate the unit cell. This additional variable offers a way to expand the range

of achievable impedance variations with the unit cell. It enhances the design flexibility and tunability of anisotropic metasurfaces, allowing for even more versatile applications.

CHAPTER 4: DUAL POLARIZATION METASCREEN

In today's rapidly advancing electromagnetic technology, there is a growing demand for devices that can support multiple functions while simultaneously reducing in size and weight. These advancements are crucial for various applications, including point-to-multi-point communication, wireless tracking, and radar systems. To achieve desired functionalities such as phase delays, polarization control, and wave redirection[27, 28], reflect arrays have traditionally been employed[29, 30]. However, due to their bulky nature, there is a need for smaller alternatives that offer comparable or even improved performance.

An increasingly popular solution for downsizing of electromagnetic devices is the use of MTSs. There are many different types of metasurfaces including lenses, antennas, and imaging structures. They can be designed with a multitude of different methods and different elements types such as diodes or metallic patches [31, 32, 33, 34]. This chapter discusses the utilization of a MTS in the usage of a metascreen: a MTS placed in-between an transmitting source and receiving source to perform a space wave transformation. The most basic design of a metascreen is one layer of metallic patches [35], but this limits design flexibility and, in turn, can introduce an abundance of loss through scattering. To help reduce the excessive scattering, more layers can be used for extra degrees of freedom in the design. This has been done in [36, 37, 38] to achieve beam steering. These designs, although less lossy, are restricted in their use to steering an incident wave in one polarization direction.

In order to overcome this limitation, a space wave transforming metascreen is proposed that overcomes this limitation by creating a dual polarization steering structure. In the interest of conserving space, this structure is able to perform the task of two

metasurfaces in the space, weight, and resources of one metascreen. This dual polarization effect relies on the surface impedances to be independent for the vertical and horizontal modes. The independent beam steering is accomplished through a three-layer design of metallic patches separated by dielectric slabs.

The structure of this chapter is as follows; the first section delves into the equivalent local transmission line model and provides essential background theory. The subsequent section conducts an in-depth analysis of the unit cell and its varying admittance in the context of the complete MTS design. Following that, the chapter presents and discusses the numerical results obtained from the fully designed structure. Finally, the last section offers concluding remarks on the outcomes and findings.

4.1 Analysis of Metascreen with Anisotropic Admittance Profiles and Independent Polarization Behavior

A metascreen can be described using the generalized Snell's Law, as outlined in [39] and shown in Fig. 4.1, where a phase gradient is introduced at the interface of two mediums to influence the reflection and refraction of the wave. The phase gradient introduced adapts the typical Snell's Law equation, described by $\sqrt{\epsilon_{r1}}\sin\theta_1 = \sqrt{\epsilon_2}\sin\theta_2$ to include the phase with an addition to the equation making it $\sqrt{\epsilon_{r1}}\sin\theta_1 + \frac{1}{k}\frac{\delta\phi}{\delta x} = \sqrt{\epsilon_2}\sin\theta_2$. The linear phase gradient is implemented by discretizing the phase through unit cells, resulting in a phase discontinuity at the interface. In the proposed structure, the metascreen consists of three slotted metallic layers separated by a dielectric layer with a thickness d, to create the periodic structure.

The layers of the metascreen are arranged such that each side of a middle layer contains identical admittance profiles, while the middle layer itself has a separate admittance profile. The identical external layers add an extra degree of freedom into the design canceling out introduced reflection commonly seen in screens with two layers. Fig. 4.2 shows a cross-sectional view illustrating the two identical outer layers defined

with one impedance profile, $\underline{\underline{Y}}_1(x)$, and the middle layer with an impedance profile of $\underline{\underline{Y}}_2(x)$. The layered metascreen is excited with two orthogonal polarizations; the black diagram representing an x polarized wave and the green diagram representing a y polarized wave.

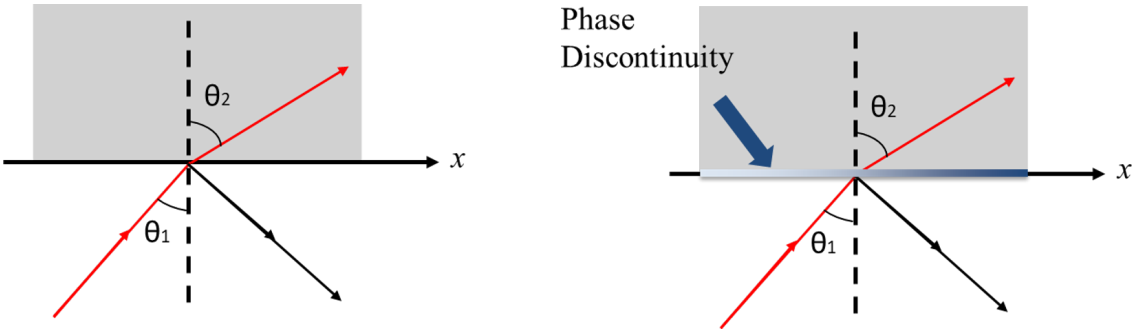

Figure 4.1: Comparison of Snell's Law versus generalized Snell's Law where a phase gradient is introduced at the interface of a medium.

To further analyze the metascreen, a local transmission line model can be employed, as shown in the right half of Fig. 4.2. The transmission line consists of two distinct transmission line models connected together. The left half of the local transmission line model describes the behavior for an x-polarized incident wave, while the right half is utilized for a y-polarized incident wave. By exciting the metascreen with either of the two orthogonal polarizations, the transmitted wave can be steered, and the steering angle is dependent on the admittance profiles. Since the layers possess anisotropic admittance profiles, the steering angles vary based on the polarization, resulting in independent angles for different excitations.

The anisotropy of the admittance is expressed in Eq. 4.1 and Eq. 4.2 for the outer and middle admittance layers respectively. Upon examining the equations, it becomes evident that the 2×2 matrix exhibits position dependence for the two different polarization directions.

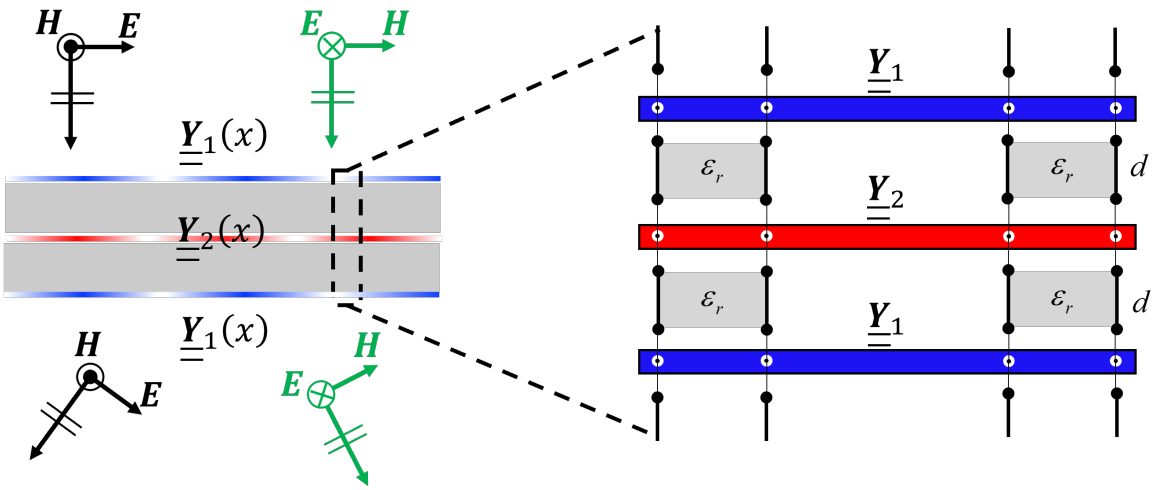

Figure 4.2: Left: Cross-sectional view of the metascreen with $\underline{\underline{Y_1}}(x)$ and $\underline{\underline{Y_2}}(x)$ representing the admittance layers with the blue layers representing one admittance tensor and the red layer representing a separate admittance tensor. This also shows the two polarizations depicted in black and green. This is locally modeled for analysis using a local transmission line model to the right showing the three metascreen layers separated by layers of dielectric.

$$Y_1 \rightarrow \underline{\underline{\boldsymbol{Y}}}_{\mathbf{1}} = \begin{bmatrix} Y_1^{xx} & Y_1^{xy} \\ Y_1^{yx} & Y_1^{yy} \end{bmatrix} \tag{4.1}$$

$$Y_2 \rightarrow \underline{\underline{\boldsymbol{Y}}}_{\mathbf{2}} = \begin{bmatrix} Y_2^{xx} & Y_2^{xy} \\ Y_2^{yx} & Y_2^{yy} \end{bmatrix} \tag{4.2}$$

With the simplified model, the scattering parameters describing the structure can easily be determined using common transmission line equations. It can be noted that there are no closed-form solutions for the transmission line model using these admittance profiles that ensure full transmission due to coupling between the two modes notated by Y_{xy} and Y_{yx}. To achieve a wave that has minimal reflection with the maximum amount of transmission for each polarization, the modes need to be excited independently to prevent the occurrence of coupling between them. To achieve this, the off-diagonal values of both admittance tensors are set to equal zero. Consequently,

Y_{xy} and Y_{yx} are set to equal zero, two independent local transmission line models are used, shown as the inset in Fig. 4.4, with each one separately describing one polarization. Subsequently, the simplified local models can be solved using the $ABCD$ method [39] to find each admittance profile. The full admittance profile is constructed by superimposing the individual admittances into the admittance tensor in their respective positions to fully capture the behavior.

4.2 Unit Cell Design and Validation for Independent Polarization Behavior

The impedance tensor provides an ideal mapping of the metascreen to achieve the desired independent polarization effect. This is implemented through discretizing the impedance using sub-wavelength unit cells. Using the local periodicity assumption, different geometries of the unit cell are studied to find the appropriate shape to fulfill the impedance. Local periodicity allows the unit cell to be analyzed assuming the adjacent unit cells in the screen will exhibit minimal geometric differences. Local periodicity also dictates that the size of the unit cell has to be much much less than the wavelength. The period of the unit cell, p, chosen for this design is $\lambda_o/5$ where λ_o is the free-space wavelength.

The choice of the proposed unit cell was guided by several key advantages it offers to the overall design. Firstly, simplicity of the unit cell's geometry while still being able to encompass the full impedance variation needed for all layers and polarizations is advantageous. The simplicity would streamline the design process, requiring only a single database that can be applied consistently across all layers of the metascreen. Additionally, symmetry plays a critical role in achieving the desired independent polarization effect. To achieve this, the unit cell's layers must exhibit symmetry across both the x and y axes. This symmetry ensures that the metascreen can effectively manipulate and control two orthogonal polarizations independently.

The selected unit cell geometry that aligns with the design requirements of simplicity and symmetry is the slotted modified Jerusalem cross, as illustrated in Fig. 4.3.

The Jerusalem cross offers a host of advantages, making it a suitable choice for the metascreen design. These advantages include its inherent symmetry, structural integrity, rigidity, and compactness. Moreover, the Jerusalem cross exhibits the necessary geometrical variation to cover the impedance range required for the specific structural design of this metascreen. This variation is achieved by adjusting the lengths of its arms. When an x-polarized wave is incident, the length of the arm, L_x, which runs parallel to the y direction, is modified to control the impedance encountered by the x-polarized wave. Similarly, the arm length L_y, which is parallel to the x direction, is adjusted to manage the incident y-polarized wave. The variation in arm lengths in both directions is achieved by altering the length, which ranges from 1 mm to 10 mm. It's worth noting that each slotted arm maintains a consistent width, denoted as w, measuring 0.5 mm. Additionally, the height, h, of each of the longer cross slots situated in the center of the unit cell is 12 mm for both arms.

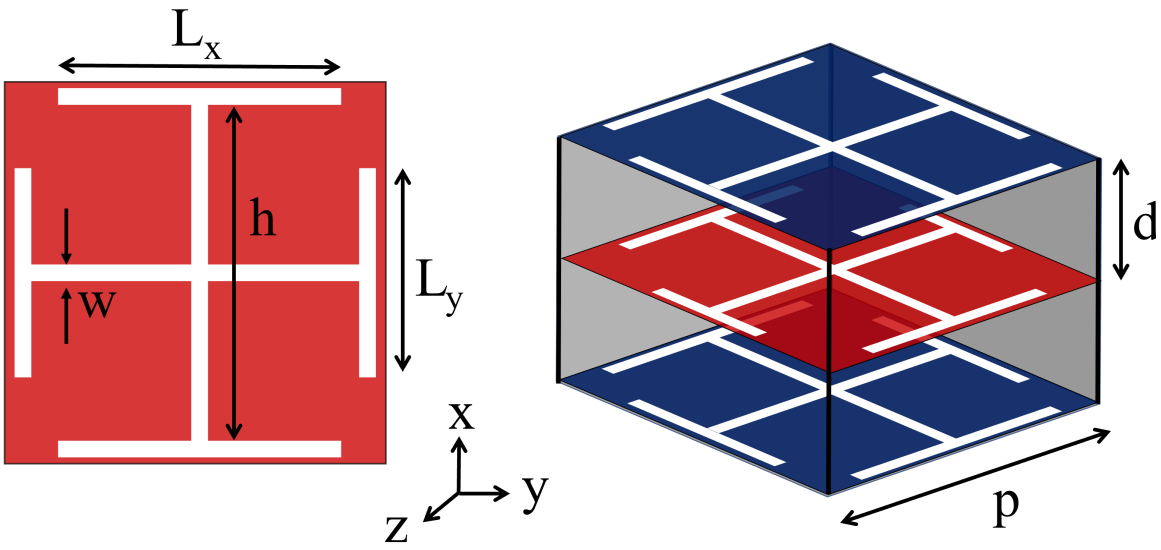

Figure 4.3: Left: Example of a layer of the slotted metallic unit cell annotated with its geometric parameters. Right: Three-dimensional view of the layered unit cell separated by layers of dielectric wit height, d, and a period, p.

The metallic slots within the unit cell are arranged in layers and separated by a dielectric material, as illustrated in the right half of Fig. 4.3. The choice of the separa-

tion distance, denoted as d, is selected to strike a balance between allowing sufficient transmission of waves and preventing unwanted reflections while avoiding coupling between the layers that could alter the admittance characteristics. To maintain the independence of the admittance of each layer, the unit cell is rigorously analyzed at its individual interfaces. Specifically, it is assessed for the interface between air and dielectric for the outer layers and the interface between dielectric layers for the central section. The chosen separation distance that has demonstrated optimal results, preventing excessive scattering and providing the best performance, is $\lambda_o/8$.

The combination of the layered metallic slots and the dielectric material between them forms the complete unit cell for the metascreen. The outer layers, depicted in blue, contribute to the impedance characteristics for $\underline{\underline{Y_1}}(x)$, while the central red layer contributes to the impedance characteristics for $\underline{\underline{Y_2}}(x)$. This careful arrangement ensures that the metascreen can effectively manipulate and control the two orthogonal polarizations independently.

4.2.1 Validation of Unit Cell Performance through Floquet Analysis and Admittance Study

The unit cell is thoroughly examined through Floquet analysis, employing periodic boundaries to acquire the scattering parameters. Subsequently, the admittance values are extracted from these scattering parameters for both the x and y polarized modes. The individual components of the admittance tensor are studied as the length along L_x is systematically varied to ensure that the unit cell meets its specified requirements while also providing sufficient variability to match the impedance values presented in Fig. 4.5. First, the off-diagonal values, Y_{xy} and Y_{yx}, from Eq. 4.1 and Eq. 4.2 are varied to prove they are equal to zero. This verification is essential to confirm the feasibility of finding a solution, and the resultant zero admittance values are visually represented in Fig. 4.4. Fig. 4.4 (a) exhibits both the normalized admittances for the boundaries between dielectric to dielectric, depicted as a solid blue line, and the

boundaries between air and dielectric, illustrated by a dashed red line. The scaling of the y-axis in this plot is intentionally minimized to emphasize the close proximity of the admittance values to zero across all lengths of L_x. These minute values are indicative of the metascreen's ability to function independently, as there is negligible coupling between the two modes.

The admittance database as L_x is increased is looked at for both Y_{xx} and Y_{yy} in Fig. 4.4 (b)-(c) for both medium interfaces. As expected, the Y_{yy} is constant value across all lengths of L_x for both the interfaces of air to dielectric and for dielectric to dielectric. This consistent flat line indicates that changes in the unit cell's geometry, intended to vary the admittance for an x-polarized wave, do not have any impact on the admittance for the orthogonal polarization (y-polarized wave). This observation reaffirms the independence of these two modes. Again, this also confirms the independence of the modes. Accordingly, there is a smooth gradient of increasing admittance values over the lengths of L_x when the unit cell is excited with an x-polarized wave that encompasses the full range of values to match to the theoretical values. This admittance database in Fig. 4.4 (c) is the same that is used for Y_{yy} for the design of the metascreen as well.

The theoretical admittance values are examined and shown as the solid, blue line in Fig. 4.5. Using the admittance profile in Fig. 4.4 (c), the unit cell geometries are chosen to match the necessary admittances to create the phase discontinuity. The unit cells utilized on the screen for a design of 20° for both layers is conveyed in Fig. 4.5. Each individual unit cell's admittance is represented by a red dot. Notably, the unit cells closely approximate the theoretical values, aligning well with nearly every point across the modulation period. However, there is a slight deviation in the last unit cell of the Y_1 profile. This discrepancy arises from the asymptotic nature of the tangential function in the theoretical design, and the chosen geometry's inability to reach the required admittance value at that specific point. To address this asymptotic behavior,

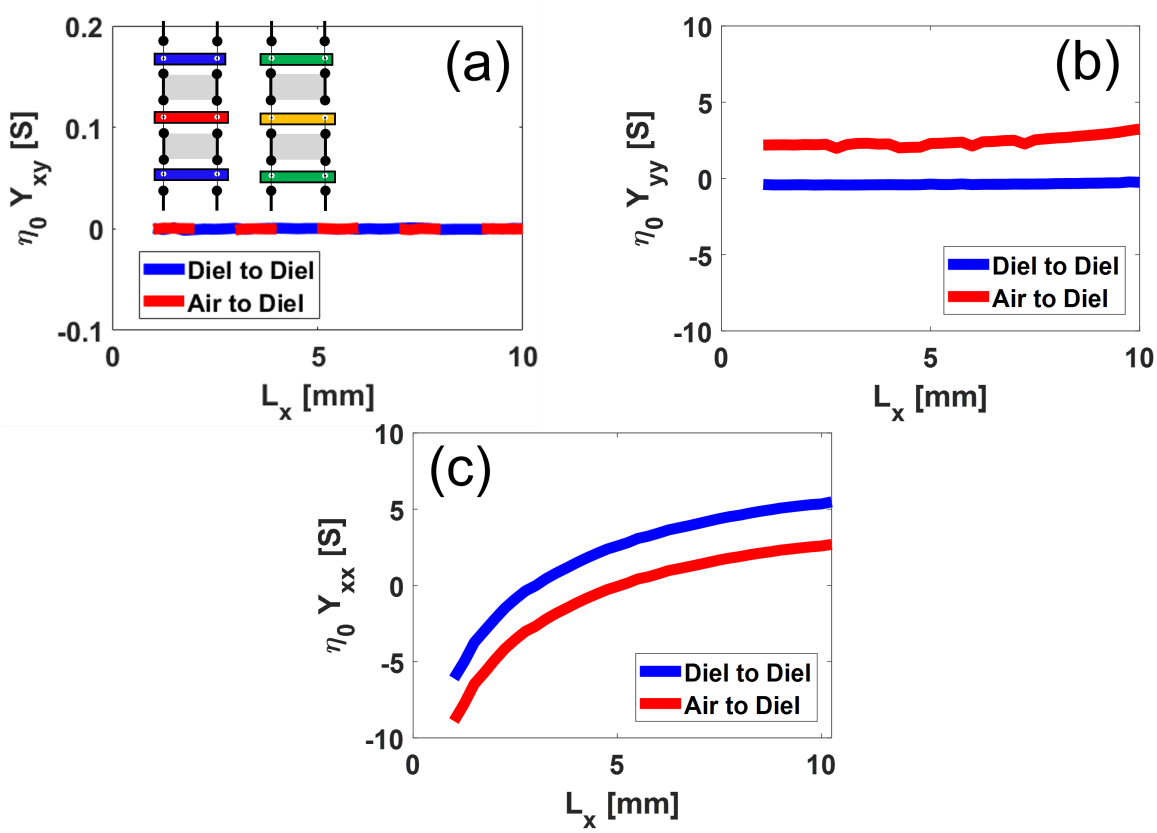

Figure 4.4: a) Normalized admittance, Y_{xy}, across the variations of L_x showing to be 0 for all values, Inset: Transmission lines for each polarization shown to be independent of each other (b) Normalized admittance, Y_{yy} across all variations of L_x illustrating the cross-pol admittance does not change based on variation of the co-pol geometry (c) Database of impedance values for both x and y polarized waves.

a phase shift is introduced, ensuring that the modulation period begins and ends with the asymptotes. This strategic placement of asymptotes at the modulation period's endpoints eliminates abrupt jumps in the admittance. Moreover, these asymptotes are conveniently positioned where the electric field across the modulation period exhibits the lowest magnitude.

4.3 Simulation and Analysis of the Full Metascreen

The full simulated metascreen is constructed using 77 unit cells which corresponds to 7 modulation periods for a design of 30° and just over 5 modulation periods for a design of 20°. The modulation periods are aligned such that one is centered in the

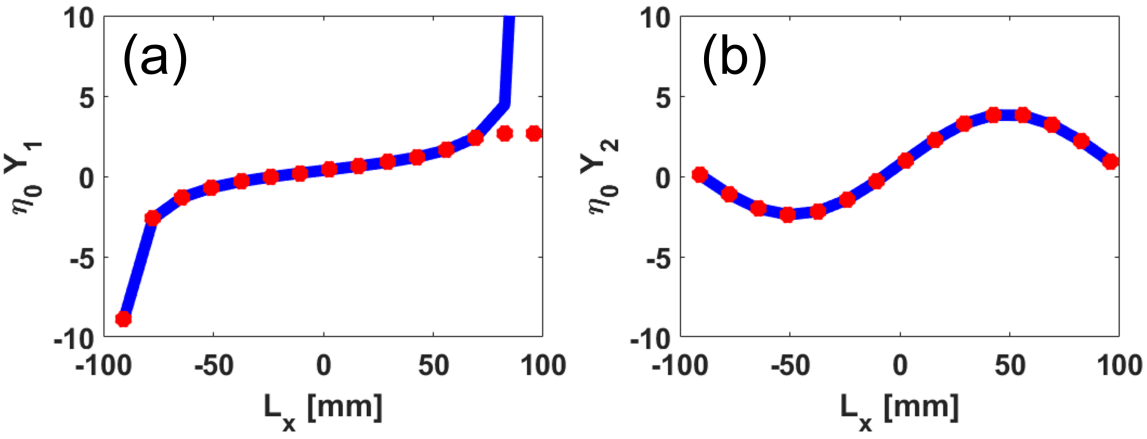

Figure 4.5: (a) Theoretical admittance value (solid, blue line) for a steering angle of 20° and the admittance value of the unit cells used (red dots) for Y_1 (b) Theoretical admittance value (solid, blue line) for a steering angle of 20° and the admittance value of the unit cells used (red dots) for Y_2

middle of the screen and repeated out towards the edges. Using Comsol's Electromagnetics simulator, the entire metascreen, spanning just over a meter in length, is positioned within a parallel plate waveguide. This configuration allows the excitation of orthogonal polarizations. Excitation is achieved at the center of the metascreen using a Gaussian beam. The radius of this beam varies depending on the size of the modulation period, which, in turn, changes with different steering angles. The results of the simulation are illustrated in Fig. 4.6, depicting the behavior of the x-polarized and y-polarized waves as they steer at angles of 20° and 30°, respectively.

The results are quite evident in illustrating the results of the Gaussian beam incident on the metascreen, as denoted by the three black lines at the center of the graphic. Notably, this incident beam undergoes an abrupt phase shift at the interface, effectively steering the angle in the intended direction. It is worth observing how the field spreads and how the design angle influences the scattering of transmitted fields. As the design angle increases, there is an inverse relationship with the size of the modulation period, primarily due to a $1/\sin(\theta)$ dependency. Consequently, for higher angle designs, there are fewer unit cells within each modulation period, leading

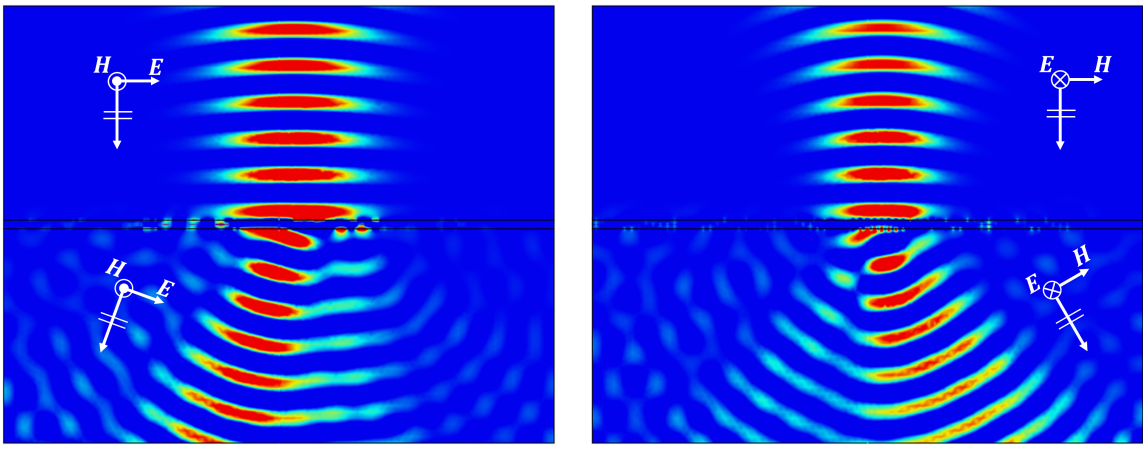

(a) (b)

Figure 4.6: (a) Gaussian beam excited electric field incident of a screen steered at an angle of 20° for an x polarized wave (b) Gaussian beam excited electric field incident of a screen steered at an angle of 30° for an y polarized wave

to increased scattering resulting from the non-continuous discretization of the admittance. Nevertheless, the metascreen's efficiency remains adequate for a wide range of angles, only becoming a limiting factor at more extreme steering angles.

In this chapter, the design and simulation of a metascreen for beam steering purposes are thoroughly explored. The selection of a slotted modified Jerusalem cross as the unit cell geometry is explained, emphasizing its advantages in achieving simplicity, symmetry, structural integrity, and the ability to vary impedance. The study employs Floquet analysis with periodic boundaries to obtain scattering parameters and extract the admittance values for both x and y polarized modes. Notably, the investigation ensures the independence of modes by confirming zero off-diagonal admittance values and reveals smooth variations in admittance along the length. The results of the full simulated metascreen demonstrate effective beam steering capabilities, with efficiency remaining acceptable for various angles.

CHAPTER 5: DUAL BAND METASURFACE ANTENNAS

The demand for multifrequency medium-to-high gain antennas is rapidly increasing in many application areas, including Earth and climate science, remote sensing, and satellite communications. These antennas, which are able to operate at different frequency bands with the same shared aperture, offer the possibility to increase the channel capacity, improve the isolation between the transmitted and received signals, and provide multiple functionalities.

Reflectarrays [40, 41, 42, 43, 44, 45] and transmitarrays [46, 47, 48, 49, 50, 51] have been largely explored as radiators operating in multiple frequency bands. Among other advantages, these antenna solutions are low cost, low weight, and ease of fabrication. However, they usually require an external feed, which makes them less appealing for applications with severe space constraints. Thus, it is of significant interest to propose multifrequency antenna solutions with an integrated feed.

Metasurface antennas have raised a great deal of interest in recent years [52, 53, 54, 55, 33, 56, 57]. Key features they offer include lightweight, ultra-thin form factor, polarization control, and a simple feeding mechanism. In the simplest cases, the feed structure is a vertical monopole placed inside the slab and coaxially powered from the ground plane. The monopole located at the center of the antenna excites a cylindrical surface wave that is gradually converted into a radiative wave, known as a leaky wave, through the interaction with the periodic metallic texture. The metallic texture can be modeled by a spatially modulated surface impedance [58]. This impedance relates tangential components of the electric and magnetic fields and is usually assumed to be purely imaginary (reactive), implying lossless metallic elements which is a reasonable assumption in the microwave and millimeter-wave regimes. As stated by the Foster's

Reactance theorem, such a reactance must be a monotonically increasing function of the frequency alternating poles and zeros [59].

In this chapter, the investigation of a new strategy for designing dual-frequency MTS antennas is based on exploiting the behavior of the MTS surface impedance versus frequency. Previous research on dual-band MTS antennas has typically relied on two different strategies. The first strategy involves superimposing two different modulated surface impedances, with each one responsible for controlling radiation at a specific frequency [60, 61]. This approach requires subwavelength unit cells to accurately discretize the continuous impedance profile, making it challenging for radiative systems operating at two widely separated frequency bands. The second strategy involves cascading two surface impedances whose profiles are determined using the optimization technique of the gradient-descent method [62].

While this approach potentially has no restriction on the separation between the two operating frequencies, it requires an external excitation, resulting in a poor device form factor. In this proposed antenna, it allows overcoming such issues. It consists of a dual-layered MTS antenna capable of performing at two broadly different frequencies with a coplanar excitation. The key point in this dissertation is to make the layer working at the frequency f_1 transparent at the frequency f_2, and vice-versa. As mentioned above, this behavior can be achieved by exploiting the Foster's Reactance theorem. Namely, the equivalent impedance of the metallic layer operating at f_1 (f_2) has to be close to a pole at f_2 (f_1).

The work begins with a concise review of the design principles for single-layered MTSs intended to operate within a single frequency band. This serves as a foundation for the subsequent stages of the analysis, which initiates with the design and examination of a single-layered, single-frequency x-polarized antenna. This initial step accelerates the process, aiding in the understanding of simulation and fabrication limitations. The subsequent sections expand upon Foster's Reactance theorem

to facilitate the design of double-layered MTS antennas capable of functioning across two distinct frequency bands. The research provides a practical implementation of this approach, wherein a double-layered MTS antenna designed to emit circularly polarized broadside beams at two commonly used frequencies in cloud and precipitation radar applications, namely 35.75 GHz and 94.05 GHz, is developed. The antenna's performance is rigorously verified through full-wave simulations, ensuring its effectiveness and suitability for the specified dual-frequency operation in cloud and precipitation radar systems [63].

An $e^{j\omega t}$ time convention is used and suppressed throughout.

5.1 Single Frequency Anisotropic Antenna

Firstly, a concise overview is presented on the fundamental principles involved in designing single-layered MTS antennas. Building upon these principles, an initial antenna design is introduced, which serves as the foundation for further development into a dual-band, dual-layered antenna configuration.

The design of single-layered MTS antennas is rooted in a two-dimensional (2D) canonical problem, as depicted in Fig. 5.1(a). This problem comprises a periodically modulated impedance sheet situated on a dielectric substrate that is backed by a metallic ground plane. The structure is assumed to exhibit invariance along the y direction. The dielectric slab's relative permittivity, ε_r, and thickness,h, are denoted by their respective symbols. Typically, the impedance sheet is characterized by a cosine or cosinusoidal function.

$$Z_s(x) = -jX_s(x) = -jX_0\left(1 + M\cos\left(\frac{2\pi x}{d}\right)\right) \tag{5.1}$$

In this equation, X_0 represents the average impedance (with $X_0 > 0$), M is the modulation index, and d is the modulation period. Due to the periodic nature of X_s, the solution of the 2D canonical problem can be represented through an infinite

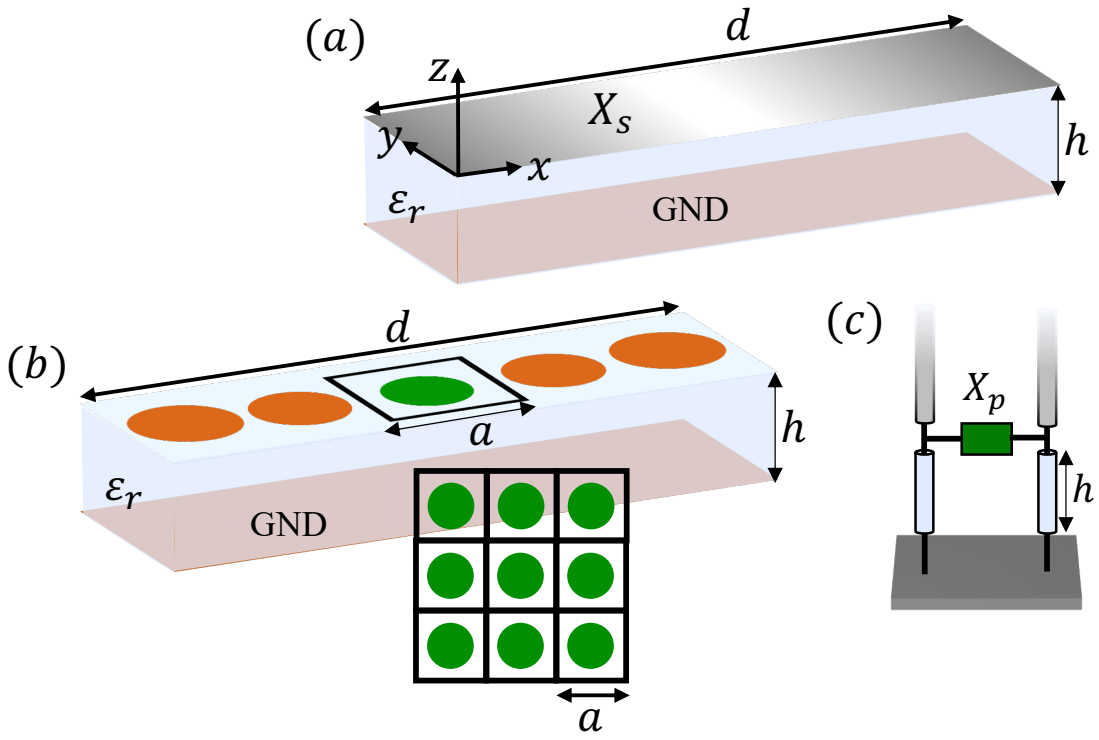

Figure 5.1: (a) A 2D canonical problem consisting of a penetrable sinusoidally modulated surface impedance (Z_s) on top of a grounded dielectric slab. The geometry is assumed to be invariant along the y-direction and spatially variant along the x- and z-directions. (b) Z_s is conceptually implemented through gradually varying subwavelength patches. The inset shows the locally periodic problem utilized to map the patches into an equivalent impedance (Z_p) through (c) the local transmission line model.

set of Floquet modes (FMs) [5, 58]. The longitudinal (along x) wavenumber of the n-indexed FM is

$$k_x^{(n)} = k_x^{(0)} + \frac{2\pi n}{d} \tag{5.2}$$

where $k_{x,0}$, which is the solution of the dispersion equation, is the propagation constant of the 0-indexed TM FM. For d larger than a critical value [5], at least one of the higher-order FMs ends up inside the light cone, and leaky waves occur. In this case, the solution of the dispersion equation takes a complex value and can be represented as

$$k_x^{(0)} = \beta_{sw} + \Delta\beta - j\alpha \tag{5.3}$$

The positive real numbers $\Delta\beta$ and α account for the perturbation in the phase and amplitude, respectively, induced by the modulation into the surface wave propagating in the unmodulated surface impedance ($M = 0$) with wavenumber β_{sw}. The period (d) of modulated surface impedances modeling MTS antennas is usually selected such that only the (-1)-indexed FM is inside the light cone. As a result, the pointing angle (θ), which is defined with respect to the z axis, and d are related as follows

$$\beta_{sw} + \Delta\beta - \frac{2\pi}{d} = k\sin\theta \tag{5.4}$$

with k being the free-space wavenumber.

To accurately synthesize the desired continuous impedance profile, the approach involves the use of subwavelength metallic patches that smoothly vary along the surface, as illustrated in Fig. 5.1(b) [58]. The gradual variation of the patches allows using the local periodicity approximation. Namely, the equivalent impedance of each patch can be extracted as it was embedded in a periodic environment [inset of Fig. 5.1(b)]. A periodic pattern modeled with the transmission line shown in Fig. 5.1(c) is studied to build databases linking the equivalent impedance ($Z_p = jX_p$) with the geometrical parameters of the unit cell. Various techniques for efficiently and accurately extracting impedance from periodic metallic patches printed on a grounded slab are available in the published literature. These techniques can be found in references such as [64, 65, 66].

5.1.1 Designing a Single-Layer MTS Antenna for 94.05 GHz Operation

The initial focus under investigation is a linearly polarized single-layered MTS antenna designed for operation at 94.05 GHz. Starting with the single-layer antenna at the higher frequency allows the assessment of the limitations of simulation capabili-

ties and the feasibility of fabrication. Adding a second layer will introduce significant complexity to the computational efforts, making it more challenging to evaluate these factors effectively.

In the design of the initial single-layer antenna, a method suitable for a single-layer anisotropic antenna is employed to create an x-polarized antenna capable of operating at 94.05 GHz. The introduction of anisotropy into the surface impedance is a key factor in enhancing the antenna's efficiency, as it enables greater directivity in the main lobe compared to the side lobes. The surface impedance can be mathematically expressed using the tensor-based representation as $\overline{\overline{\boldsymbol{X}}} = X_{\rho\rho}\hat{\boldsymbol{\rho}}\hat{\boldsymbol{\rho}} + X_{\rho\phi}(\hat{\boldsymbol{\rho}}\hat{\boldsymbol{\phi}} + \hat{\boldsymbol{\phi}}\hat{\boldsymbol{\rho}}) + X_{\phi\phi}\hat{\boldsymbol{\phi}}\hat{\boldsymbol{\phi}}$ [67]. This tensor-based representation allows for an accurate description of the impedance properties of the antenna.

The aspects of the tensor can broken into its components in the equations below.

$$X_{\rho\rho} = \overline{X}_{\rho}\left[1 + m_{\rho}(\boldsymbol{\rho})\cos(Ks(\boldsymbol{\rho}) + \Phi_{\rho}(\boldsymbol{\rho}))\right] \tag{5.5}$$

$$X_{\rho\phi} = \overline{X}_{\rho} m_{\phi}(\boldsymbol{\rho})\cos(Ks(\boldsymbol{\rho}) + \Phi_{\phi}(\boldsymbol{\rho})) \tag{5.6}$$

$$X_{\phi\phi} = \overline{X}_{\phi}\left[1 - m_{\phi}(\boldsymbol{\rho})\cos(Ks(\boldsymbol{\rho}) + \Phi_{\phi}(\boldsymbol{\rho}))\right] \tag{5.7}$$

With the equations provided, it becomes possible to generate the physical layout required for antenna design. By assigning a tapered modulation determined through [33, 68] and aiming for an average impedance of approximately -270 Ω, the plots for $X_{\rho\rho}$, $X_{\rho\phi}$, $X_{\phi\rho}$, and $X_{\phi\phi}$ can be constructed as illustrated in Fig. 5.2. These plots serve as a crucial reference for shaping the surface impedance profile and are essential for achieving the desired antenna performance.

This transparent, lossless reactance tensor nicely describes the surface impedance that will provide the antenna with the appropriate pointing angle. As shown in Fig. 5.2, the antenna needs a large range of impedance values to be able to cover the theoretical impedance values meaning that a large database is needed to fulfill the

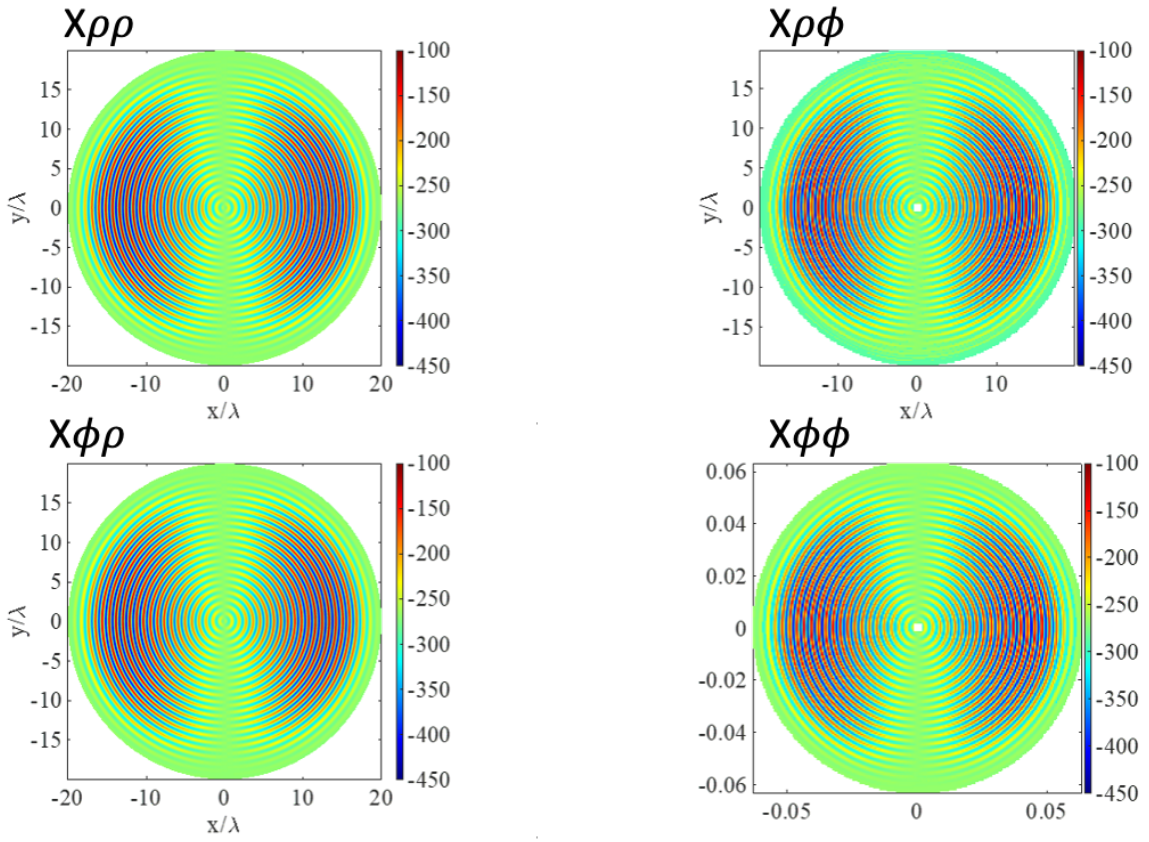

Figure 5.2: In order from top left to bottom right, $X_{\rho\rho}$, $X_{\rho\phi}$, $X_{\phi\rho}$, $X_{\phi\phi}$, for the impedance tensor for the single layer, x polarized antenna with a 20λ radius designed for 94.05 GHz

full range of values. This also means that the unit cells used to realize this antenna needs to have some complexity to introduce a full range of capacitance values within the desired range. The unit cell chosen that is capable of this behavior is a double π shape [69]. The full unit cell is shown in Fig. 5.3 with its dimensions of L_x, L_x, w, w_1, and ψ with a unit cell period of d with it residing on a dielectric slab with a height, h_d. Here, it shown that the height of the dielectric is 203 μm and has an ε_r of 3.55. The material chosen as the dielectric for the patches to reside of is Rogers 4003c which has relative permittivity as shown and can be manufactured as small as 203 μm. At this height of dielectric, only one mode is able to propagate. In addition to the design aspect of the height, the unit cell period, d, is set to 580 μm so the

antenna will radiate broadside.

The last design element is varying the dimensions of the unit cell to create the impedance range covered in Fig. 5.2. To achieve the variation needed to meet the specifications for the impedance, the database is made by varying the lengths L_x and L_y, as well as the rotation of the metallic patch itself.

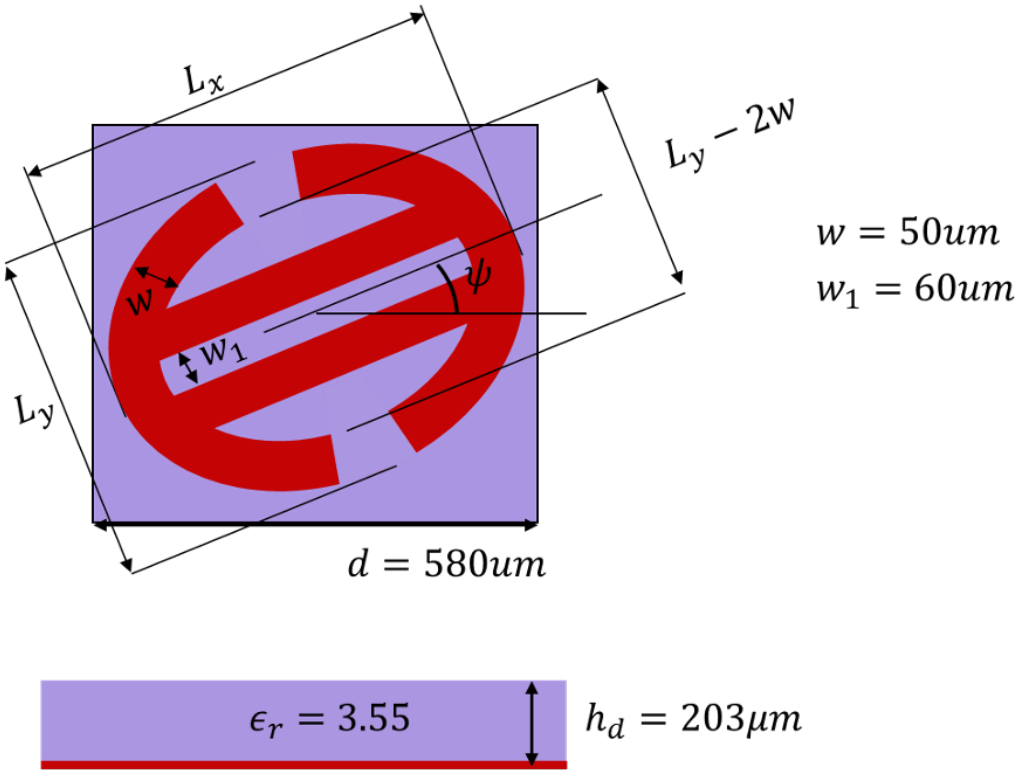

Figure 5.3: Double π shaped unit cell used to fulfill the required impedance range in order to make a linearly polarized antenna at 94.05 GHz

Given the variation of three parameters of the two lengths and rotation, the database becomes three-dimensional and covers a very large range of values suitable to design the antenna. Fig. 5.4 provides the completed database for all the components of the impedance including $X_{\rho\rho}$, $X_{\rho\phi}$, and $X_{\phi\phi}$.

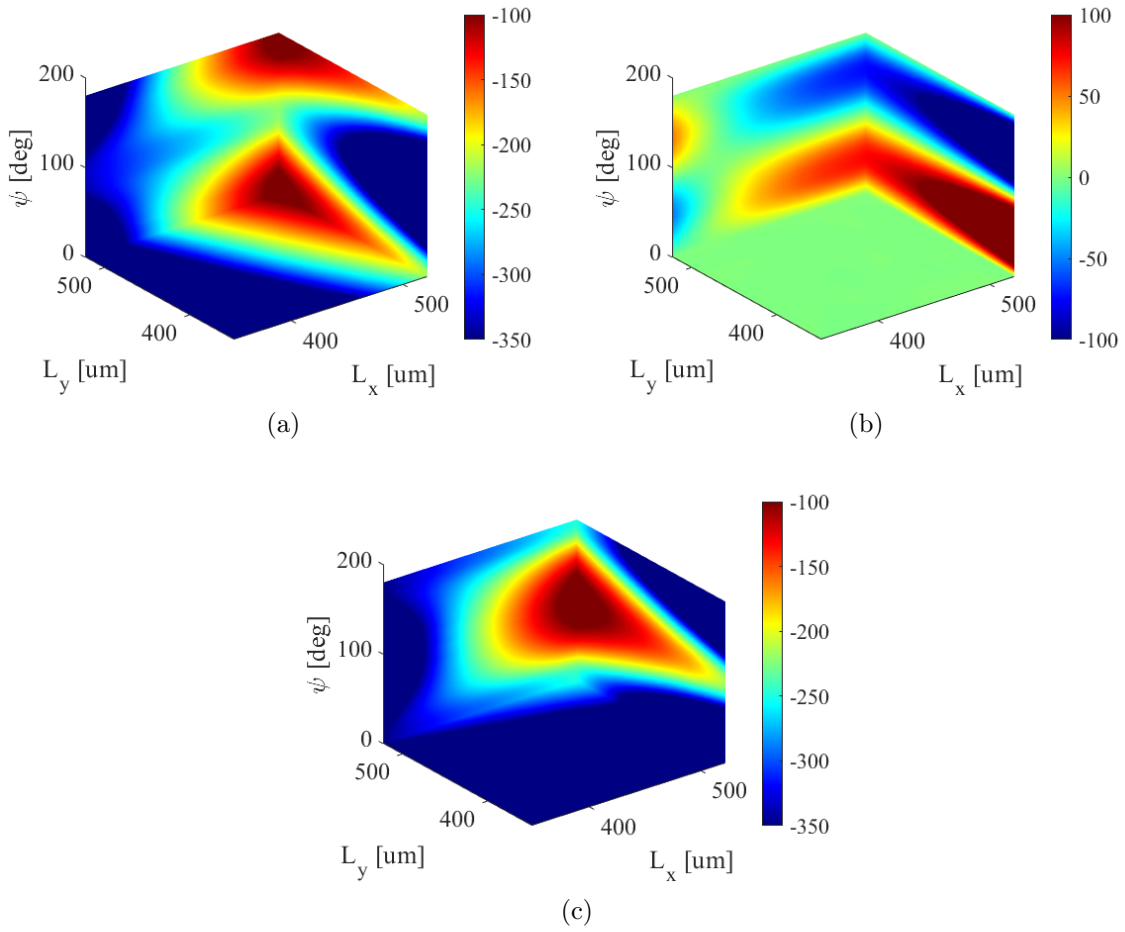

Figure 5.4: The impedance database elements, (a) $X_{\rho\rho}$, (b) $X_{\rho\phi}$, (c) $X_{\phi\phi}]$, in terms of length in x and y and ϕ for the anisotropic 94.05 GHz antenna

5.1.1.1 Accommodating Effects of Spatial Dispersion

In the initial antenna design, it was assumed that all unit cells would encounter an incident wave perpendicular to them. The error in a quarter of $X_{\rho\rho}$ can be observed in Fig. 5.5, illustrating an increase in error towards the center and a subsequent decrease as it approaches the orthogonal side. This behavior highlights the dependence on spatial dispersion.

When applying this design to the complete antenna, the actual radiation behavior did not align with the initial predictions. This discrepancy indicated a strong dependence on the lattice structure. In response to the lower-than-expected direc-

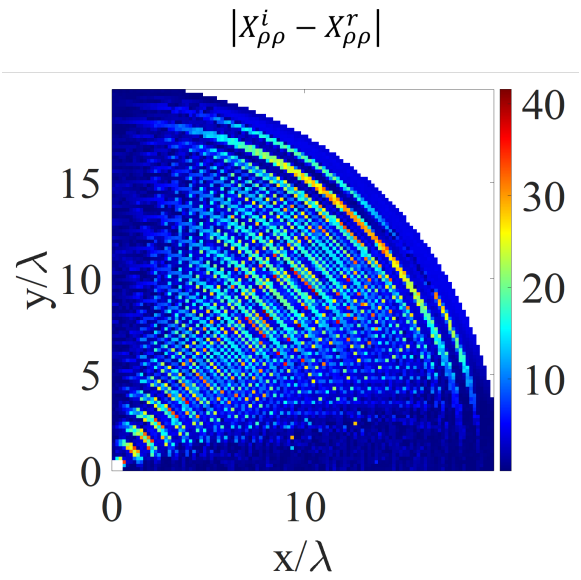

Figure 5.5: Error of one quarter of $X_{\rho\rho}$ when spatial dispersion is neglected

tivity, a new objective was established: designing the antenna in a way that makes the impedance of the unit cells dependent on the angle of the incident wave. This concept is illustrated in Fig. 5.6, which provides examples of four different unit cells.

This approach considers that the placement of the unit cell on the antenna has a significant influence on how the incident wave interacts with it. As a result, this approach effectively reduces errors, as illustrated in Fig. 5.7 for $X_{\rho\rho}$, $X_{\rho\phi}$, and $X_{\phi\phi}$.

To account for the lattice dependency, the antenna was divided into sixteen distinct slices of the phase, effectively discretizing the dispersive sections. This choice of sixteen sections was made to strike a balance between maintaining accuracy with small increments and providing granularity for designing a database for each section. In Fig. 5.8, the diagram illustrates the different colored sections, representing the sixteen divisions in which the antenna is segmented. The dotted line at the center of each colored section signifies the value used to describe the corresponding phase slice for that particular section. This partitioned phase approach allows for the incorporation of lattice dependency into the antenna design.

Combining the database and the partitioning of the phase to achieve spatial disper-

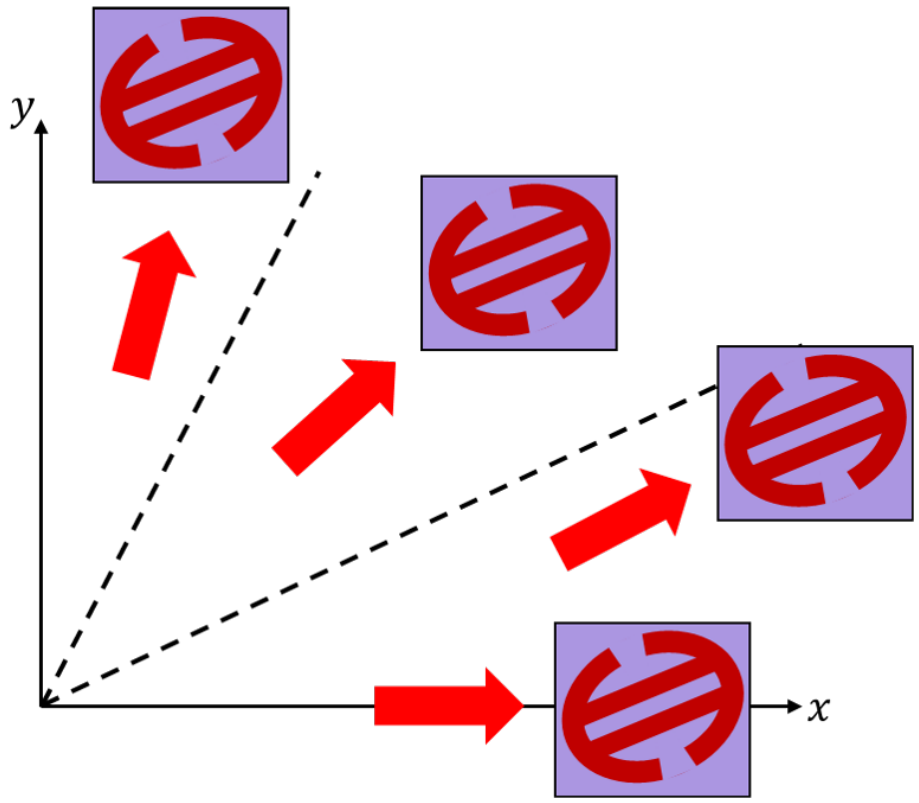

Figure 5.6: Examples of the different angles of incidence needed due to the lattice dependency of the unit cells.

sion, the unit cells are constructed for a design of 10λ seen in Fig. 5.9a with the error in Fig. 5.9b. As shown, the error for the antenna is mostly under 5Ω and the max is under 30Ω showing that the database is efficient and should produce an effective antenna.

Using Ansys's High Frequency Structure Simulator (HFSS), the antenna is excited by a Hertzian dipole centered in the middle of the antenna and positioned at the center of the dielectric. The results regarding the antenna's directivity are presented in Fig. 5.10. It is worth noting that the antenna is originally designed to operate optimally at 20λ, but for computational reasons, it was simulated with a radius half its intended size. Consequently, the directivity is lower compared to what it would achieve with a design based and optimized on a radius of 10λ. Despite this limitation, the antenna still demonstrates the proof of concept effectively. It produces

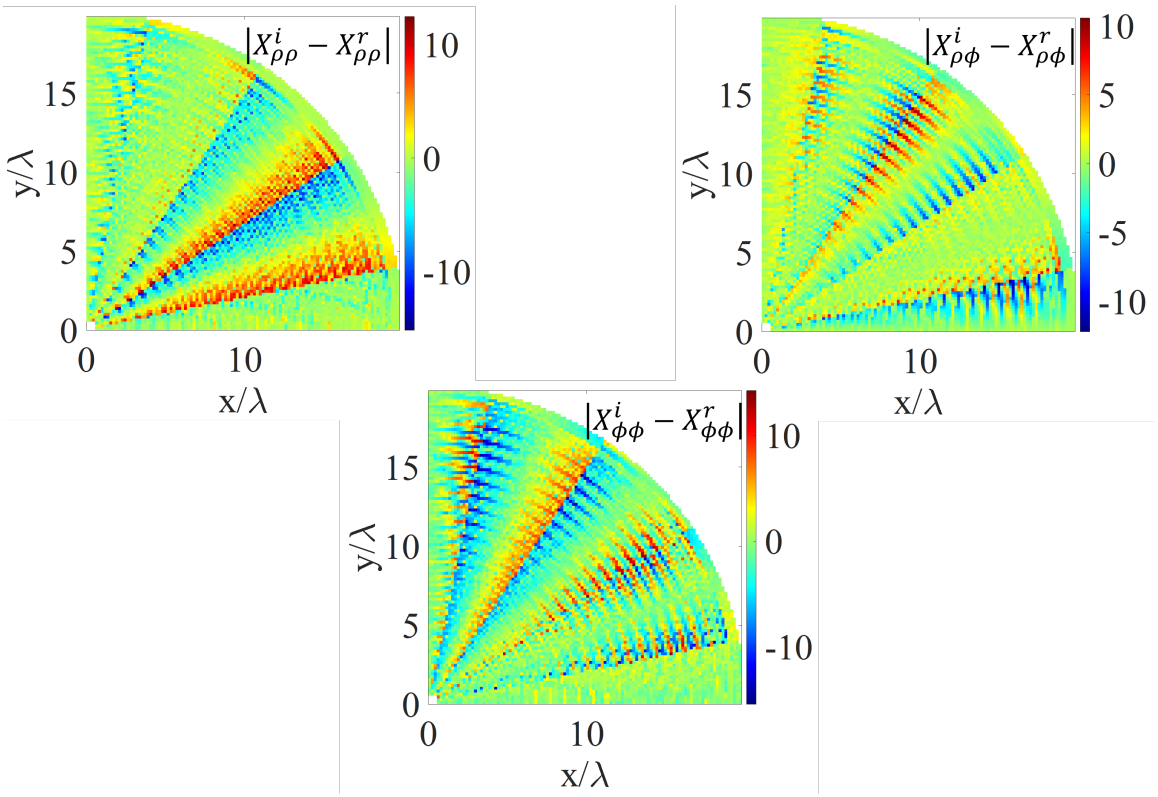

Figure 5.7: Error of one quarter of $X_{\rho\rho}$, $X_{\rho\phi}$, and $X_{\phi\phi}$ when spatial dispersion is considered.

a directivity pattern that, although not reaching its full potential, remains relatively high it exhibits low side lobes.

To ensure the method's efficiency in designing high-efficiency antennas with either linear or circular polarization, smaller antennas were designed, not constrained by computational limitations. Continuing with the linearly polarized antenna, one with a radius of 5λ was designed to incorporate attenuation tapering, resulting in a radiation pattern with 45% efficiency. The tensorial impedance values, namely $X_{\rho\rho}$, $X_{\rho\phi}$, and $X_{\phi\phi}$, required to achieve the desired attenuation, are illustrated in Fig. 5.11.

The radiation pattern of the linearly polarized antenna is visualized in Fig. 5.12, offering several significant insights. Firstly, the efficiency of this antenna design is approximately 25%. This efficiency level can be ascribed to the intrinsic limitations of linear polarization in achieving complete anisotropy. Secondly, the cross-polarization,

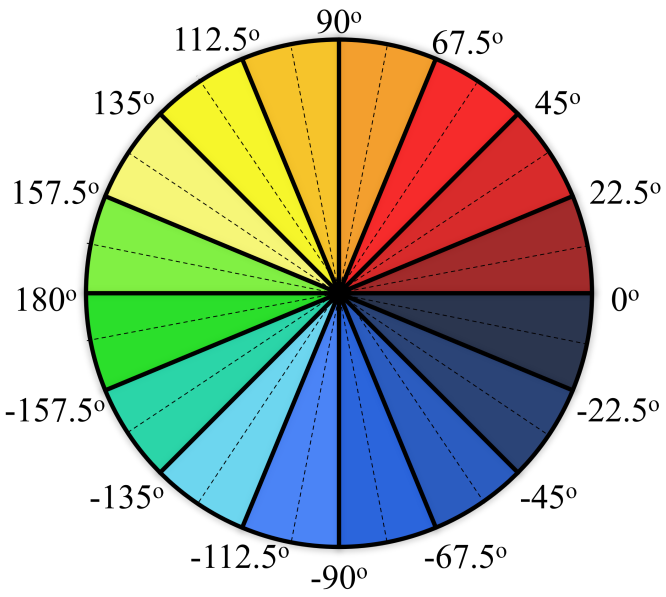

Figure 5.8: The antenna is partitioned into phase sections where each section is indicative of the angle of propagation due to the lattice dependency. Each color represents a different section of one angle and it calculated using the center of the area notated by the dotted line.

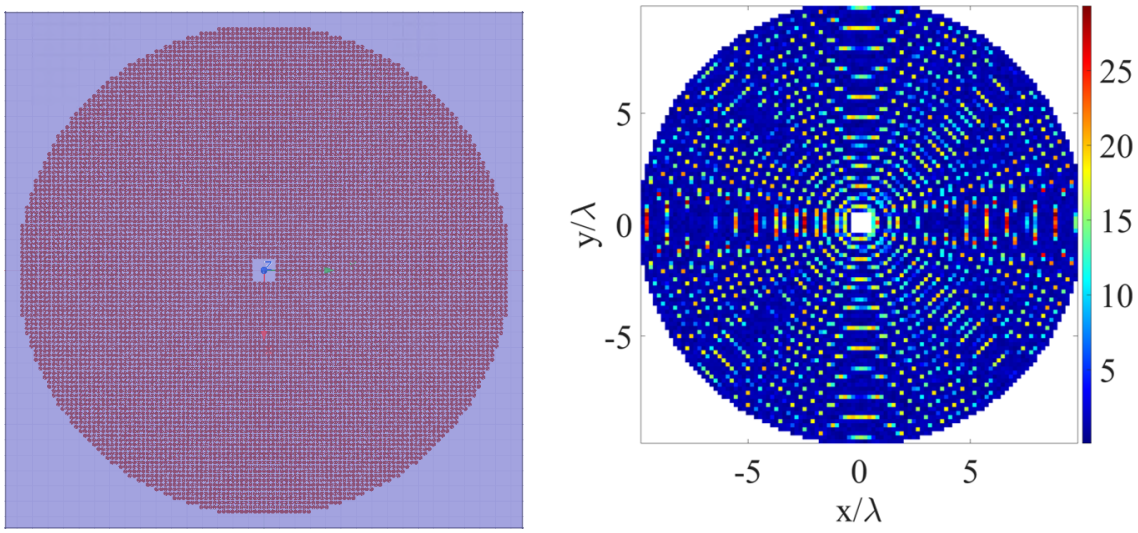

(a) (b)

Figure 5.9: (a) Top view of the single layer, anisotropic, MTS antenna designed for 94.05 GHZ with a radius of 10 λ sitting on a dielectric slab with a thickness of 203 μm and excited with a Hertzian dipole at the center and middle of the dielectric. (b) The error of the impedance of the unit cells used in (a) in comparison to the required impedance values

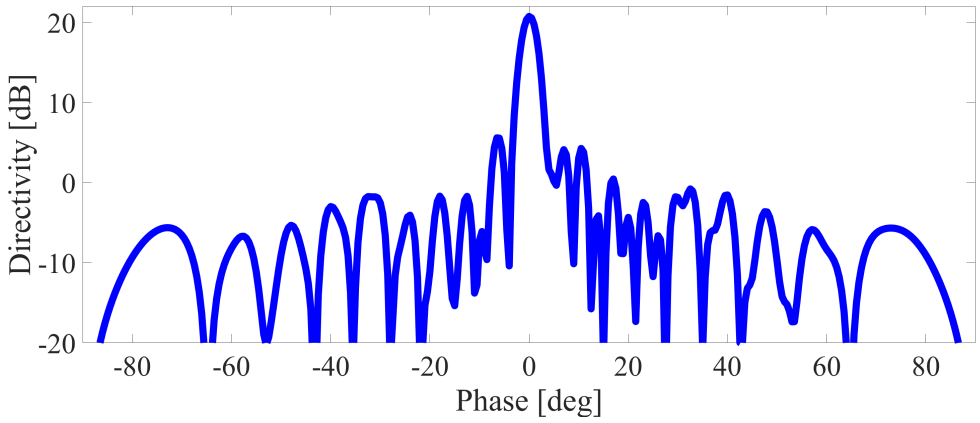

Figure 5.10: The directivity results in the x direction of the antenna in the Fig. 5.9a excited with a Hertzian dipole

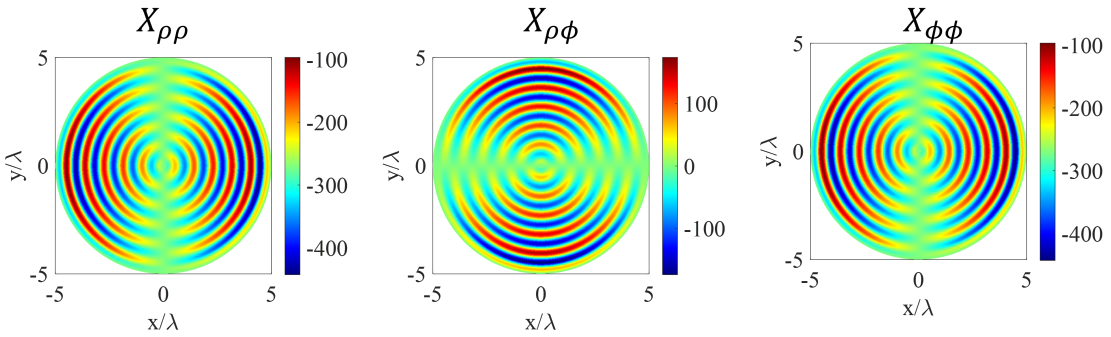

Figure 5.11: $X_{\rho\rho}$, $X_{\rho\phi}$, and $X_{\phi\phi}$ for a linearly polarized antenna designed to have a radius of 5λ and efficiency of 45%

which is around -25dB at the broadside direction, is so minimal that it does not even appear on the plot.

To illustrate that this unit cell and design approach can also be adapted for circular polarization, another antenna of the same size has been designed. This circularly polarized antenna shares similar size and efficiency parameters with the 5λ linearly polarized antenna. The impedance values required for the circularly polarized antenna are shown in Fig. 5.13.

The directivity of the circularly polarized antenna is depicted in Fig. 5.14. It is evident that the efficiency has improved, although this enhancement comes at the expense of cross-polarization, which still remains lower compared to the co-polarization.

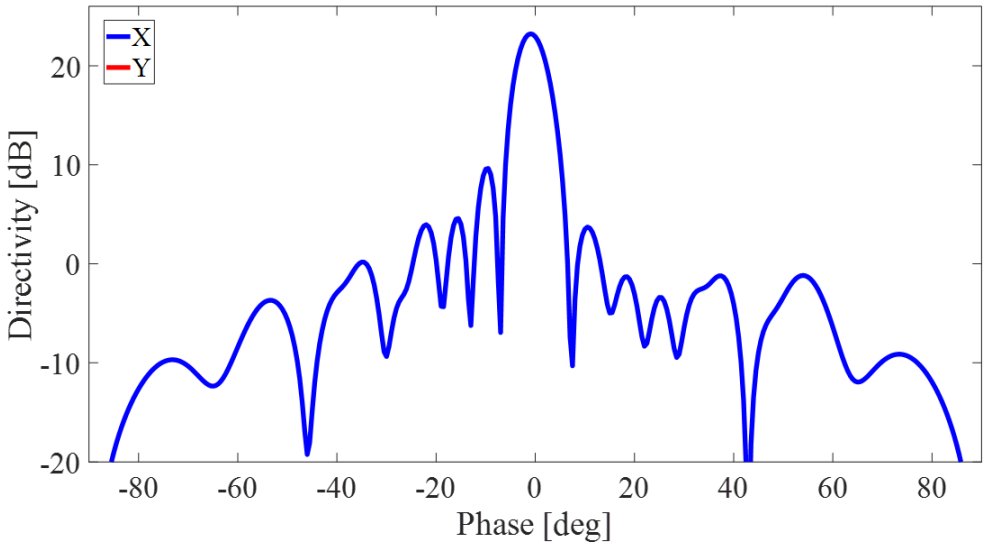

Figure 5.12: Directivity of a linearly polarized antenna optimized for a radius of 5λ and designed to have an efficiency of 45% using the double π unit cell.

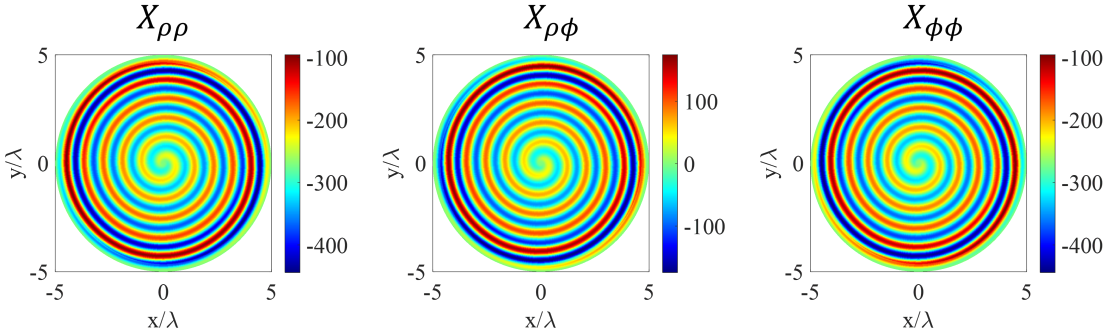

Figure 5.13: $X_{\rho\rho}$, $X_{\rho\phi}$, and $X_{\phi\phi}$ for a circularly polarized antenna designed to have a radius of 5λ and efficiency of 45%

5.2 Dual Band Metasurface Antenna

The next phase in the development of this antenna involves the incorporation of a second frequency by adding a second layer. This enhancement is explored within the context of a circularly polarized dual-layer antenna, where the impedance is changed to isotropic, and the polarization is designed to be circular. This design modification simplifies the antenna's structure and behavior. Simultaneously, the antenna from the previous section continues to be developed and optimized. Both aspects-designing the

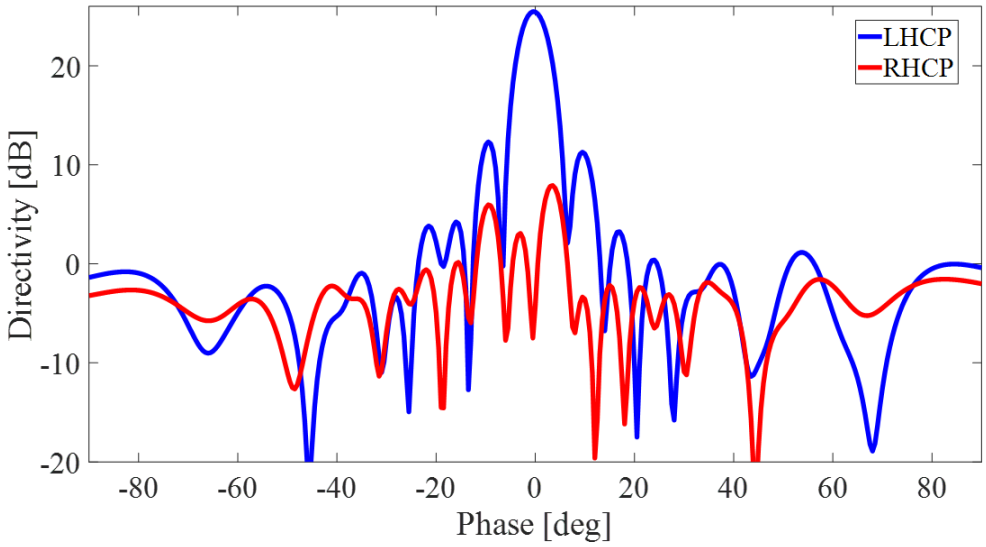

Figure 5.14: Directivity of a linearly polarized antenna optimized for a radius of 5λ and designed to have an efficiency of 45% using the double π unit cell.

dual-layer, dual-frequency antenna and refining the single-layer antenna are pursued in parallel, ensuring efficient progress in both areas. Each component of the antennas is carefully designed and fine-tuned to achieve the desired performance objectives. Ultimately, the findings and outcomes from both aspects will be combined to create the final prototype of the dual-layered, dual-frequency antenna, offering enhanced functionality and broader operational capabilities.

5.2.1 Foster Reactance Theorem For Dual Layer Design of Two Distant Frequencies

The ability to operate with two vastly different frequencies is accomplished through layering two individually designed MTS layers and placing the lower frequency MTS on top of a dielectric and embedding the second MTS of the higher frequency in the middle of the dielectric. It can be assumed that there are two canonical problems shown in Figs. 5.15(a) and (b). The first one [Fig. 5.15(a)], which is identical to that shown in Fig. 5.1(a) with a surface reactance sheet X_{s1} and slab thickness h_1, is set up to perform at f_1 with a pointing angle θ_1. The second one [Fig. 5.15(b)] is

slightly different than the previous one. That is, the sinusoidally modulated reactance sheet (X_{s2}) is embedded in the dielectric slab and located at a distance h_2 from the ground plane, with $h_2 < h_1$. However, its design principle remains unchanged and it is set up to operate at f_2 with a pointing angle θ_2. The two reactance sheets can be implemented by gradually changing subwavelength patches [see Figs. 5.15(c) and (d)]. Each patch is linked to an equivalent impedance through the local periodicity approximation. The impedance can be studies using the local transmission line models as shown in the insets of Figs. 5.15(c) and (d), with X_{p1} and X_{p2} representing the equivalent impedance of the patches in a locally periodic environment.

Now, given two MTSs of Fig. 5.15(c) and (d) operating at f_1 and f_2, respectively, it is desired that their combination [Fig. 5.15(e)] is capable of performing at both frequencies of interest. At first sight, the obtained double-layered MTSs cannot perform equally well as the two single-layered MTSs. When the two metallic patterns, which have been designed independently, are placed closely one to another, it is expected they are coupled through the near-field interactions. This implies a change in the equivalent impedance of each pattern and, as a result, the radiation performances in terms of pointing angle and side-lobe level can be noticeably affected. The coupling between the metallic layers can be handled at the synthesis level of the continuous reactance sheets. The extraction of the patch equivalent reactance needs to account for the presence of the other layer. This will involve a complicated technique for impedance extraction that deviates from the well-established techniques available for the design of MTSs [64, 65, 66]. Also, it will impose a restriction on the size of the unit cells: a_1 must be a multiple integer of a_2. An alternative approach that avoids extracting impedance in double-layered periodic structures with no restrictions on the unit cell size would be preferable. The proposed approach focuses on a suitable impedance synthesis of the two single-layered MTSs [Figs. 5.15(c) and (d)] such that they perform equally well when they are combined together [Fig. 5.15(e)].

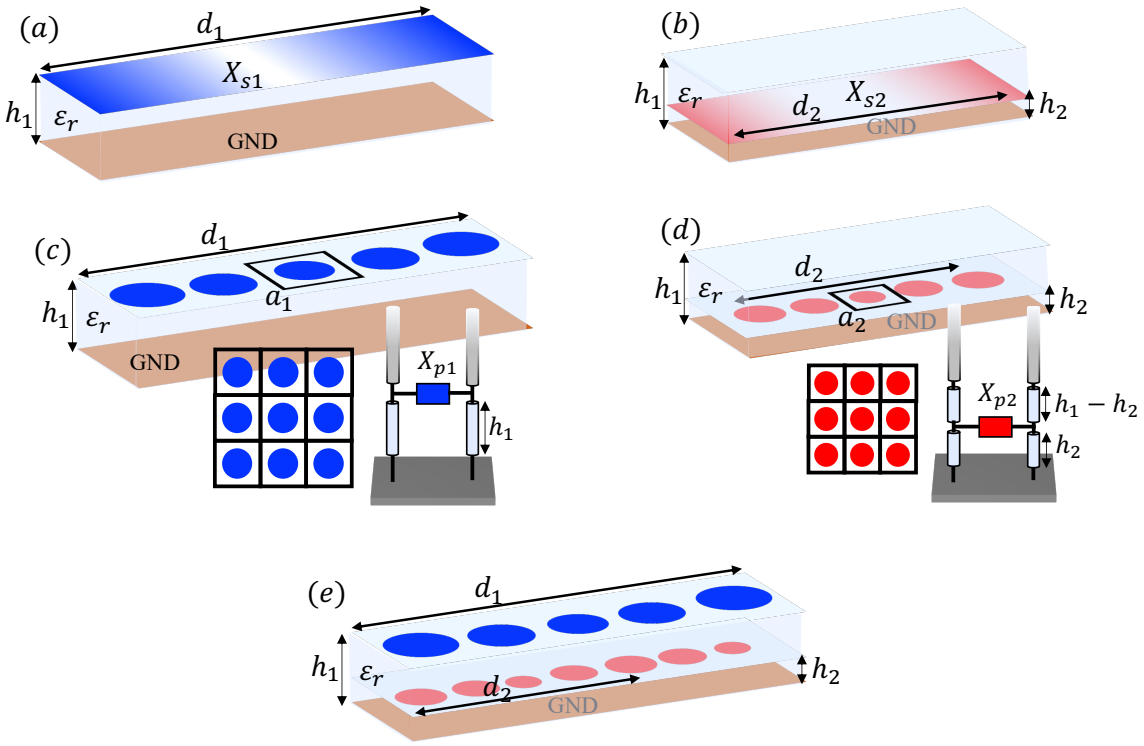

Figure 5.15: (a) and (b) 2D canonical problems operating at f_1 and f_2, respectively. (c) and (d) conceptual implementation with metallic patches. The insets in (c) and (d) show the local periodic problem and transmission line model. (e) Combination of the structures in (c) and (d) performing at f_1 and f_2.

Based on the procedure summarized in the previous section, the goal now is to develop a new methodology that allows designing two independent MTS antennas, operating at two different frequencies, that can be merged together, resulting in a single flat dual-band radiator. It is assumed that the two frequencies of interest are f_1 and f_2, with $f_1 << f_2$. Henceforth, all the frequency-dependent physical quantities introduced in the previous section are assigned with subscripts 1 and 2, corresponding to f_1 and f_2, respectively.

It is indeed well-known that the equivalent reactance provided by a periodic array of metallic patches is purely imaginary and displays a capacitive behavior in the low-frequency regime. According to Foster's Reactance theorem, in a lossless transmission line or network, the reactance changes monotonically with frequency and the poles and zeros alternate. Given the subwavelength unit cells required in the MTS

design, X_{p1} and X_{p2} reside between the first zero and the first pole. See X_{p1} and X_{p2} in Figs. 5.16(a) and (b), respectively. Now, the question is: what is the local equivalent reactance of the patches designed for f_2 (red patches in Fig. 5.15(e)) seen from the wave supported by the single-layered MTS operating at f_1 [Fig. 5.15(c)]? To address this question, X_{p2} is evaluated by forcing the local periodic problem for f_2 a TM surface wave with frequency f_1 and wavenumber β_{sw1} (see the bottom inset of Fig. 5.16(a)). This process implies extracting X_{p2} outside the dispersion curve and can be carried out through, for example, the periodic Method of Moment (MoM) described in [70]. Since $f_1 << f_2$ is assumed, a_2 will be much smaller than a_1. Thus, X_{p2} evaluated at f_1 and β_{sw1} will be very close to the pole at zero frequency, corresponding to a quasi open-circuit [Fig. 5.16(a)]. As a result, the MTS operating at f_2 [red patches in Fig. 5.15(e)] are almost transparent at f_1. The same procedure can be repeated to evaluate X_{p1} at f_2 and β_{sw2}. However, now a_1 is electrically large at f_2. The patches working at f_1 [blue patches in Fig. 5.16(b)] needs to be properly design such that X_{p1} presents a pole at f_2 becoming a quasi-open circuit [Fig. 5.16(b)]. Note that this pole will be after the first zero. It could be the second or third poles depending on the separation between f_1 and f_2. Following this strategy, the double-layered MTS of Fig. 5.15(e) obtained from the combination of the two single-layered MTSs of Figs. 5.15(c) and (d) operating at f_1 and f_2, respectively, is expected to perform at the two frequencies of interest.

Fig. 5.17 provides a clear illustration of the two distinct scenarios. The first scenario occurs when the antenna is excited at frequency f_1. At this specific frequency, the impedance experienced by the electromagnetic wave is primarily determined by the top layer, such that the metallic patches represented in blue contribute to the radiation pattern. Concurrently, the embedded patches within the dielectric exhibit extremely high impedance, resembling an open circuit. This behavior aligns with Foster's Reactance Theory, where the reactance demonstrates poles near the asymptote.

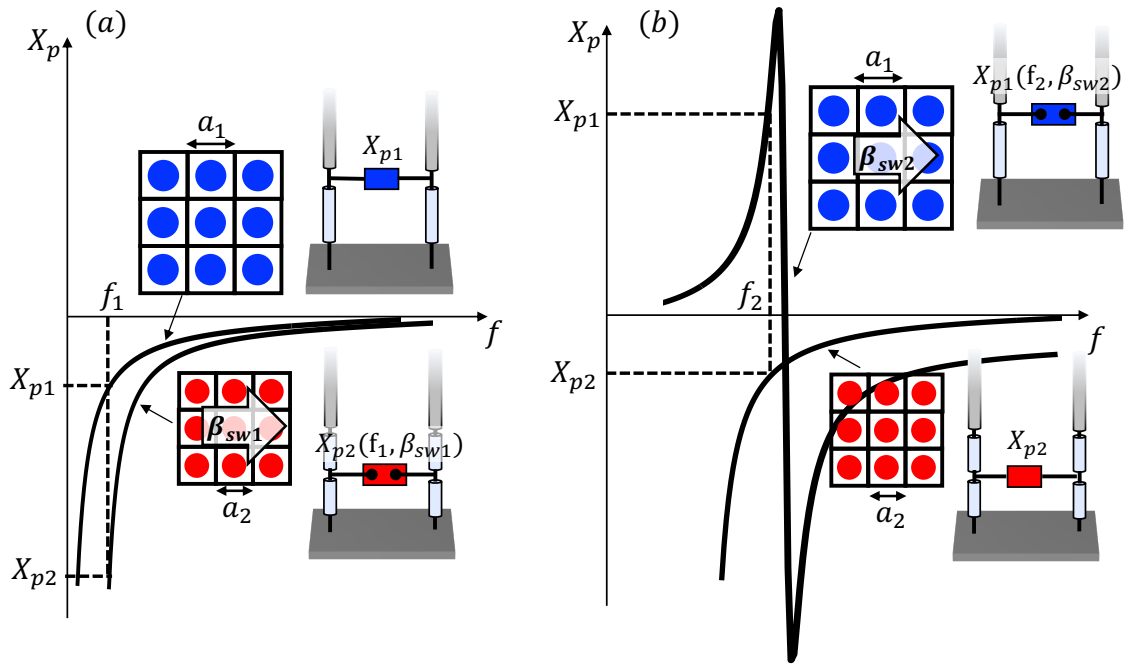

Figure 5.16: (a) Frequency dependence of the equivalent impedance resulting from the local periodic problem (top inset) of the patches working at f_1 (left curve). The right curve shows the equivalent impedance of the patches designed to work at f_2 (bottom inset) seen from the wave supported by the locally periodic structure in the top inset. (b) The same as in (a), but around f_2. The resonant curve represents the equivalent impedance of the patches designed to work at f_1 (bottom inset) seen from the wave supported by the locally periodic structure in the bottom inset.

Consequently, considering the middle layer as an open circuit simplifies the analysis to a grounded dielectric slab, conveniently modeled using a transmission line, as demonstrated previously. Similarly, the same principle applies when exciting the structure at frequency f_2. However, in this case, the top layer acts as an open circuit due to the high impedance experienced by the electromagnetic wave. By understanding the specific impedance characteristics at different frequencies, it becomes possible to analyze and model the antenna structure, considering the relevant layers as either open circuits or grounded dielectric slabs.

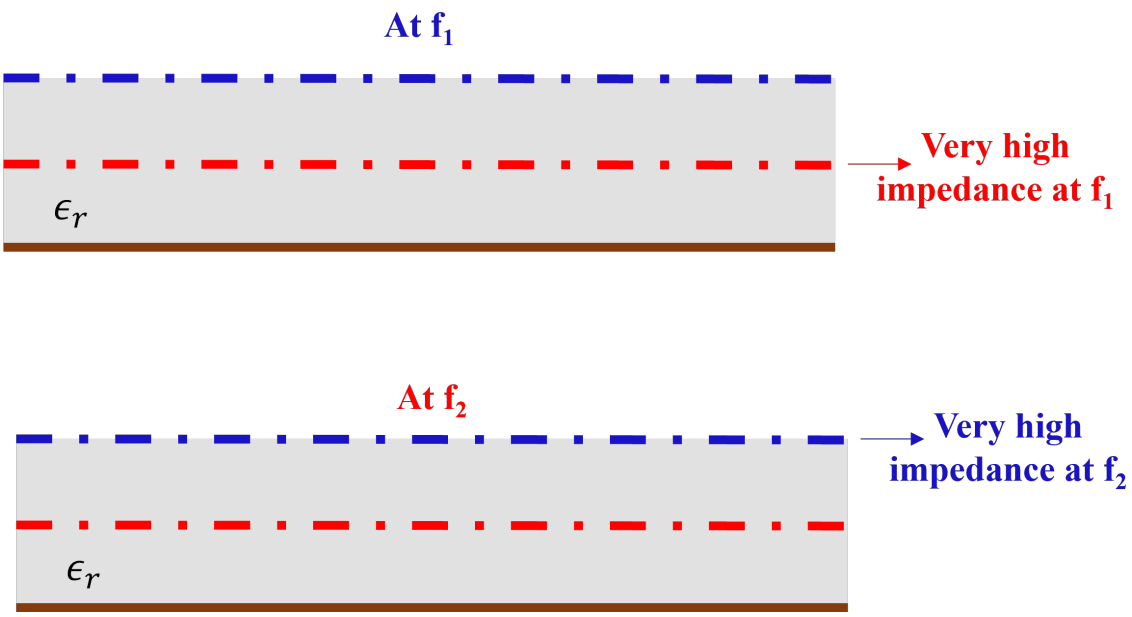

Figure 5.17: The two different possible operating scenarios for the antenna. The top figure shows how the impedance appears very high and consequently transparent when the antenna is excited at 35.75 GHz. The bottom figure shows that the top layer appears transparent from the high impedance when simulated at 94.05 GHz.

5.2.2 Realization of Antenna Through Double-Anchor Unit Cells

To demonstrate the accuracy of the proposed approach in the design of dual-band double-layered MTS antennas, two popular frequencies are chosen in climate science radars such as 35.75 GHz (f_1) and 94.05 GHz (f_2) [63]. The dielectric substrate used is Roger 4003C with an $\varepsilon_r = 3.55$ and thickness $h_1 = 406$um. The canonical problem at two frequencies [Figs. 5.15(a) and (b)] are studied with the approach proposed in [58]. For the canonical problem at f_2 [Fig. 5.15(b)], the Green's function in [58] is suitably changed to consider that the modulated reactance sheet sits inside the dielectric slab ($h_2 = h_1/2$) instead of on the top. Characterizing X_{s1} and X_{s2} with $M_1 = M_2 = 0.3$, $X_{01} = 150\Omega$, $X_{02} = 100\Omega$, $d_1 = 7.4$mm, and $d_2 = 2.15$mm, the canonical problem at f_1 and f_2 support a fundamental (0-indexed) TM FM with wavenumbers $k_{x1}^{(0)} = 778.7 - j0.08$[rad/m] and $k_{x2}^{(0)} = 2985.5 - j5.5$[rad/m], respectively. With $M_1 = M_2 = 0$ (unmodulated surface impedances), $k_{x1}^{(0)}$ and $k_{x2}^{(0)}$ reduces to $\beta_{sw1} = 777.8$[rad/m]

($\Delta\beta_1 = 0.9$) and $\beta_{sw2} = 2981.27$[rad/m] ($\Delta\beta_2 = 4.23$), respectively. With this setup, it is straightforward to verify through Eq. (5.4) that the (-1)-indexed FM at both frequencies resides inside the light cone generating a broadside beam ($\theta_1 = \theta_2 = 0$). X_{s1} and X_{s2} are synthesized with the square unit cells shown in the top-left and bottom-right insets, respectively, of Fig. 5.18. Both unit cells are based on the same metallic element topology consisting of double-anchor patch [69]. The patch sits at the air-dielectric interface and within the dielectric slab ($h_2 = h_1/2$) in the unit cell for f_1 and f_2, respectively. See the insets of Fig. 5.18. The two unit cells with side $a_1 = 1.29$mm and $a_2 = 0.43$mm are studied with the MoM in [70]. The database of the reactance (X_{p1} and X_{p2}) as a function of the patch size are shown in Fig. 5.18. By using the same MoM, X_{p2} was extracted by forcing in the periodic problem with the unit cell designed for f_2 (bottom-right inset of Fig. 5.18) a surface wave with frequency f_1 and propagation constant β_{sw1} [Fig. 5.19(a)]. With this setup, one can observe that such a unit cell operates in extremely small impedance regime (quasi-open circuit). The same process is repeated with the unit cell designed for f_1 (top-left inset of Fig. 5.18) imposing a surface wave with frequency f_2 and propagation constant β_{sw2}. The extracted X_{p1} is shown in Fig. 5.19(b). The range of L_1 is extended with respect to the one of Fig. 5.18 to show the presence of a pole. One can observe that the location of the pole is right before the range of operation assumed in the reactance database of Fig. 5.18. Thus, the patches designed for f_1 operate in extremely small impedance regime at f_2 (quasi-open circuit), as can be seen in the inset of Fig. 5.19(b). It is worth emphasizing that, although, in the design, under consideration the relation between the sides of the two unit cells ended up being $a_1 = 3a_2$, our approach, as discussed in the previous section, does not prevent using unit cells whose sides are not related by an integer number.

An initial small-scale design is created to assess the capabilities of the dual-layered antenna theory. This design focuses on a linear segment of the antenna, exemplified by

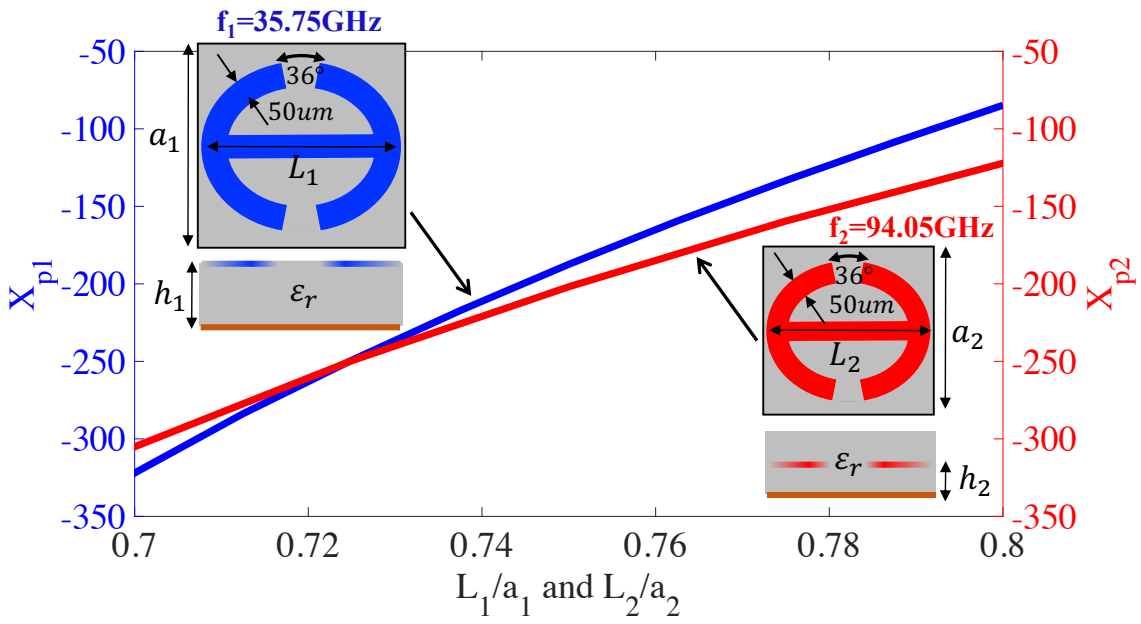

Figure 5.18: Equivalent surface reactance versus the patch size for the unit cell operating at 35.75 GHz (top-left inset) and 94.05 GHz (bottom-right inset). a_1 and a_2 are 1.29mm and 0.43mm, respectively.

the portion depicted in Fig. 5.20. Through varying the pointing angles of each layer, this setup effectively demonstrates the isolation achieved between the two layers.

To demonstrate the isolation and the influence of pointing angles on the antenna's performance, the top layer is designed to point at -20^o, while the middle layer is adjusted to showcase both broadside and non-broadside configurations. In Fig. 5.21a, the middle layer is designed for broadside. When this antenna is illuminated for 35.75 GHz, the antenna propagates at an angle of -20^o. As shown in Fig. 5.21a, the antenna is illuminated at 94.05 GHz and the radiation pattern shows that the antenna is pointing broadside. To ensure a consistent comparison, the impedance of the top layer remains the same, designed to radiate at -20^o. However, the impedance of the middle layer is modified to achieve a pointing angle of -20^o at 94.05 GHz. Subsequently, the antenna is illuminated at 94.05 GHz and the results for the directivity are shown in Fig. 5.21b. With the same directivity maximum and very similar radiation pattern as in Fig. 5.21a, these results show a clear shift of -20^o.

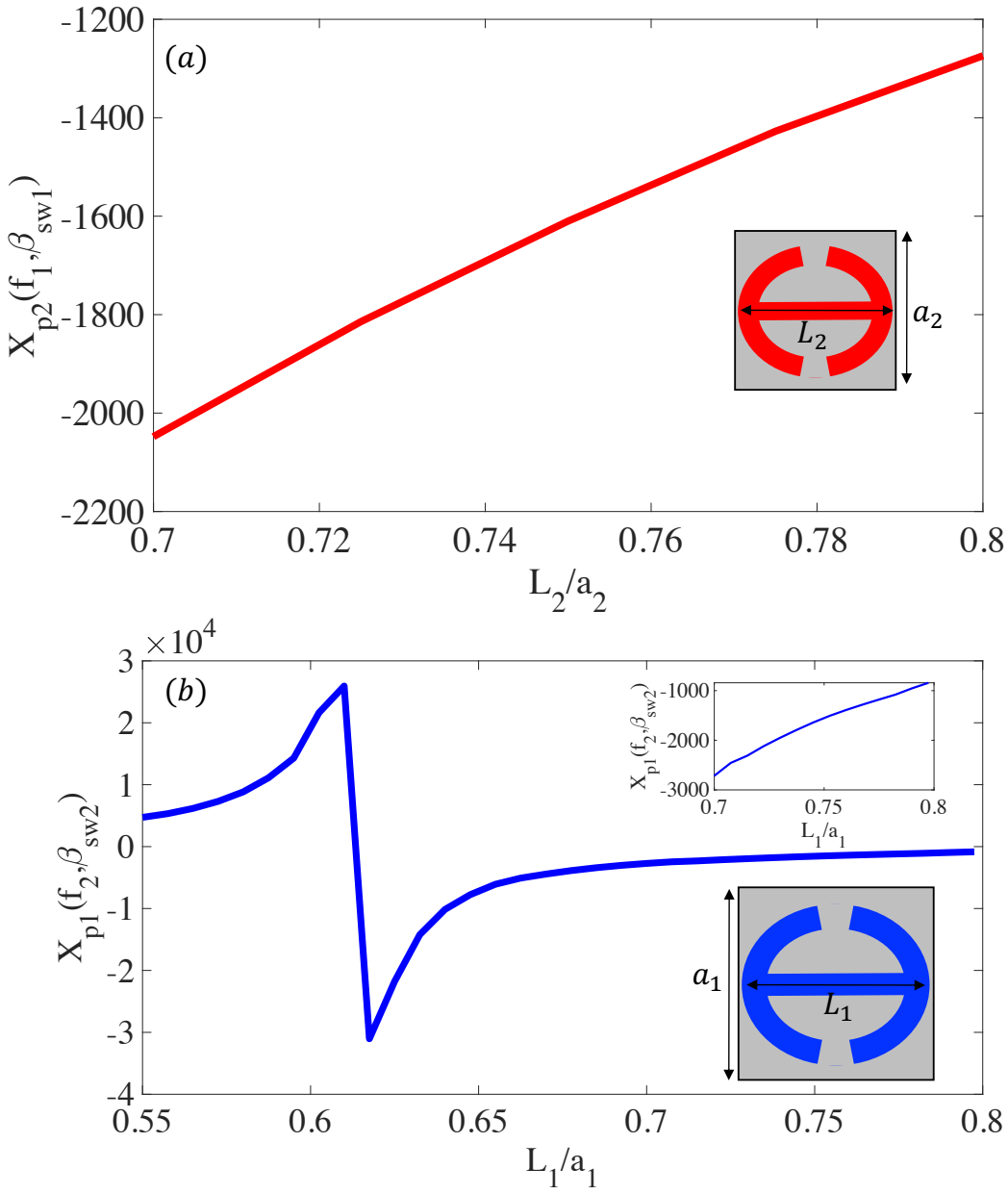

Figure 5.19: Driven equivalent surface reactance versus the patch size. (a) The surface reactance is extracted by forcing a TM surface wave with frequency 35.75 GHz and wavenumber $\beta_{sw1} = 777.8$[rad/m] in the local periodic problem with the unit cell operating at 94.05 GHz shown in the inset. (b) The same process as in (a) is repeated for the local periodic problem with the unit cell operating at 35.75 GHz shown in the bottom inset. The TM surface wave has the frequency 94.05 GHz and wavenumber $\beta_{sw2} = 2981.27$[rad/m]. The top inset shows a zoom-in of the equivalent surface reactance with size of the patch ranging as in Fig. 5.18.

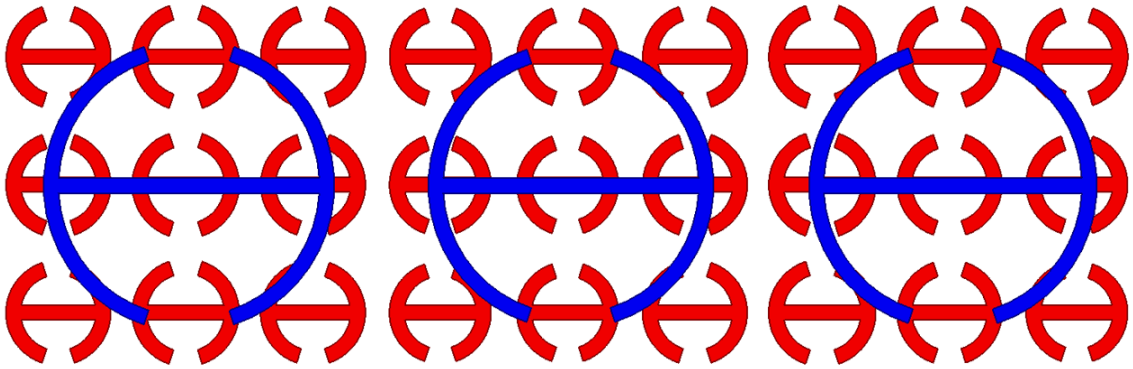

Figure 5.20: Initial linear design used for testing the concept of the dual layer and its ability to work at both broadside and non-broadside pointing angles

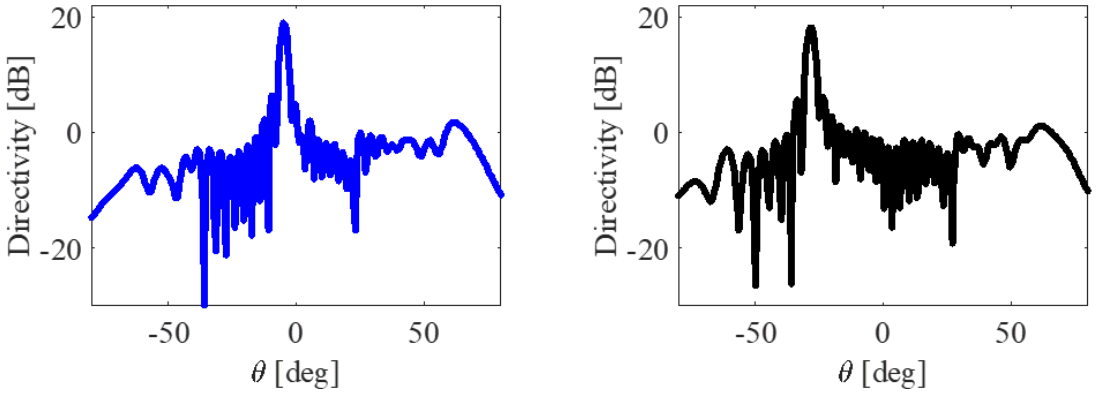

Figure 5.21: (a) Directivity of the linear antenna when the 35.75 GHz layer is designed for -20^o and the 94.05 GHz antenna is designed for 0^o. The results are for the antenna illuminated at 94.05 GHz. (b) Directivity of the linear antenna when the 35.75 GHz layer is designed for -20^o and the 94.05 GHz antenna is designed for -20^o. The results are for the antenna illuminated at 94.05 GHz.

The directivity plots serve to demonstrate two distinct aspects. Firstly, they illustrate the antenna's capability to function effectively at angles beyond the broadside. This indicates its suitability for applications requiring wide-angle coverage. Secondly, the plots reveal that the antenna's performance is only influenced by the frequency at which it is excited. Importantly, the two frequencies exhibit independence from each other, emphasizing the significance of frequency selection in achieving desired results. Based on these findings, the antenna design progresses towards the development of

the complete circular antenna.

By using the reactance databases of Fig. 5.18, a double-layered 3D MTS antenna radiating a right-handed circular polarized (RHCP) wave at both frequencies is designed. Due to the nature of the MTS where the metallic patches are modulated in two directions patterning the following modulated reactance sheets: $X_{s1,2}^{2D}(\rho,\phi) = X_{01,2}\left(1 + M_{1,2}\cos\left(\frac{2\pi}{d_{1,2}}\rho - \phi\right)\right)$ with ρ and ϕ representing the position in polar coordinates, the MTS is considered to be 3D. The ϕ-dependence in $X_{s1,2}^{2D}$ ensures that any two sectors on the antennas separated by 90° radiates an electric field with orthogonal and quadrature-phased components resulting in a circularly polarized wave. Note that the design of 3D MTS antennas is usually based on the 2D canonical problem of Fig. 5.1. Each sector can be seen as a 2D canonical problem rotated by an angle ϕ around the z-axis. Hence, the approach proposed in this dissertation can be applied to designing both 2D and 3D dual-band double-layered MTS antennas. For ease of visualization, Fig. 5.22 displays only a portion of the antenna layout. The sizes of the two MTSs are equal, although the approach proposed in this dissertation does not prevent MTSs with different sizes. The antenna radius is 3λ and 5λ at the operating frequency f_1 and f_2, respectively. A smaller radius is selected at the lower frequency because, at this frequency, the size of the MTS designed for f_2 is electrically large, and very computational intensive and difficult to simulate with the available resources. The antenna is fed by an electrically small dipole exciting a cylindrical TM mode. The dipole is displaced by h_2 upward relative to the center of the ground place. The antenna is simulated with the commercial software Ansys HFSS. Figs. 5.23(a) and (b) show the obtained co-pol directivity patterns at f_1 and f_2, respectively, for the single- and double-layered MTSs. At both frequencies, a notable correspondence can be observed between the patterns generated by the single-layered and double-layered MTSs, indicating a satisfactory agreement.

In conclusion, this chapter has focused on designing a single-layered MTS antenna

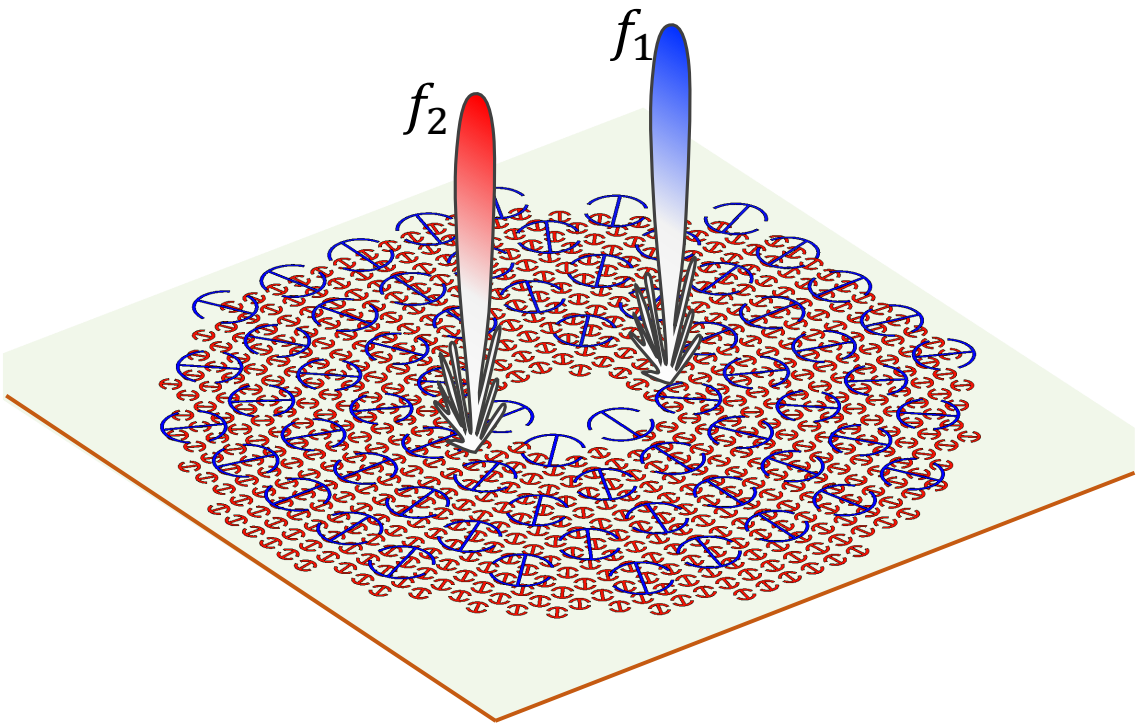

Figure 5.22: A portion of the layout of the designed double-layered metasurface antenna operating at 35.75 GHz and 94.05 GHz. The structure consists of two metallic claddings (blue and red patches) supported by a grounded dielectric slab. The top and bottom claddings (blue and red patches) control the radiation at 35.75 GHz and 94.05 GHz, respectively. The bluish and reddish beams conceptually sketch radiation patterns at f_1 and f_2, respectively.

for operation at 94.05 GHz to find the limitations on simulation and realizability. It demonstrates the creation of a specialized impedance profile using a tensor-based to accomodate the complex design of the antenna. The process of designing the antenna involves generating a 3D database by systematically varying unit cell dimensions and rotations, essential for handling spatial dispersion and lattice dependency. The resulting antenna exhibits impressive directivity and minimal side lobes.

Furthermore, this chapter introduces a groundbreaking approach for designing dual-band double-layered MTS antenna. The proposed antenna structure comprises two MTS layers, each tasked with controlling radiation at specific frequencies. These layers are combined to achieve dual-frequency operation. The key concept lies in leveraging Foster's Reactance theorem, which governs the behavior of reactance sheets in

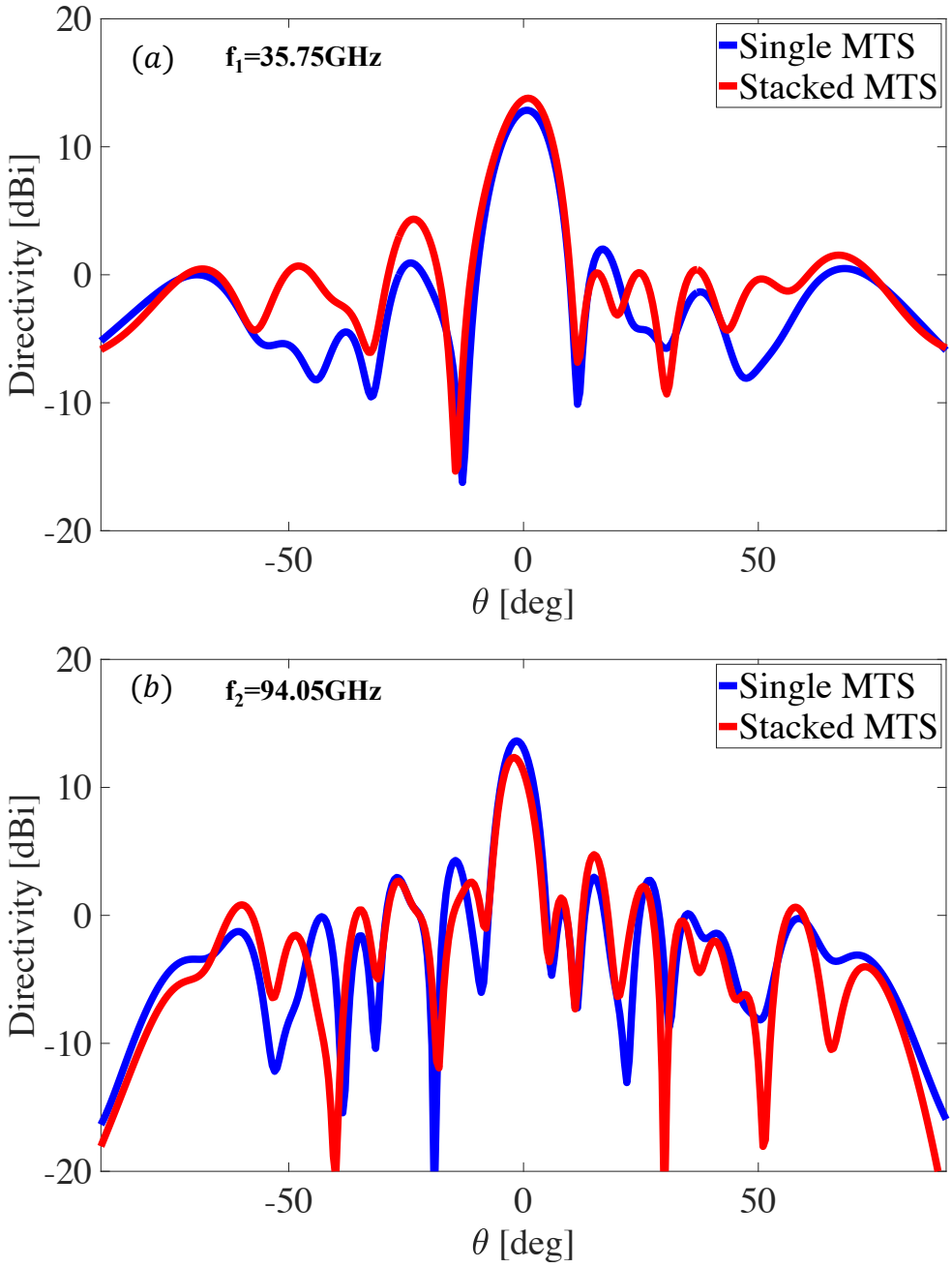

Figure 5.23: Right-handed circularly polarized directivity patterns for the single- and double-layered MTS antenna of Fig. 5.22 at (a) 35.75 GHz and (b) 94.05 GHz.

MTS designs. By ensuring that the equivalent reactance of one MTS layer aligns with a pole at the other frequency, this approach enables the independent design of the two layers. The practical implementation of this method is exemplified through dual-band operation at 35.75 GHz and 94.05 GHz, resulting in circularly polarized

radiation patterns that closely match single-layered MTS designs at both frequencies.

Looking ahead, the future research directions for this antenna involve further improving the efficiency of its individual layers, incorporating anisotropic impedance, and integrating tapered modulation techniques. As the optimization process in the design phase continues to advance, the next steps will involve fabricating the antenna and subjecting it to comprehensive testing. Upon successfully completing these design and testing phases, the antenna will be ready for integration into space-based technology, with a specific focus on applications in weather research and analysis.

CHAPTER 6: DESIGN OF ADDITIVE MANUFACTURABLE METASURFACE ANTENNA

MTS technology has found applications in designing leaky-wave (LW) antennas that enable control over the radiative properties of electromagnetic waves [71, 72, 73, 74]. It achieves this by manipulating either the radiative surface waves [75, 76, 77] or the surface waves themselves. This control is usually achieved through the discretization of the designed surface impedance via unit cells, allowing for precise tailoring of the antenna's performance and radiation characteristics.

One of the ways to accomplish the discretization of impedance for symmetrical shapes is the method of moments; this symmetry makes the antenna isotropic limiting its applications [78, 79]. In contrast, metasurfaces offer the flexibility to design antennas with asymmetrical patches or shapes, enabling the creation of anisotropic antennas for tasks such as polarization control [65]. These effects can also be achieved using electromagnetic structures composed solely of dielectric materials, offering advantages such as reduced weight, particularly valuable in applications like satellites and wireless communication [80, 81, 82]. One specific type of metasurface, known as air-perforated dielectrics, finds applications across a wide range of fields, including physics, material science, civil engineering, and electrical engineering [83]. These air-perforated dielectrics can also be used in the design of leaky-wave antennas [84]. Similar to patch-based metasurfaces, the initial step often involves finding the homogeneous equivalent of the dielectric slab through effective permittivity. This approach has been extended to anisotropic metasurfaces, employing various methods, including mathematical techniques and full-wave simulations, to characterize their dispersive behavior [83].

The unit cell analyzed in this dissertation is a dielectric, cylindrical pin. This approach involves modeling the unit cell as a uniaxial, dielectric slab. The grounded slab can be effectively represented using a transmission line model, and its dispersion characteristics can be derived using fundamental equations. A full-wave approach is also introduced to study the method comprehensively, covering a range of radial sizes for the pin. Furthermore, this novel approach is applied to the design and simulation of a leaky-wave antenna. This antenna is constructed using additive manufacturable materials and is intended to operate efficiently at various pointing angles.

6.1 Dispersion Study of Dielectric Cylindrical Pin

This section presents a numerical approach to analyze the dielectric pin unit cell's dispersion characteristics. To simplify the complex geometry of the unit cell, it is treated as a uniaxial slab with an effective permittivity. Classical Maxwell-Garnett mixing equations are employed to determine the effective relative permittivity for different modes. The dispersion behavior is derived through a transmission line model, offering valuable insights into how the dielectric pin unit cell behaves within metasurfaces and antennas.

6.1.1 Numerical Approach Through Classical Mixing Equations

In order to analyze the unit cell, the reference plane can be considered as the (x, y, z) coordinate system, with the optical axis along the z direction. Assuming local periodicity in the x and y directions, the unit cells sinusoidally varying can be represented as shown in Fig.6.1 where the sinusoidal modulation is featured by the dashed red and blue lines. Each dielectric pin, highlighted in Fig. 6.2a, resides within a unit cell characterized by parameters such as period a, height h, and radius r. However, analytical investigation becomes challenging with this representation, prompting the need for a different modeling approach to facilitate a more straightforward analysis. Alternatively, Fig.6.2a can be viewed using the local periodicity

assumption where the highlighted pin is repeating in both the x and y directions so it is studied as visually described in Fig. 6.2b. In order to numerically solve for the dispersion characteristics of the unit cell, the repeating pins of the same height can be modeled as a uniaxial slab with the same height, as illustrated in Fig. 6.3. In this approach, the slab is assigned an effective permittivity denoted as $\underline{\underline{\epsilon}}$, which considers its anisotropic properties.

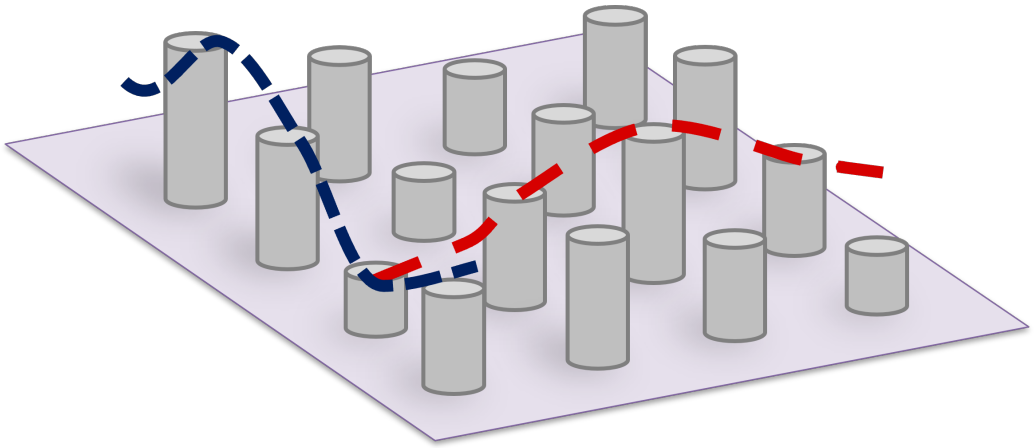

Figure 6.1: Sample of the metasurface antenna with unit cells sinusoidally modulated in all directions with the dashed lines highlighting the sinusoidal modulations.

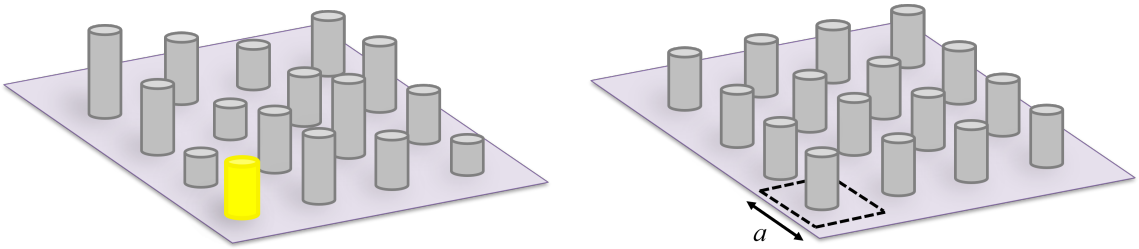

(a) (b)

Figure 6.2: (a) Left: Isotropic, cylindrical pin unit cell on a ground plane with an effective permittivity, ϵ_r, period, a, height, h, and radius r. Right: Equivalent uniaxial, grounded dielectric slab of the left figure with the same h and a tensorial permittivity ϵ_{eff} described by its effective parallel and perpendicular permittivity.

The effective relative permittivity for each mode is determined using classical Maxwell-Garnett mixing equations, originally developed for homogeneous elliptical

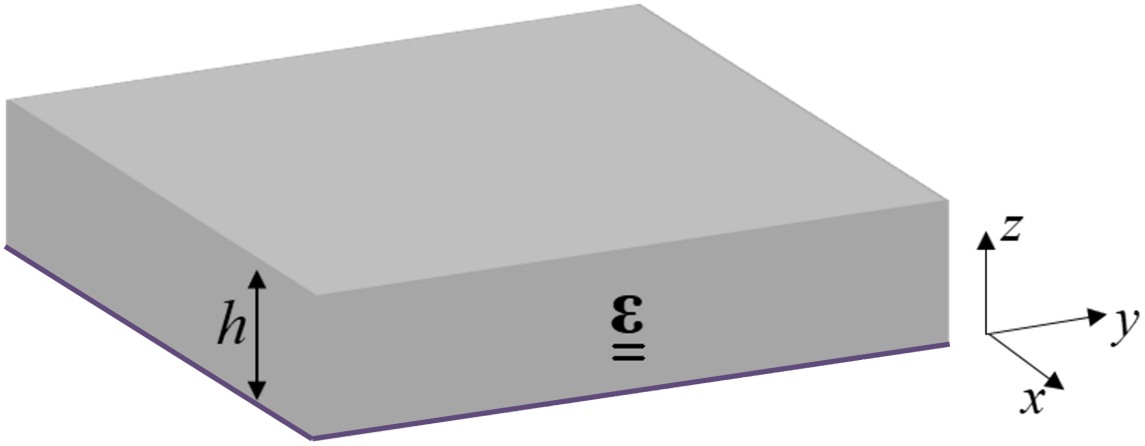

Figure 6.3: Dielectric slab used to model the cylindrical pin unit cell using a tensor to describe the relative permittivity allowing the unit cells to be modeled as a uniaxial slab.

scatterers, as described in [83]. These equations are extended to analyze the behavior of the uniaxial slab representing the pins in this context. The total effective permittivity of the dielectric slab model is defined as $\underline{\underline{\epsilon}} = \epsilon_0 \underline{\underline{\epsilon}} r$, where ϵ_0 is the free space permittivity, and $\underline{\underline{\epsilon}} r$ is a tensor represented as:

$$\underline{\underline{\epsilon}}_r = \begin{bmatrix} \epsilon_\perp & 0 & 0 \\ 0 & \epsilon_\perp & 0 \\ 0 & 0 & \epsilon_{||} \end{bmatrix} \tag{6.1}$$

Here, $\epsilon_\perp$ represents the permittivity for TE polarization, while $\epsilon_{||}$ represents the permittivity for TM polarization. The values of $\epsilon_\perp$ and $\epsilon_{||}$ depend on the material's permittivity and the fill factor. The fill factor is a measure of the ratio of the volume occupied by the dielectric pin to the volume of an airbox with the same height and period as the pin.

After substituting in the depolarization factor [85] for the transverse axis, the permittivity for the ordinary wave is:

$$\epsilon_{\perp} = \epsilon_0 \left[1 + 2fill \times \frac{\epsilon_m - \epsilon_0}{\epsilon_m + \epsilon_0 - f(\epsilon_m - \epsilon_0)} \right] \tag{6.2}$$

where ϵ_m is the dielectric matrix and ϵ_0 is the free space permittivity. The dielectric matrix accounts for the isotropic behavior of the dielectric and can be described as $\epsilon_m = \epsilon_{rm}\epsilon_0$ where ϵ_{rm} is the relative permittivity of the dielectric.

The extraordinary wave is defined by the behavior of the depolarization considering the longitudinal axis. For this structure, there are no dielectric pins along the longitudinal axis so the depolarization factor is 0. This reduces the classical mixing equation for the extraordinary mode to Eq. 6.3.

$$\epsilon_{||} = fill \times \epsilon_m + (1 - fill)\epsilon_0 \tag{6.3}$$

The resulting behavior from Eq. 6.2 and Eq. 6.3 can be portrayed graphically in its relationship to the fill factor of the unit cell in Fig. 6.4 ranging from a fill of 0% to a fill of 100%. Notice how with zero fill, the dielectric slab behaves just as air and a 100% fill is representative of an isotropic dielectric slab. Due to the nature of the geometry, the maximum fill is determined via the instance of the radius equalling half of the size of the period. Because of this, the porosity of this geometry is maximum at 78.54%, but there is no lower limit to the accuracy of this analytical approach.

The dispersion characteristics can be derived via a transmission line model illustrated in Fig. 6.5 [86]. The tensorial permittivity is contained in the grounded dielectric with impedance Z_{in}. Since the grounded slab is contained in air, the latter half of the transmission line is composed of an open circuit of free space impedance, Z_0.

Looking into the input impedance, the transmission line is shorted by the grounded slab. This simplifies the equation to describe the impedance as $Z_{in} = jZ_c \tan(\beta h)$ where h is the height of the dielectric slab, Z_c is the characteristic impedance of the the dielectric slab, and β is the propagation constant. The characteristic impedance

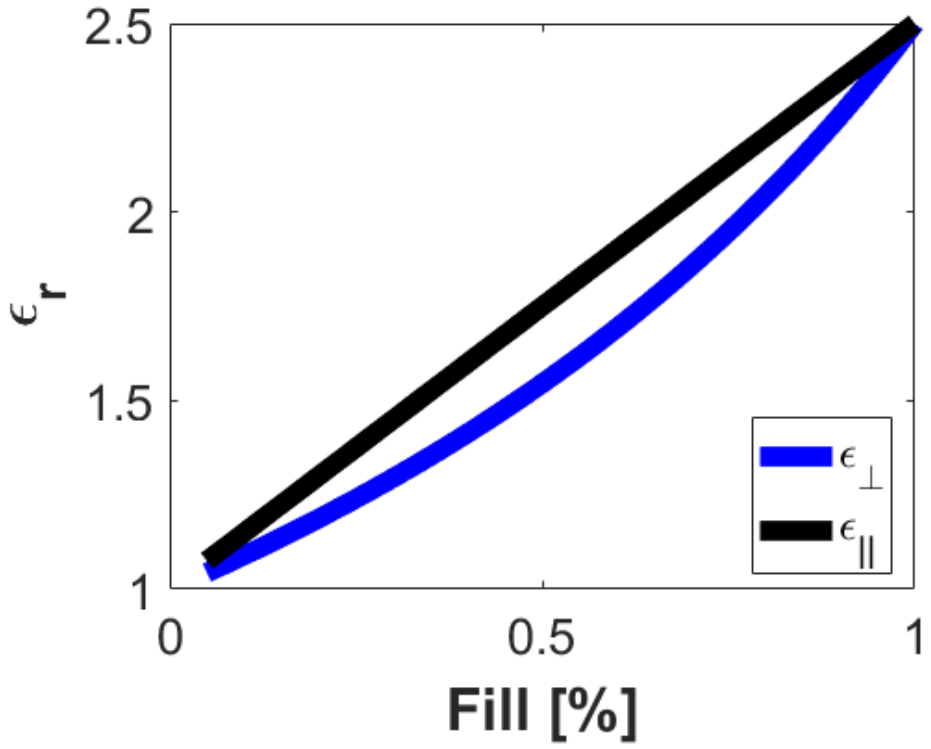

Figure 6.4: Relationship of the the $\epsilon_\perp$ and $\epsilon_{||}$ in respect to the percentage of the fill. These ϵ values are used to compose the diagonal of the tensor representation of the total effective permittivity of the slab.

and propagation constant are defined as $Z_c = \frac{k_z}{\omega\epsilon}\sqrt{\frac{\epsilon_\perp}{\epsilon_{||}}}$and $\beta = \sqrt{\frac{\epsilon_\perp}{\epsilon_{||}}}k_z$ respectively.

The z component of the wave vector, k_z, is described in Eq. 6.4 where ω is the radial frequency and k_ρ is the summation of the squares of the x and y component of the wave vector shown in Eq. 6.5. Since the optical axis of this antenna is defined to be z, k_ρ is also considered to be the plane on the surface of the antenna acting as a surface wave.

$$k_z = \sqrt{\omega^2\mu_0\epsilon_{||} - k_\rho^2} \tag{6.4}$$

$$k_\rho = k_x^2 + k_y^2 \tag{6.5}$$

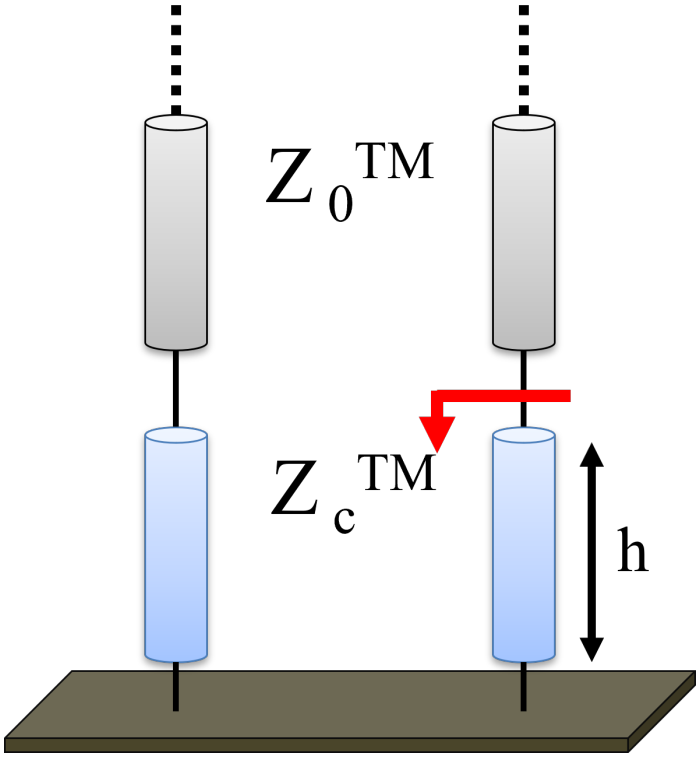

Figure 6.5: Local transmission line model of the grounded uniaxial slab in the Fig. 6.3 where Z_{slab} is he impedance of the uniaxial slab with height, h, and Z_0 is the impedance of free space.

With the individual components of the wave number defined, the wave number can be expressed in two different ways: $k = k_\rho^2 + k_z^2 = \omega\sqrt{u_0\epsilon_{||}}$. Similarly, the characteristic impedance and wave number can be expressed for the wave propagating in air where $Z_{in0} = Z_{c0}$.

$$Z_{c0} = \frac{k_{z0}}{\omega\epsilon_0} \tag{6.6}$$

$$k_{z0} = \sqrt{\omega^2\mu_0\epsilon_0 - k_\rho^2} \tag{6.7}$$

The dispersion of the dielectric slab is found by finding k_ρ through satisfying the transverse resonance such that $Z_{in0} + Z_{in} = 0$. Through applying the above equations, the dispersion equation thus becomes:

$$Z_{c0} + jZ_c \tan(\beta h) = 0 \tag{6.8}$$

By solving for the surface wave number, k_ρ, in Eq. 6.8 using the tensorial permittivity and corresponding fill of the unit cell, the dispersive behavior is found for a unit cell with a cylindrical pin with a certain fill modeled as the anisotropic grounded slab.

6.1.2 Full-Wave Analysis Comparison to Numerical Approach

The second approach presented involves using the traditional method to determine the dispersive behavior. This approach relies on a full-wave simulation of a unit cell and is used to assess the accuracy of the numerical method discussed earlier. In this method, a unit cell is created in HFSS by placing an isotropic dielectric pin with radius, r, and height, h, in a grounded air box, with period a. The unit cell structure is analyzed with local periodicity such that it is infinitely periodically expanding in both the x and y direction using periodic boundary conditions (BCs). Using eigenmode analysis, the phase is swept gradually from 0^o to 180^o for one set of BCs while maintaining no phase shift for the orthogonal set of BCs. This iterative procedure is focused on determining the dispersion characteristics for a specific height and necessitates replication across a spectrum of heights to construct a comprehensive database, a task demanding significant time investments. In practice, acquiring dispersion data for a wide range of heights can be time-consuming, with each design iteration taking multiple hours. This challenge becomes more pronounced when investigating diverse unit cells for various applications or frequencies, amplifying the cumulative time investment.

The numerical method introduced in this context significantly accelerates the process of characterizing the dispersive behavior for a specific height. The method is so efficient that it takes less than a second to obtain the relevant data for a singu-

lar height. Furthermore, the creation of a comprehensive database encompassing a range of heights for each unit cell is achieved in a remarkably short period, typically requiring less than a minute. This efficiency stands in stark contrast to traditional approaches that demand substantial time investments in setting up and waiting for simulations to complete. The advantages of this expedited method become evident when comparing its performance to the conventional approach across various fill levels, or porosity values, as illustrated in Figure 6.6. To maintain consistency, a uniform height of 10 mm is employed for all three unit cells under examination, although this height selection is arbitrary, and various values within the operational range could have been chosen. Similarly, the unit cell period remains constant across all three curves, with the unit cell designed for 15 GHz and featuring 6 cells per modulation period. Since this approach relies on the fill ratio, its applicability extends across a wide frequency range. Figure 6.6 showcases three distinct examples, each associated with a unit cell having a radius of 0.25 mm, 1.6 mm, and the maximum fill achieved when the radius is equal to half the size of the period. Correspondingly, these values yield porosities of 0.92%, 37.65%, and 78.54%, as indicated by the solid lines. The full-wave simulation results for each porosity are superimposed on the analytical method presented, depicted as dotted lines, to highlight the accuracy of the method. Notably, both approaches demonstrate a high degree of agreement with each other.

6.2 Implementation of Numerical Method for Antenna Design

From solving the transverse resonance, the value of k_ρ is found which is used to find the dispersion behavior. The surface wave on the xy plane can be described as its real and imaginary components of $\alpha_{sw} + j\beta_{sw}$ or the attenuation constant plus the phase constant respectively. Since k_ρ is purely imaginary, it can be simplified to only be described by β_{sw} for a modulated surface. According to [1], the phase constant on a modulated surface is defined in Eq. 6.9

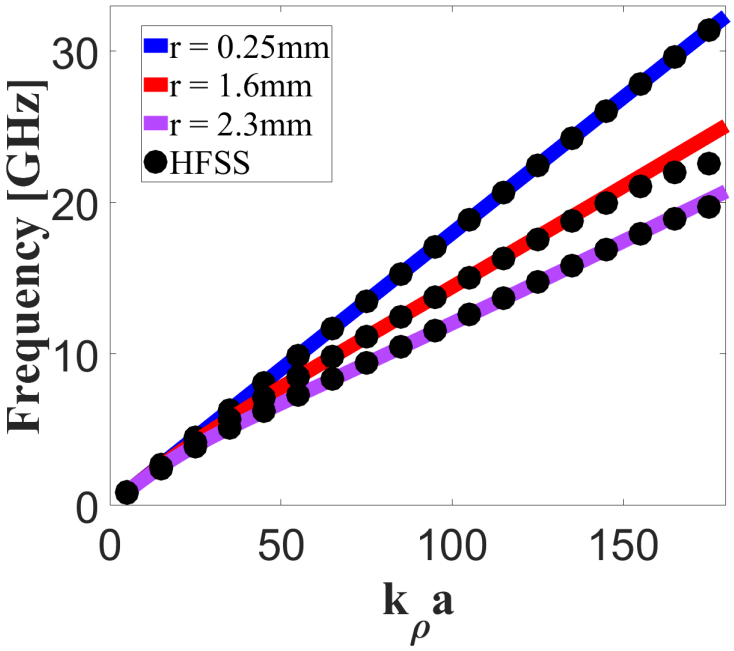

Figure 6.6: Dispersion curves for three different radius values (0.25 mm, 1.6 mm, 2.3 mm) that range from very small to the largest possible radius size for a unit cell size of 4.6 mm. All of the unit cells were ran at the arbitrary height of 10 mm. The solid, colorful lines are the results from using numerical method. The black dots describe their respective results when the dispersion information is found using HFSS.

$$\beta_{sw} = k\sqrt{1 + \left(\overline{X}/\zeta\right)^2} \tag{6.9}$$

where $\overline{X}$ is the average reactance of the modulated metasurface. Oliner and Hessel [5] describe the relationship of a guided plane wave along a modulating structure to have a surface impedance of $X_s(x) = \overline{X}[1 + M\cos(2\pi x/d)]$, along the xy plane for a broadside pointing angle with M describing the modulation index. Utilizing Oliner and Hessel's equation for a broadside pointing angle, Minatti et al. extended it from the linear Cartesian case to a cylindrical coordinate system, thereby accommodating non-zero pointing angles due to the dependence on ρ and ϕ. Equation 6.10 illustrates the sinusoidal modulation of the surface reactance for any angle, with θ_0 representing

the pointing angle, while ρ and ϕ denote the positions of the cylindrical pins on the surface.

$$X_s(\rho, \phi) = \overline{X}(1 + M \sin(\beta_{sw}\rho - k_0\rho \sin\theta_0 \cos\phi \pm \Phi)) \tag{6.10}$$

The equation above considers a few design parameters that are chosen to control the average impedance, rate of attenuation, and the size of the antenna. The average impedance is chosen to be $\overline{X} = 0.7\eta_o$, the modulation index is set to $m = 0.65$, and the radius of the antenna is 10 times the modulation period. In addition, the size of the cylinder radius is chosen to be the unit cell size divided by 2.1.

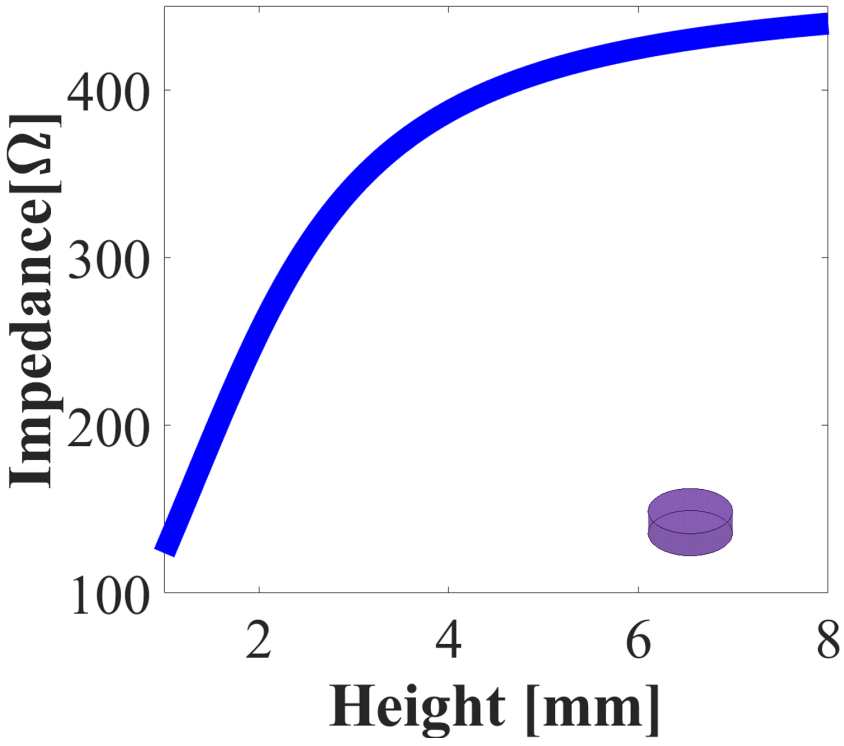

Figure 6.7: Relationship describing the height of the cylindrical pin to the impedance to serve as a database for the surface impedance of the antenna

6.2.1 Design of a Broadside Radiating Antenna

Equation 6.10 provides the full impedance profile for an antenna designed to operate at 25 GHz, chosen based on the size restraints of a 3D printer, given in Fig. 6.14a in respect to the placement of each unit cell position in order to achieve the appropriate pointing angle. The height of each pin corresponds to a specific impedance and is carefully tailored to match the impedance profile, forming the foundation of the antenna design. As depicted in Fig.6.14b, the range of heights for the dielectric cylinders spans from very small values to approximately 12 mm, ensuring the necessary impedance variation is achieved. To assess the design's accuracy, validation is conducted by examining the error, as presented in Fig. 6.14c. This figure demonstrates the minimal discrepancy between the ideal impedance value and the impedance provided by the various cylinders, affirming the design's efficacy.

In light of the extremely small error, the subsequent phase of this antenna design entails simulating the designed antenna using HFSS. Within the HFSS simulation, the antenna is excited with a coaxial-type excitation, customized to match with the surface impedance. This excitation is accomplished by extending the inner PEC a few millimeters into the antenna. The additional length of the inner PEC aids in exciting a wave that couples effectively with the pins, facilitating the propagation of the surface wave. The antenna's configuration with the coaxial excitation is visually represented in Fig. 6.9.

The results of the directivity for the left hand circular polarized (LHCP) wave is provided in Fig. 6.10. The directivity shows main beam pointing broadside with a maximum value around 25 dB. In addition, the side lobes for this antenna are sufficiently low.

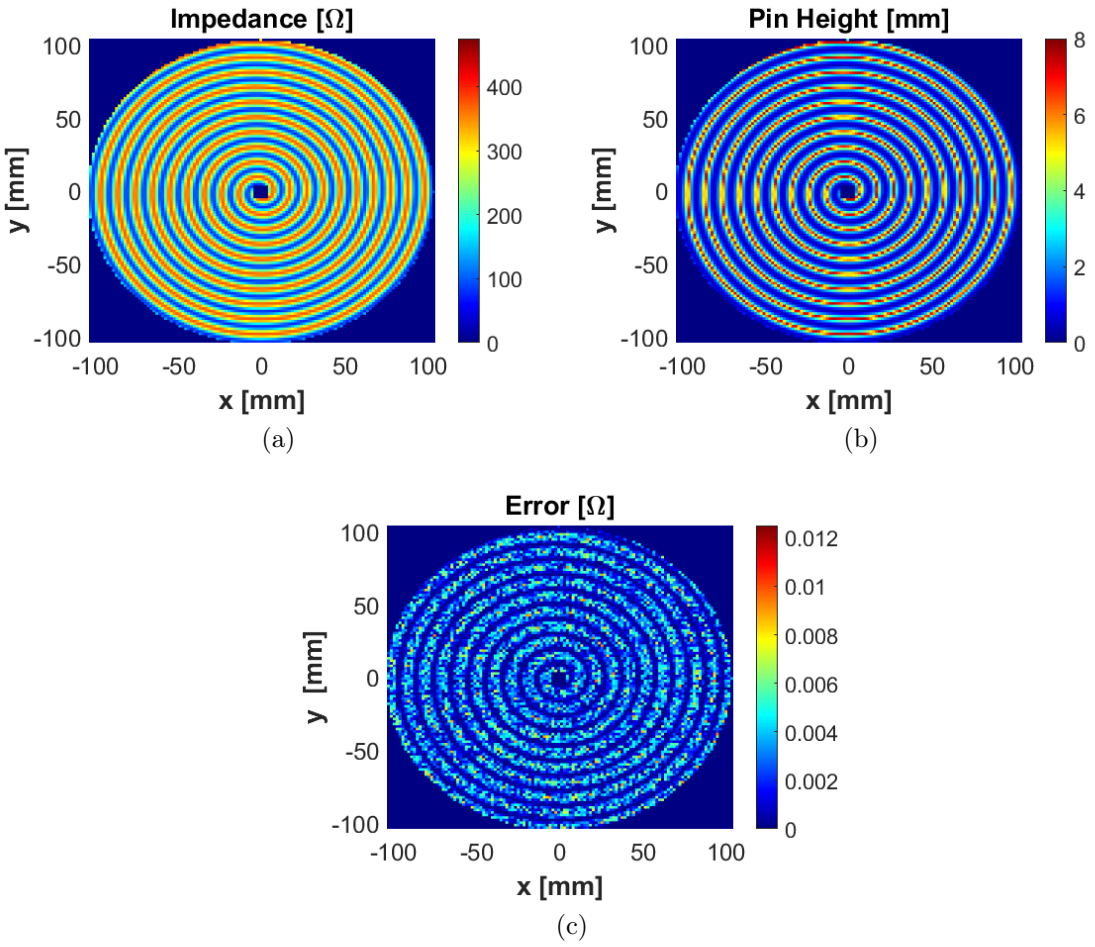

Figure 6.8: (a) Impedance profile for an antenna with a radius of 10 modulation periods designed for 25 GHz for broadside propagation (b) The heights of the cylindrical dielectric pins corresponding to the impedance profile (c) The error is the difference between the values used via the dielectric pins and the ideal impedance values.

6.2.2 Design of Non-Broadside Radiating Antennas

Furthermore, this method extends its applicability beyond broadside designs and proves effective in creating antennas with pointing angles significantly deviating from broadside. To illustrate the method's versatility, all parameters of the previous antenna are maintained, except for the pointing angle, which is adjusted to 15^o. Consequently, this new angle results in an impedance profile, along with its corresponding cylinder heights and error, as displayed in Fig. 6.11. It is worth noting that the impedance shape exhibits more pronounced spatial spirals on one side, while the

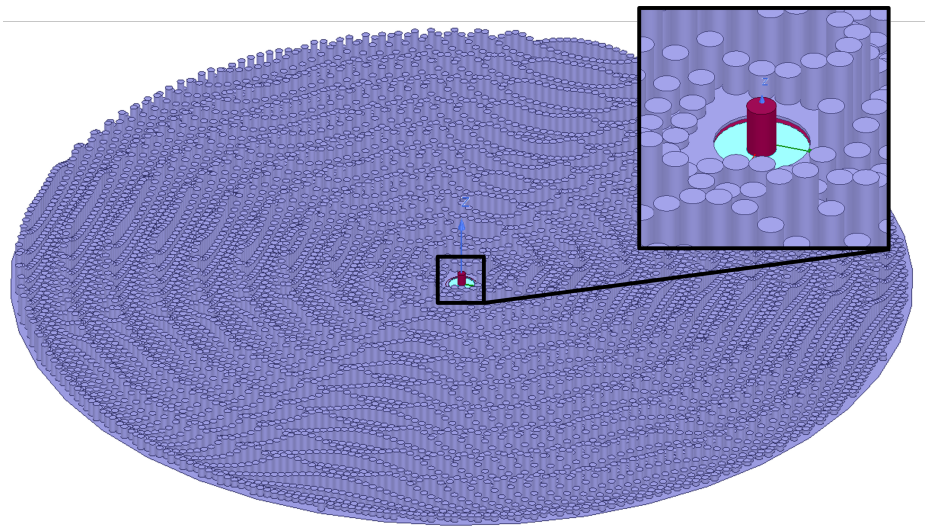

Figure 6.9: Screenshot of the antenna in Ansys HFSS with a radius of 10 modulation periods designed for 25 GHz and broadside propagation excited with a coaxial cable

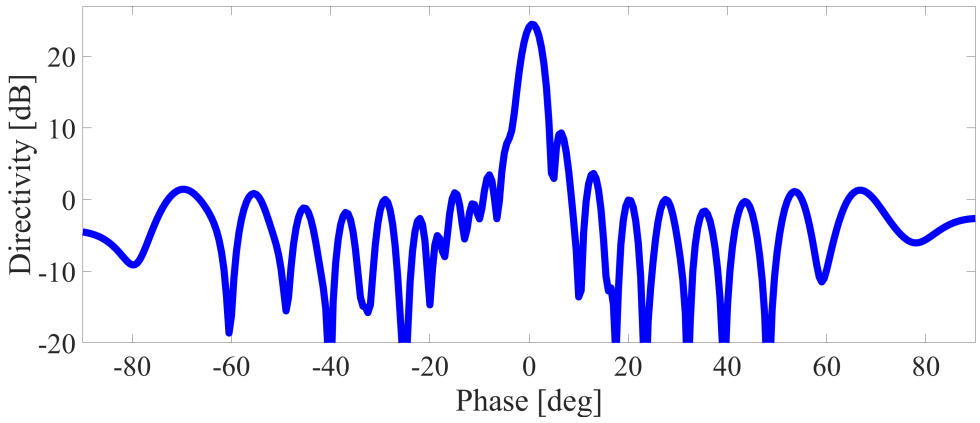

Figure 6.10: Directivity of a circularly polarized wave for the full dielectric antenna with a modulation index of 0.65, an average impedance of 0.6η, and a radius of 10 modulation periods designed to radiate broadside.

other half of the antenna displays a closer spiraling pattern. This asymmetric sizing is a direct consequence of the non-broadside pointing angle, effectively steering the wave to the desired direction.

Using the same coaxial excitation method as employed for the previous antenna, simulations of this design produce the LHCP, depicted in Fig. 6.12. The plot clearly illustrates a well-defined main lobe direction with an equivalent level of directivity,

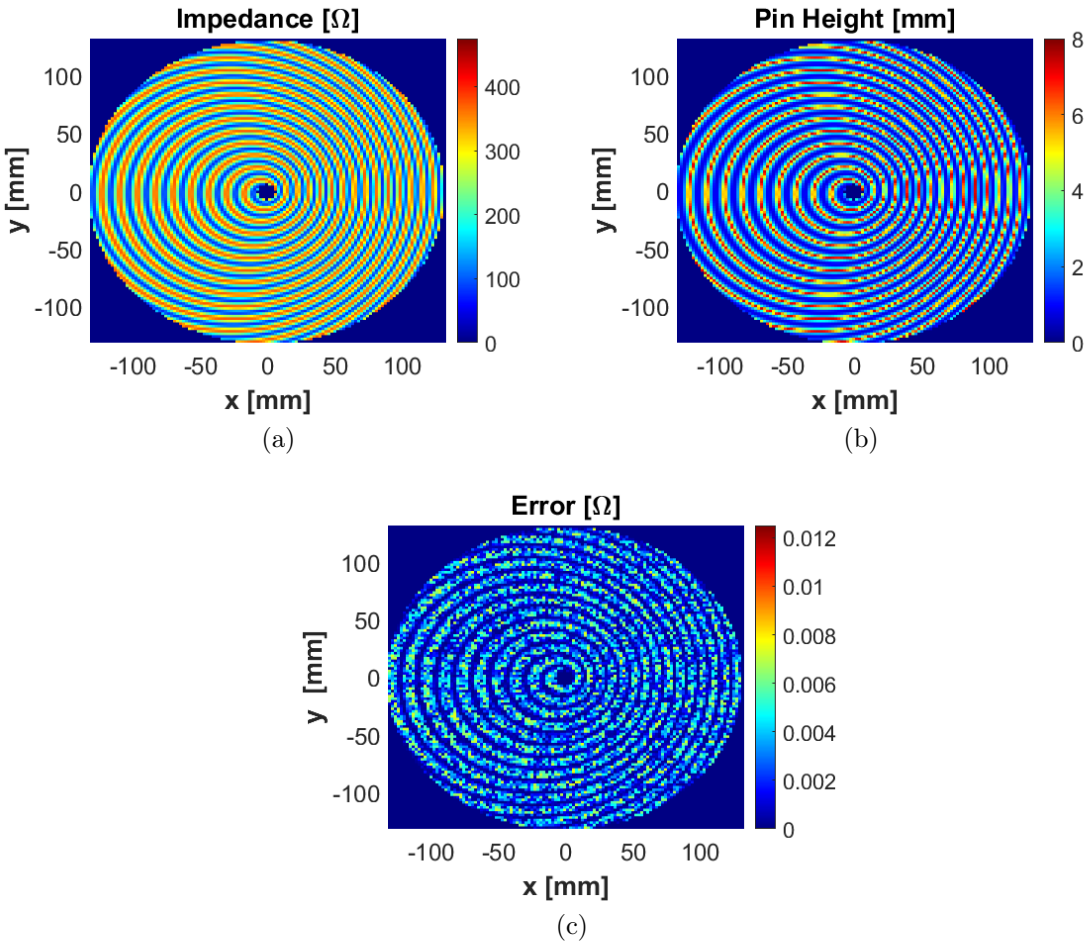

Figure 6.11: (a) Impedance profile for an antenna with a radius of 10 modulation periods designed for 25 GHz for broadside propagation (b) The heights of the cylindrical dielectric pins corresponding to the impedance profile (c) The error is the difference between the values used via the dielectric pins and the ideal impedance values

maintaining the same performance as when originally designed for broadside propagation.

6.3 Fabrication and Testing

The antennas are simulated using a relative permittivity (ϵ_r) of 2.5 and a dielectric loss tangent (δ) of 0.018, as reported in Boussatour et al. [87], to emulate the empirically tested values of polylactic acid (PLA). The chosen material properties accurately represent the electromagnetic behavior of PLA in the simulations. The antennas are printed using the Raise3D Pro printer and PLA material. To optimize

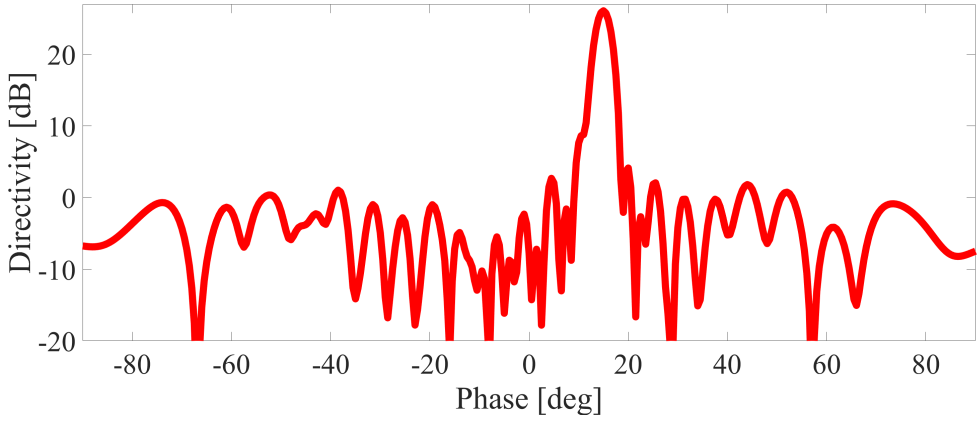

Figure 6.12: Directivity of a circularly polarized wave for the full dielectric antenna with a modulation index of 0.65, an average impedance of $0.6eta$, and a radius of 10 modulation periods designed to radiate at 15^o.

printing accuracy, careful considerations were made. The radius of the pins, which serve as the aperture elements, was selected based on the printer's nozzle size. The printer's nozzle has a diameter of 0.4 mm, and the pin radii were chosen as multiples of this value to ensure precise printing and alignment between the pins and the nozzle, resulting in improved printing resolution and accuracy. Various printing parameters, including speed, layer height, and temperatures, were adjusted to achieve smoothness and accuracy in the printed antennas. These parameter adjustments helped enhance the overall quality of the printed structures, including the aperture elements. To avoid the need for additional supports during printing, such as a raft or extra structural supports, a 0.2 mm thick layer was added to the bottom of the antenna. This additional layer provided sufficient support for the pins and facilitated the removal of the antenna from the printer after printing. Although the added layer slightly affected the impedance of the antenna's surface, its impact on the overall performance was taken into careful consideration. Since PLA is not a perfect dielectric, it introduces some level of loss. Therefore, a thorough study was conducted to examine the impact of the dielectric loss tangent (δ) on the antenna's radiation pattern. The simulations included the effects of material loss to accurately evaluate the antenna's performance.

The directivity and gain of the antennas, accounting for the losses introduced by the material properties, were analyzed. The results, as presented in Fig. 6.13, indicate that the dielectric loss tangent (δ) has only a minor effect on the radiation pattern. This demonstrates that the chosen δ value enables the antenna to maintain a radiation pattern that meets the desired specifications.

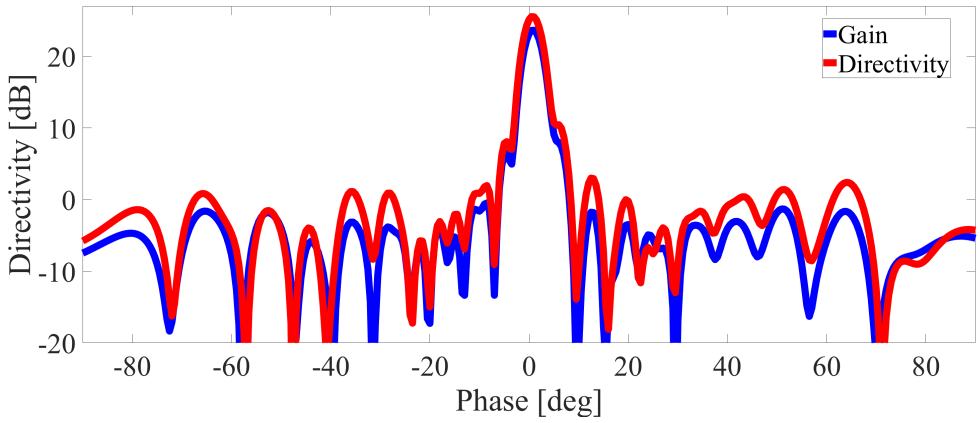

Figure 6.13: Directivity versus gain for the full dielectric antenna when a dielectric loss tangent, δ of 0.018, is introduced into the dielectric properties.

To ensure accurate printing of this antenna, specific adjustments were made to optimize adhesion and smoothness. The initial layer was printed at a significantly reduced speed of 10 mm/s to enhance filament adhesion to the bed and minimize the risk of lifting. Additionally, to further prevent lifting issues, the designed raft, which acts as the attachment point for the ground plane, was modified to have a circular shape instead of a square. This circular design eliminates corners that might be susceptible to lifting due to insufficient adhesion or inadvertent displacement caused by the extruder. In terms of temperature settings, the bed temperature for PLA printing is typically set around 60^{o}C. However, for this particular print, the bed temperature was raised to 65^{o}C. This adjustment promotes a smoother base layer and improves the adhesion of the printed object to the printing surface. Moreover, while the standard extruder temperature for PLA printing is approximately 205^{o}C, the temperature

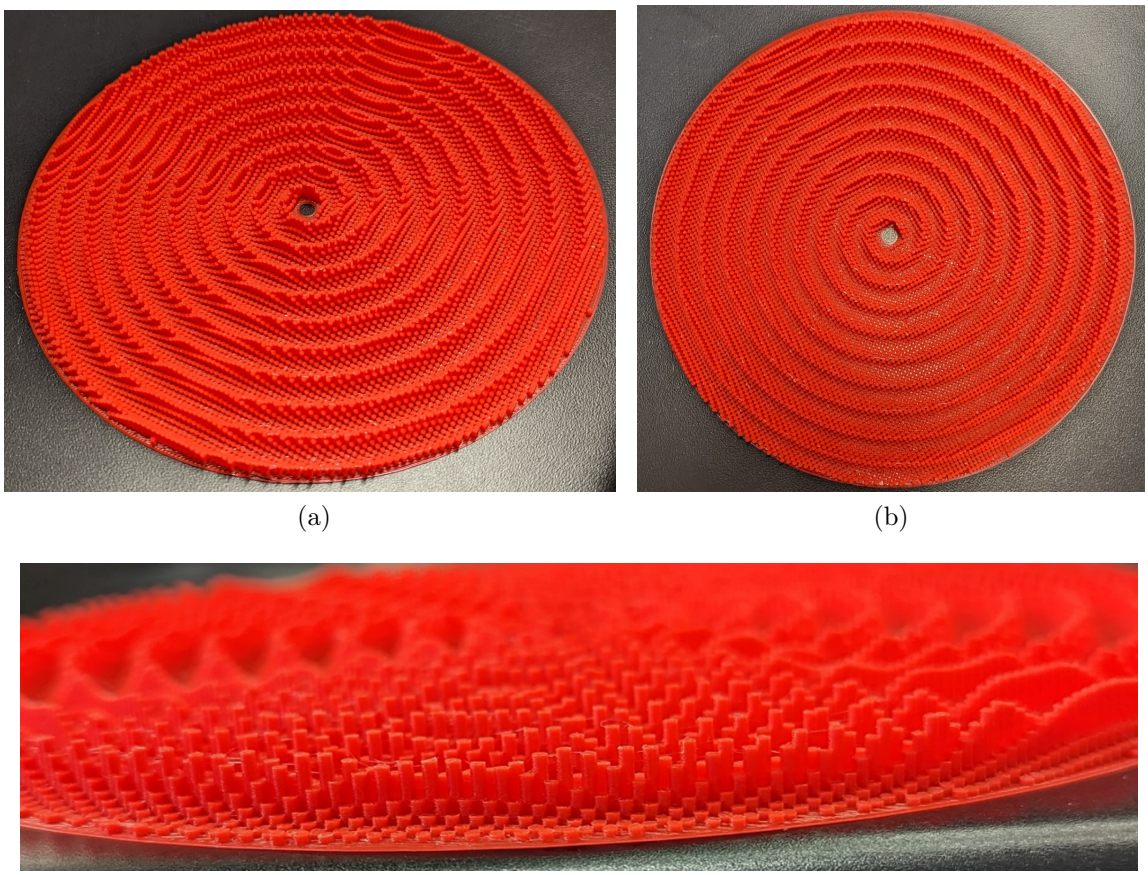

(a) (b)

(c)

Figure 6.14: Various angles showing the additive manufactured final prototype of the broadside, fully dielectric antenna made of cylindrical pins.

was slightly lessened to 195^{o}C for this specific print. The lower extruder temperature contributes to improved smoothness during the extrusion process and minimizes the occurrence of stringiness. Furthermore, additional settings were carefully fine-tuned to optimize print quality. The layer heights for the pin layer were reduced to 0.1 mm, resulting in finer details and a more refined surface finish. Additionally, the print speed was increased to 25 mm/s to ensure a consistently smooth surface without the appearance of a stacked coin-like texture along the edges. By meticulously adjusting these printing parameters, the objective was to achieve a high-quality print characterized by strong adhesion, enhanced smoothness, and an aesthetically pleasing appearance.

This chapter presented an efficient and accurate approach for characterizing additive-manufactured MTSs consisting of dielectric pins on a dielectric slab. It presents a way to model the MTS composed of purely dielectric pins as a uniaxially anisotropic grounded slab, providing a dispersion equation for the fundamental TM mode. Numerical results demonstrate the accuracy of the proposed approach for the antenna design. The antennas were simulated using PLA. The Raise3D Pro printer and PLA material were utilized for printing, with careful considerations made to optimize printing accuracy. Parameters such as pin radius, printing speed, layer height, and temperatures were adjusted to ensure precise printing and smoothness. The impact of dielectric loss was studied, and results indicated that the chosen loss tangent had only a minor effect on the antenna's radiation pattern, demonstrating its suitability for the design's specifications.

CHAPTER 7: TIME VARYING CAPACITOR AND ENERGY BALANCE

One of the hottest topics in current electromagnetics and photonics research is the study of structures with parameters, such as permittivity and/or permeability, varying in time. Exploiting time as a new degree of freedom for the control of electromagnetic waves has enabled the development of structures with intriguing functionalities, such as time-Floquet topological insulators [88, 89, 90], temporal-based non-reciprocity [91, 92, 93], static-to-dynamic field conversion [94], that overcome most of the challenges faced by time-invariant structures. Recently, the platform of time-varying media has also been combined with the concept of metamaterials, opening up another interesting avenue to control and achieve desired functionalities in wave-matter interaction [95, 96, 97, 98, 99, 100, 101, 102, 103]. In addition to physics and engineering, research on time-variant systems has been aggressively pursued in mechanics [104], acoustics [105], and water-wave [106].

An important subclass of electromagnetic time-varying media is represented by time-varying networks consisting of lumped elements, such as resistors, capacitors, and inductors with time-dependent properties. These networks have stimulated a great deal of research interest [107, 108, 109, 110, 92, 111, 112]. In addition to providing an interesting platform to control and manipulate electromagnetic waves, they are also more amenable for experimental demonstrations than the conventional time-varying media [92, 111, 112]. The vast majority of studies related to temporal-dependent networks have been limited to lumped elements periodically modulated in time. On the other hand, lumped elements with aperiodic time modulation can provide an extra degree of freedom to engineer time-variant networks with new functionalities. Indeed, it has been recently shown how reactive elements, like capacitors

and inductors, judiciously modulated in time can provide an alternative for electromagnetic energy accumulation in a transmission line scenario [113, 114]. For example, [113] showed how reactive elements, albeit lossless, when experiencing a temporal variation, exhibit a resistive behavior responsible for the incoming signal absorption. However, this approach requires capacitors or inductors with extreme values, including negative ones, which may be challenging to achieve from a practical standpoint. A follow-up proposal [114] showed that this issue can be overcome if modulation is applied to a coupling network between an LC-resonator and a feeding transmission line, which allows transferring the incoming energy to the LC network by applying slow modulation. Both of these approaches work for harmonic input signals and no technique exists for capturing of arbitrary pulses.

This work is motivated by the recent interest in harnessing electromagnetic energy accumulation through time-varying lumped elements. It presents a novel approach for capturing the energy of any arbitrary pulse by introducing non-periodic modulation to a single capacitor located at the end of a transmission line. The study clarifies the limitations of a previously proposed method and explains how combining an incoming pulse with a DC signal effectively mitigates the need for extreme capacitance values. Furthermore, the research includes a fundamental derivation of the system's energy balance, demonstrating that the energy from the pulse is transferred to the modulation source rather than being stored in the capacitor. This investigation aims to advance the understanding of energy capture and storage in time-varying systems.

This chapter is structured as follows: Section 7.1 introduces the investigated system, comprising a transmission line terminated with a time-varying capacitor charged by a DC voltage connected at the opposite end of the transmission line. Section 7.2 presents the derivation of the required temporal capacitance profile for achieving a reflectionless system, which is further examined through the analysis of two specific incoming voltage pulses in Sections 7.2.1 and 7.2.2. Section 7.3 focuses on deriv-

ing the system's energy balance from first principles, while Sections 7.3.1 and 7.3.2 elaborate on the energy exchange mechanisms for the incoming pulses discussed in Sections 7.2.1 and 7.2.2, respectively. Finally, Section 7.4 presents the conclusions drawn from this study.

7.1 Statement of the problem

Figure 7.1 provides a schematic representation of the studied system: a lossless transmission line terminated with a time-varying capacitor. The input port is connected to a DC voltage source (V_{dc}). After the DC source has charged the capacitor completely, initially at $t = -\infty$, a voltage pulse $[v^+(t,z)]$ begins propagating along the transmission line towards the capacitive load. It is assumed that the DC voltage source remains connected to the system even for $t > -\infty$, and for simplicity, throughout the paper, it is assumed that $V_{dc} > 0$. The combined instantaneous voltage and current at the load position ($z = 0$) can be expressed as follows:

$$v(t) = v^+(t,0) + v^-(t,0) + V_{dc} \tag{7.1a}$$

$$i(t) = \frac{v^+(t,0) - v^-(t,0)}{Z_0} \tag{7.1b}$$

Here, Z_0 represents the characteristic impedance of the transmission line. To explore the possibility of trapping the energy of the incoming voltage pulse in the capacitor, the first step is to determine the temporal variation of its capacitance to fully eliminate the reflected pulse, which will be discussed in the next section.

7.2 Reflectionless time-dependent capacitor

The elimination of reflected pulses in a time-varying capacitive load is demonstrated by exploiting the temporal dependence of capacitance. Unlike stationary purely capacitive loads, which exhibit a reflection coefficient with a magnitude of one, resulting in total pulse reflection, this work reveals a method to fully eliminate the reflected

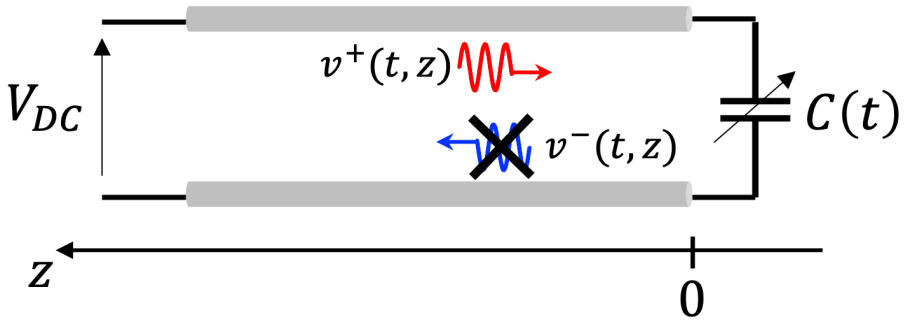

Figure 7.1: A DC voltage source V_{dc} is connected to a time-varying capacitor through a transmission line with characteristic impedance Z_0. The incoming voltage pulse $v^+(t,z)$ (red arrow) travels toward the capacitor, while the reflected voltage pulse $v^-(t,z)$ (blue arrow) travels away from the same capacitive load. The capacitor can eliminate the reflected pulse as long as its capacitance experiences a suitable temporal modulation.

pulse. To achieve this, zero reflection ($v^-(t,z) = 0$) is first imposed, and then, by substituting Eqs. 7.1a and 7.1b into the capacitor equation for current and voltage ($i = \frac{d}{dt}(Cv)$), a first-order ordinary differential equation is obtained:

$$\frac{dC(t)}{dt} + \frac{C(t)}{v^+(t,0) + V_{dc}} \frac{dv^+(t,0)}{dt} = \frac{v^+(t,0)}{Z_0\left(v^+(t,0) + V_{dc}\right)} \tag{7.2}$$

with a solution with respect to $C(t)$ as

$$C(t) = \frac{v^+(-\infty,0) + V_{dc}}{v^+(t,0) + V_{dc}} \left[\frac{1}{Z_0\left(v^+(-\infty,0) + V_{dc}\right)} \int_{-\infty}^{t} v^+(\varepsilon,0)\, d\varepsilon + C_i \right] \tag{7.3}$$

This equation, given the incoming pulse $v^+(t,z)$, provides the required temporal variation of the capacitance with initial value C_i to eliminate the reflected pulse in the system of Fig. 7.1. Inspecting Eq. 7.3, one can observe that $C(t)$ diverges for $v^+(t,0) = -V_{dc}$. In order to avoid extreme capacitive values, it is important to have a DC voltage across the capacitor outside the range of values of the incoming voltage pulse ($V_{dc} > |v^+(t,0)|$). This simple analysis elucidates the extreme capacitive values required in the approach proposed in [113], which did not include a DC source and,

as a result, required a capacitive value tending to infinity.

Another important physical quantity to bring into the discussion, as will become clear shortly, is the temporal variation of the charge in the capacitor to cancel the reflected pulse. Recalling the capacitor charge-voltage relationship ($q = Cv$), it is straightforward to derive the temporal variation of the charge in the capacitor with respect to its initial value ($q_i = C_i V_{dc}$) from Eq. 7.3

$$\Delta q\left(t\right) = C\left(t\right)\left[V_{dc} + v^{+}\left(t,0\right)\right] - C_i V_{dc} \tag{7.4}$$

To delve deeper into the implications of the previously mentioned equations and their underlying physical principles, two distinct temporal shapes of incoming voltage pulses are now considered.

7.2.1 First-order derivative of a Gaussian pulse

The mathematical expression of a normalized voltage pulse with a temporal profile of the first-order derivative of the Gaussian function, which is shown in the inset of Fig. 7.2(a), can be written as $v_{dg}^{+}\left(t,z\right) = -\frac{t-v_p z-\mu}{\sigma^2} e^{-\frac{\left(t-v_p z-\mu\right)^2-\sigma^2}{2\sigma^2}}$, with μ being the zero crossing position, v_p the phase velocity, and σ a positive real number controlling the width of the pulse. Substituting $v_{dg}^{+}\left(t,z\right)$ into Eq. 7.3 and simplifying, it becomes

$$C_{dg}\left(t\right) = \frac{V_{dc}}{v_{dg}^{+}\left(t,0\right) + V_{dc}}\left[\frac{\sigma}{Z_0 V_{dc}} e^{-\frac{\left(t-\mu\right)^2-\sigma^2}{2\sigma^2}} + C_i\right] \tag{7.5}$$

which is the required modulation of the capacitor to eliminate the reflected pulse in the transmission line of Fig. 7.1 with $v^{+}\left(t,z\right) = v_{dg}^{+}\left(t,z\right)$. Fig. 7.2(a) displays the temporal evolution of C_{dg} for three different values of V_{dc}. One can observe that as the incoming pulse approaches the capacitor its capacitance (C_{dg}) starts varying in time, as expected. During the transient time, the range of variation of C_{dg} depends on V_{dc}. The larger V_{dc} is, the smaller the range of variation of C_{dg} is. After the transient

time, C_{dg} returns to its initial value (C_i) for all the three V_{dc} values. This fact can also be rigorously seen by taking the limit $t \to \infty$ in Eq. 7.5. To comprehend the underlying physical rationale for this outcome, the time-dependent equation of the charge in the capacitor is derived by combining Eq.7.5 with Eq.7.4.

$$\Delta q_{dg}(t) = \frac{\sigma}{Z_0} e^{-\frac{(t-\mu)^2-\sigma^2}{2\sigma^2}} \tag{7.6}$$

The temporal evolution of the charge is shown in Fig. 7.2(b). Δq_{dg} exhibits a Gaussian-like temporal variation and tends to zero for $t \to \infty$. As a result, the charge stored in the capacitor is identical before and after the transient time. And, in contrast to C_{dg}, Δq_{dg} does not depend on V_{dc}. This behavior of Δq_{dg} is expectedly consistent with the law of charge conservation, which, for the system under study, can be expressed as $\Delta q_{dg}(t) = \int_{-\infty}^{t} i_{dg}^{+}(\varepsilon, 0)\, d\varepsilon$ with $i_{dg}^{+} = v_{dg}^{+}/Z_0$. As can be seen from the former equation, Δq_{dg} depends only on the voltage of the pulse, but not on V_{dc}. For large t (after the transient time), given the odd symmetry of v_{dg}^{+} [see the inset of Fig. 7.2(a)], the previous integral is zero, which implies that the amount of current flowing in and out of the capacitor during the transient time is the same, resulting in a zero net flow of charge. Thus, the initial and final capacitance/charge values are identical. Therefore, for an incoming pulse with the temporal profile given by the derivative of a Gaussian pulse, the capacitor of the system under study (Fig. 7.1), with a capacitance variation as in Eq. 7.5, eliminates the reflected pulse and does not accumulate any additional charge with respect to the initial one provided by the DC source. This analysis also explains why the peak value of C decreases with increasing V_{dc} and can be generalized to any pulse with a zero net charge.

7.2.2 Gaussian pulse

Now, let us consider the following incoming Gaussian pulse: $v_g^{+}(t, z) = Ae^{-\frac{(t-v_p z-\mu)^2}{2\sigma^2}}$ with μ the position of the peak A, which it is assumed to be a real number, and σ,

the standard deviation, controlling the temporal extension of the pulse. Substituting $v_g^+(t,z)$ into Eq. 7.3, the required modulation of the capacitive load in the system under investigation (Fig. 7.1) to achieve the reflectionless condition for an incoming Gaussian pulse is obtained

$$C_g(t) = \frac{V_{dc}}{Ae^{-\frac{(t-\mu)^2}{2\sigma^2}} + V_{dc}} \left[\frac{A\sigma\sqrt{\frac{\pi}{2}}}{Z_0 V_{dc}} \left(1 + \operatorname{erf}\left(\frac{t-\mu}{\sqrt{2}\sigma} \right) \right) + C_i \right] \tag{7.7}$$

with erf being the Gauss error function [$\operatorname{erf}(\mathrm{y}) = \frac{2}{\sqrt{\pi}} \int_0^{\mathrm{y}} \mathrm{e}^{-\mathrm{y}^2} \mathrm{dy}$]. Combining the previous equation with Eq. 7.4, the time-dependent equation of the charge is obtained.

$$\Delta q_g(t) = \frac{A\sigma\sqrt{\frac{\pi}{2}}}{Z_0} \left(1 + \operatorname{erf}\left(\frac{t-\mu}{\sqrt{2}\sigma} \right) \right) \tag{7.8}$$

Eqs. 7.7 and 7.8 for large t, simplifies to

$$C_g(t \to \infty) = \sqrt{2\pi} \frac{A\sigma}{Z_0 V_{dc}} + C_i \tag{7.9}$$

and

$$\Delta q_g(t \to \infty) = \frac{A\sigma\sqrt{2\pi}}{Z_0}, \tag{7.10}$$

respectively. From Eqs. 7.7 and 7.8, it can be seen that C_g and Δq_g may behave differently depending on the sign of the Gaussian pulse amplitude (A). Let us consider, first, the case with $A > 0$, say $A = 1$. With this amplitude of the Gaussian pulse, the temporal evolution of $C_g(t)$ is shown in Fig. 7.2(c) for three different V_{dc} values. As observed, $C_g(t)$ varies during the transient time, and then stabilizes at a certain value, reaching a value that is higher than the initial one. The range of variation decreases with increasing V_{dc}. Thus, the value of $C_g(t)$ after the transient time (for large t) gets closer to the initial one for higher V_{dc}, as predicted by Eq. 7.9. According to Eq. 7.8, the temporal evolution of $\Delta q_g(t)$, which is shown in Fig. 7.2(d), is independent of V_{dc}.

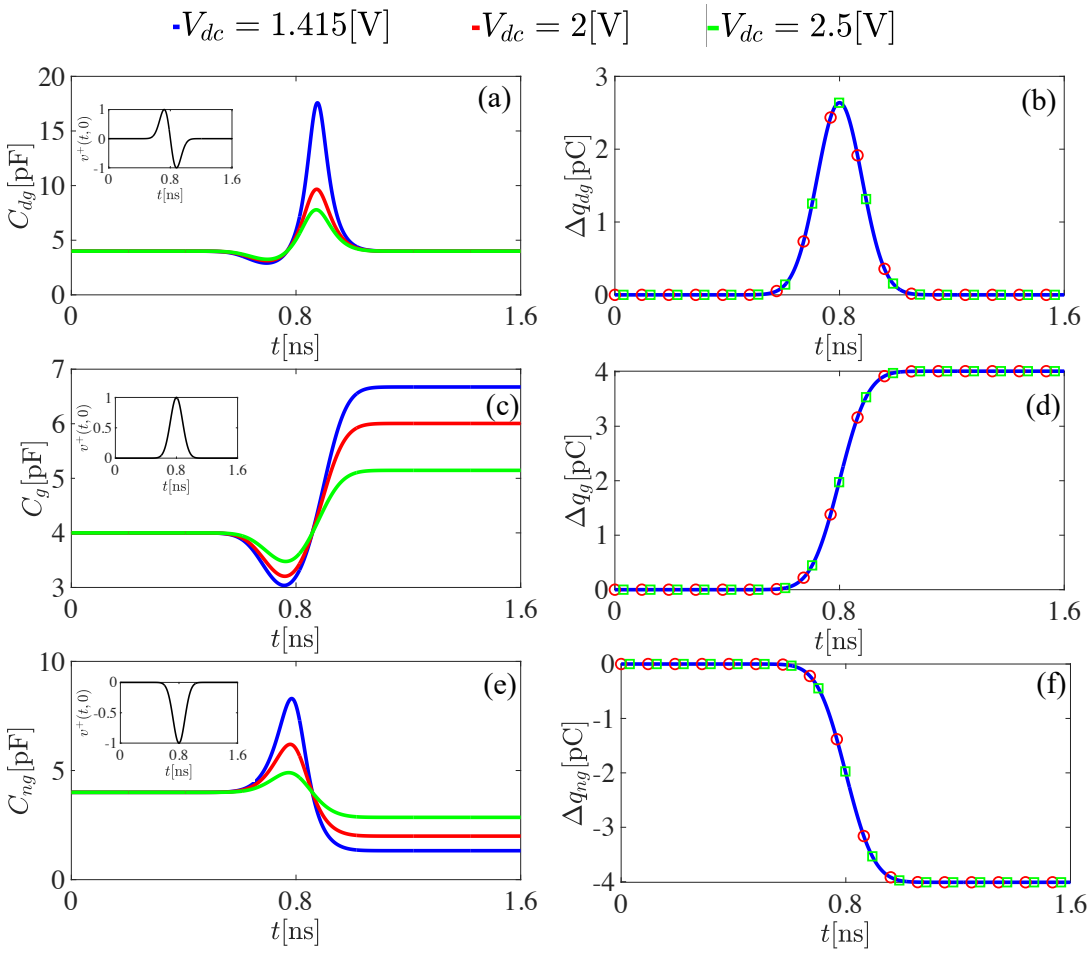

Figure 7.2: Time dependence of the capacitance and charge experienced by the capacitor in the system of Fig. 7.1 to achieve the reflectionless condition for three different temporal shapes of the incoming pulse: (a) and (b) first-order derivative of the Gaussian function; (c) and (d) Gaussian function with positive peak: (e) and (f) Gaussian function with negative peak. Each panel display three curves corresponding to three different values of V_{dc} indicated above the panels (a) and (b). The insets in (a), (c), and (d) show the profile of the considered incoming pulse. The results were obtained for $Z_0 = 50\Omega$, $C_i = 4$pF, $\mu = 0.8$ns, and $\sigma = 0.08$ns.

And, after the transient time, the charge stored in the capacitor is increased. As can be seen in Eq. 7.10, the amount of charge stored in the capacitor after the transient depends on the parameters characterizing the Gaussian pulse, specifically the amplitude A and the standard deviation σ. Note that the discussion on the law of charge conservation carried out for the incoming pulse considered in the previous section can be repeated for an incoming pulse with an arbitrary temporal shape. Accordingly,

the growth of charge experienced by the capacitor for the incoming Gaussian pulse with positive amplitude results from the current ($\frac{v_g^+(t,z)}{Z_0}$) that this pulse induces in the transmission line, which implies a positive net flow of charge toward the capacitor. This charge is accumulated in the capacitor and is responsible for the different final capacitor value than the initial one.

Now, let us consider the case when the amplitude of the incoming Gaussian pulse $[v_g^+(t,z)]$ is a negative real number, $A < 0$. The profile of $v_g^+(t,z)$ with $A = -1$ is shown in the inset of Fig. 7.2(e). To eliminate the reflection from this pulse the capacitor of the system in Fig. 7.1 needs to experience the temporal variation of its capacitance and charge shown in Figs. 7.2(e) and (f), respectively. These plots are obtained from Eqs. 7.7 and 7.8 and, to differentiate the notation between these results and the ones of Figs. 7.2(c) and (d) (corresponding to $A = 1$), $C_g(t)$ and $\Delta q_g(t)$ have been replaced with $C_{ng}(t)$ and $\Delta q_{ng}(t)$, respectively. As one can observe from Figs. 7.2(e) and (f), the temporal evolution of $C_{ng}(t)$ and $\Delta q_{ng}(t)$ is flipped along the vertical axis with respect to the case with $A = 1$ (see Figs. 7.2(c) and (d)). With $A = -1$, or more generally when the amplitude of the Gaussian pulse is negative, the current associated to this pulse flows toward the DC source. This current, according to the law of charge conservation, induces a flow of charge out of the capacitor. As a result, the charge stored in the capacitor and its capacitance after the transient decrease, as predicted by Eqs. 7.9 and (7.10) with $A < 0$. Thus, when the peak of the Gaussian pulse is negative, the capacitor experiencing a temporal modulation of its capacitance given by Eq. 7.7 eliminates the reflected pulse and releases part of its charge into the transmission line.

7.3 Energy exchange process

Another essential aspect of the system in Fig. 7.1 is the energy exchange process between the dynamic energy associated to the incoming pulse and the electrostatic energy stored in the capacitor before and after the transient time. Exploring this aspect

will address the following fundamental question: How much of the incoming pulse's energy is trapped in the capacitor, and how much is transferred to the modulation source? The dynamic energy associated to the pulse is given by

$$W_i^d = \int_{-\infty}^{\infty} \left(v^+(t,z) + V_{DC}\right) i^+(t,z)\, dt = \int_{-\infty}^{\infty} v^+(t,z)\, i^+(t,z)\, dt + V_{dc} \int_{-\infty}^{\infty} i^+(t,z)\, dt \tag{7.11}$$

On the right-hand side of the previous equation, the first and second terms are the energy carried by the pulse (W^p) and the energy due to the current of a pulse flowing in a charged transmission line (W^c), respectively. The latter, upon applying the law of charge conservation and considering that the charge is conserved in time-varying capacitor, becomes $W^c = V_{dc}\Delta q^\infty = V_{dc}\,(q_f - q_i)$, with q_f denoting the final charge stored in the capacitor. Note that Δq^∞ coincides with Eq. 7.4 by letting $t \to \infty$. Thus, Eq. 7.11 can be expressed in a compact form as $W_i^d = W^p + W^c$. Then, the energy balance is expressed as $\Delta W = W_f^s - W_i^d - W_i^s$, where $W_i^s = \frac{1}{2} q_i V_{dc}$ and $W_f^s = \frac{1}{2} q_f V_{dc}$ are the electrostatic energy stored in the capacitor before and after the transient time, respectively, ΔW is equal to the energy given by the modulation agent to the network. It is easy to show that

$$\Delta W = -W^p - \frac{1}{2} V_{dc} \Delta q^\infty \tag{7.12}$$

The energy-balance equation presented here is general and not restricted to a specific temporal shape of the incoming pulse. It allows for an understanding, from first principles, of the energy exchange mechanism in the system of Fig. 7.1 operating in the reflectionless mode. Inspecting Eq. 7.12, one can observe that the first term on the right-hand side, which is related to the energy of the incoming pulse, is a negative term in the energy balance regardless of the pulse time shape and the DC source. This implies that a time-varying capacitor terminating a transmission line cannot trap the

energy of the incoming pulse, which is transferred to the modulation source. On the other hand, the second term on the right-hand side of Eq. 7.12, which is related to the energy associated to the current of the pulse flowing in a charged transmission line (W^c), implies different energetic changes in the system depending on the sign of Δq^∞.

For $\Delta q^\infty < 0$, which occurs for incoming pulses such as the Gaussian pulse with negative peak investigated above, the energy exchange process undergoing in the system is schematically shown in Fig. 7.3(a). As indicated in Sec. 7.1, $V_{dc} > 0$ is assumed. The following discussion can be easily extended to the case with $V_{dc} < 0$. The energy associated to the current of the pulse flowing in a charged transmission line is a negative quantity ($W^c = V_{dc}\Delta q^\infty < 0$) resulting in a depletion of the energy in the transmission of an amount equal to W^c that ends up being accumulated in the DC source. As emerged from the second term on the right-hand side of Eq. 7.12, which is a positive quantity with $\Delta q^\infty < 0$ and equals to W^c except for a factor 1/2, half of the energy in the transmission line is restored by the modulation source pumping energy into the system. The other half of the transmission line energy is restored by the capacitor losing part of its charge during the transient time ($\Delta q^\infty < 0$). As discussed above and shown in Fig. 7.3(a), the energy of the incoming pulse is captured by the modulation source. With $\Delta q^\infty < 0$, Eq. 7.12 results in three different energy exchange regimes depending on the DC voltage across the capacitor (V_{dc}). By setting $\Delta W = 0$ in Eq. 7.12, the DC voltage across the capacitor ($V_{dc}^* = 2W^p/|\Delta q^\infty|$) can be determined, ensuring that the energy of the system is "conserved." As shown in Fig. 7.3(a), the modulation source pumps energy into system to restore the energy in the transmission line and captures the energy of the incoming pulse. These two energies balance out when $V_{dc} = V_{dc}^*$ and, as a result, $\Delta W = 0$. This implies that the energy accumulated in the DC source and the energy captured by the modulation source are identical. When $V_{dc} < V_{dc}^*$, $\Delta W < 0$ implying that the energy of the pulse

transferred to the modulation source exceeds the energy that the modulation source pumps into the system and accumulates in the DC source. On the other hand, when $V_{dc} > V_{dc}^{*}$, the modulation source pumps into the system an amount of energy, which is accumulated in the DC source, that is higher the one received from the incoming pulse ($\Delta W > 0$).

For $\Delta q^{\infty} = 0$, which indicates that the initial and final energy stored in the capacitor are identical, according to Eq. 7.12, the only energy exchange taking place in the system is the transfer of the pulse energy to the modulation source [see Fig. 7.3(b)]. This scenario occurs for the family of incoming pulses whose current induces a no net flow of charge along the transmission line, such as the pulse investigated in Sec. 7.2.1 and shown in the inset of Fig.7.2(a).

The last case that needs to be considered is when $\Delta q^{\infty} > 0$, which is shown in Fig. 7.3(c). In this case, the energy associated to the current of the pulse flowing in a charged transmission line ($W^{c} = V_{dc}\Delta q^{\infty} > 0$) travels toward the capacitor. By comparing W^{c} with the expression of the difference between the initial and final energy stored in the capacitor ($\frac{1}{2}\Delta q^{\infty} V_{dc}$), one can observe that they are equal except for a factor 1/2. Hence, the capacitor is only able to capture half of W^{c}. The other half of W^{c}, in addition to the energy of the incoming pulse (W^{p}), is transferred to the modulation source, as emerged from the energy balance equation [Eq. 7.12] that results in $\Delta W < 0$. For the set of incoming pulses that induce a net flow of charge moving toward the capacitor ($\Delta q^{\infty} > 0$), such as the Gaussian pulse with a positive peak investigated in Sec. 7.2.2, the capacitor captures only half of the energy induced by the current of the pulse flowing in a charged transmission line. The other half of this energy and the pulse's energy are transferred to the modulation source.

In the first part of this section, the energy exchange process in the system under study (Fig.7.1) was discussed in a general sense, without limiting it to incoming pulses with specific temporal evolution. To further investigate this process, including the

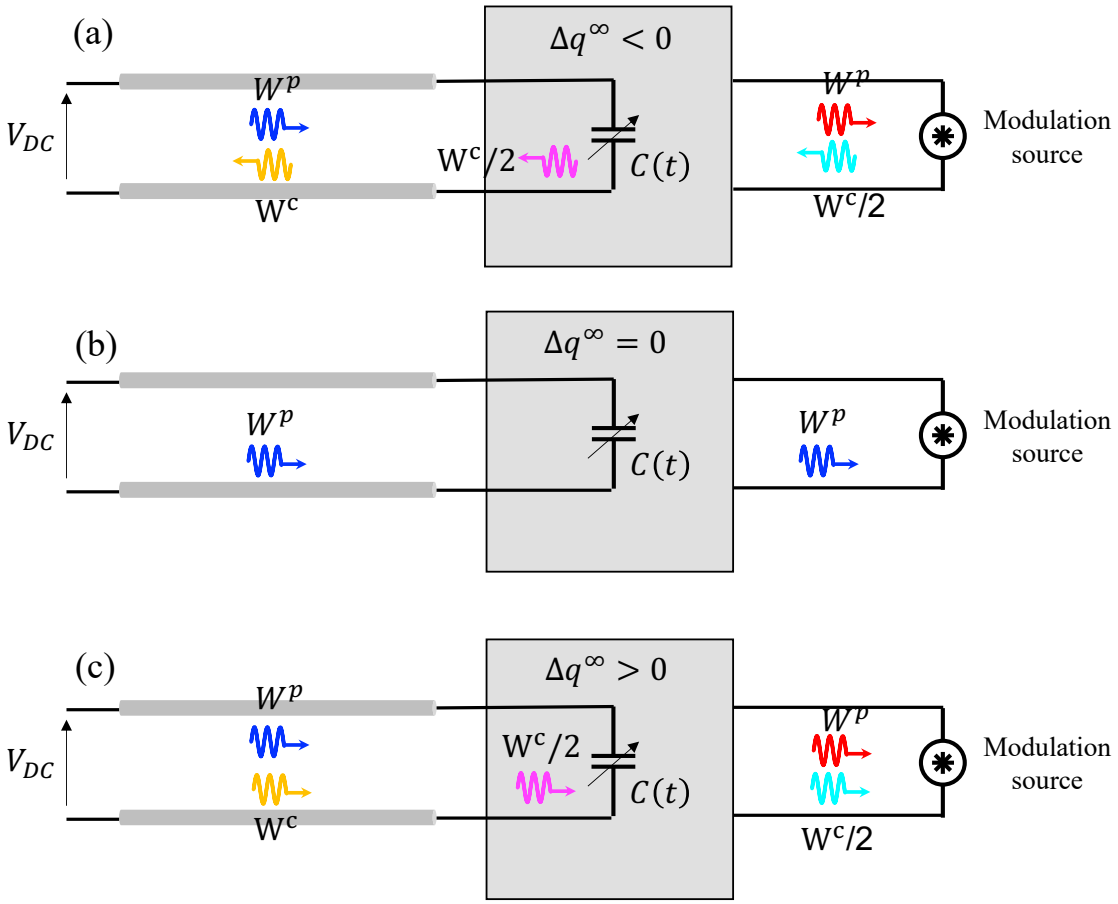

Figure 7.3: Schematic representation of the energy exchange process experienced by the system in Fig. 7.1 operating in the reflectionless regime for incoming pulses that induce (a) a flow of charge moving away from capacitor ($\Delta q^{\infty} < 0$), (b) a zero flow of charge ($\Delta q^{\infty} = 0$), and (c) a flow of charge toward the capacitor ($\Delta q^{\infty} > 0$).

temporal evolution of the energy balance, the focus will now be on the incoming pulses studied in Secs.7.2.1 and 7.2.2.

7.3.1 Energy balance for an incoming pulse with the temporal profile of the first-derivative of a Gaussian function

As can be seen in Fig. 7.2(b), for an incoming pulse consisting of the first-order derivative of the Gaussian function [$v_{dg}^{+}(t,z)$], the final charge in the capacitor (after the transient) is identical to the initial one. When the capacitor accumulates no additional charge during the transient ($\Delta q^{\infty} = 0$), the energy-balance equation [Eq. 7.12]

becomes

$$\Delta W_{dg} = -W_{dg}^{p} \tag{7.13}$$

with W_{dg}^{p} the energy carried by $v_{dg}^{+}(t,z)$, which is transferred to the modulation source, as discussed in the previous section. Since ΔW_{dg} is independent of V_{dc} [see Fig. 7.4(a)], to get a better understanding of the role played by the DC voltage source from energetic standpoint, in Fig. 7.4(b), the temporal evolution of the energy balance has been plotted, and it can be expressed as:

$$\Delta W_{dg}(t) = \frac{1}{2}\left(v_{dg}^{+}(t,z) + V_{dc}\right) v_{dg}^{+}(t,z)\, C_{dg}(t) - \frac{1}{2} V_{dc} \Delta q_{dg}(t) - \int_{-\infty}^{t} \frac{\left(v_{dg}^{+}(\varepsilon,z)\right)^{2}}{Z_0} d\varepsilon \tag{7.14}$$

One can observe that, during the transient time, $\Delta W_{dg}(t)$ depends on V_{dc} exhibiting a larger swing for higher V_{dc} values. This behavior seems to be related to the fact that more energy is stored in the capacitor for higher V_{dc} values. And while the capacitance is experiencing a temporal modulation, more energy is exchanged between the capacitor and the modulation source. After the transient time, the three curves expectedly converge to the same constant negative quantity ($-W_{dg}^{p}$). It can be further investigate this energy exchange mechanism by looking at the instantaneous power balance (P_{dg}), obtained as the derivative of $\Delta W_{dg}(t)$ with respect to time. The temporal evolution of P_{dg} for three values of V_{dc} is shown in Fig. 7.4(c). When P_{dg} is positive (see orangish filled boxes in Fig. 7.4(c)), the instantaneous energy of the pulse is lower than the energy required to modulate the capacitor, which, assuming a mechanical capacitor, is given by $W_{mech}(t) = \frac{1}{2}\left(v_{dg}^{+}(t,z) + V_{DC}\right)^{2} C_{dg}(t)$, and the modulation source needs to supply energy into the system. On the other hand, when P_{dg} is negative (see cyanish filled box in Fig. 7.4(c)), the instantaneous energy of the pulse exceeds the energy required to modulate the capacitor, and a portion of it ends up to the modulation source.

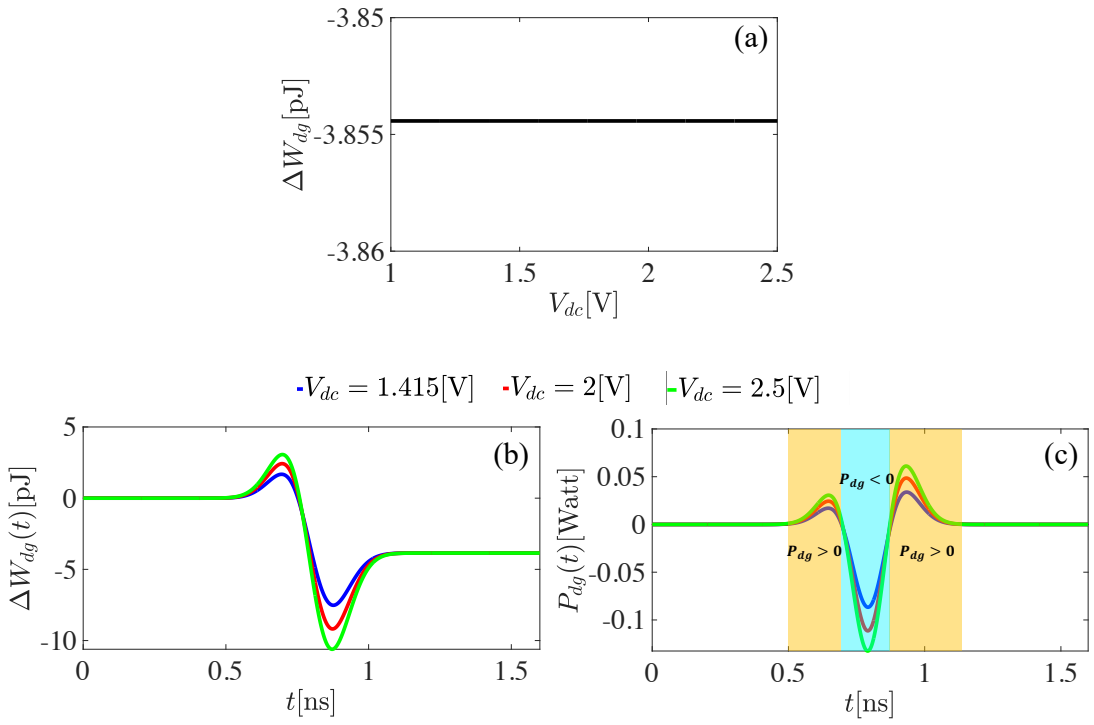

Figure 7.4: Energy exchange process of the system in Fig. 7.1 operating in the reflectionless regime for an incoming pulse given by the first-order derivative of a Gaussian function $[v_{dg}^{+}(t,z)]$. (a) Energy balance as a function of the DC voltage across the capacitor. (b) Instantaneous energy balance and (c) its temporal derivative for three different values of V_{dc}, which are indicated above these panels. The results were obtained for $Z_0 = 50\Omega$, $C_i = 4$pF, $\mu = 0.8$ns, and $\sigma = 0.08$ns.

7.3.2 Energy balance for an incoming pulse with the temporal profile of a Gaussian function

Combining Eq. 7.10 with Eq. 7.12, the energy-balance equation for the incoming Gaussian pulse $v_g^{+}(t,z)$ [Sec. 7.2.2] is obtained

$$\Delta W_g = -\frac{A\sigma}{Z_0}\sqrt{\frac{\pi}{2}}V_{dc} - W_g^p \tag{7.15}$$

with W_g^p representing its energy. One can observe that this energy-balance equation may involve different energetic considerations depending on the sign of A (the peak of the Gaussian pulse). First, let us assume $A > 0$, say $A = 1$ for the sake of consistency with the results shown in Figs. 7.2(c) and (d). With an incoming Gaussian pulse

with this peak, which induces an increase of the final charge stored in the capacitor [see Fig. 7.2(d)], the system experiences the energy exchange mechanism discussed in Sec. 7.3 for the general class of incoming pulses with $\Delta q^{\infty} > 0$ [see Fig. 7.3(c)]. The energy of the pulse (W_g^p) and half of the energy associated to the current of the pulse flowing in a charged transmission are transferred to the modulation source, resulting in $\Delta W_g < 0$ that decreases linearly with V_{dc}, as shown in Fig. 7.5(a). The temporal evolution of ΔW_g, which has been obtained by replacing in 7.14 $v_{dg}^{+}(t,z)$, $C_{dg}(t)$, and $\Delta q_{dg}(t)$ with $v_g^{+}(t,z)$, $C_g(t)$, and $\Delta q_g(t)$, respectively, is shown in Fig. 7.5(b). As observed, higher V_{dc} implies that more energy is exchanged between the capacitor and the modulation source, resulting in a large amount of energy transferred the modulation source, as predicted by Eq. 7.15. Fig. 7.5(c) displays the instantaneous power balance, $P_g(t)$. During the transient time the modulation source, first, supplies power to the system ($P_g(t) > 0$) and, then takes power from the system ($P_g(t) < 0$). Overall, the power taken from the modulation source exceeds the power gain by the system, resulting in a flow power moving toward the modulation source, as expected.

Now, let us consider the case when the peak of the Gaussian pulse is a negative real number, say $A = -1$ for consistency with the results in Figs. 7.2(e) and (f). With this incoming pulse, which induces a decrease of the charge stored in the capacitor (see Fig. 7.2(f)), the system experiences the energy exchange mechanism discussed in Sec. 7.3 for the general class of incoming pulses with $\Delta q^{\infty} < 0$ [see Fig. 7.3(a)] and there are three different energetic regimes depending upon the DC voltage across the capacitor, as can be seen in Fig. 7.6(a). Note that to differentiate this result from the one in Fig.7.5(a), both obtained from Eq.(7.12), we have replaced ΔW_g with ΔW_{ng}. In Fig. 7.6(a), one can observe that there is a specific value of the DC voltage ($V_{dc}^{*} = 1.415$[V]) for which $\Delta W_{ng} = 0$, meaning that the system transfers and receives the same amount of energy from the modulation source. To better understand this energetic regime, the blue-solid curves can be looked at in Figs. 7.6(b) and (c) showing

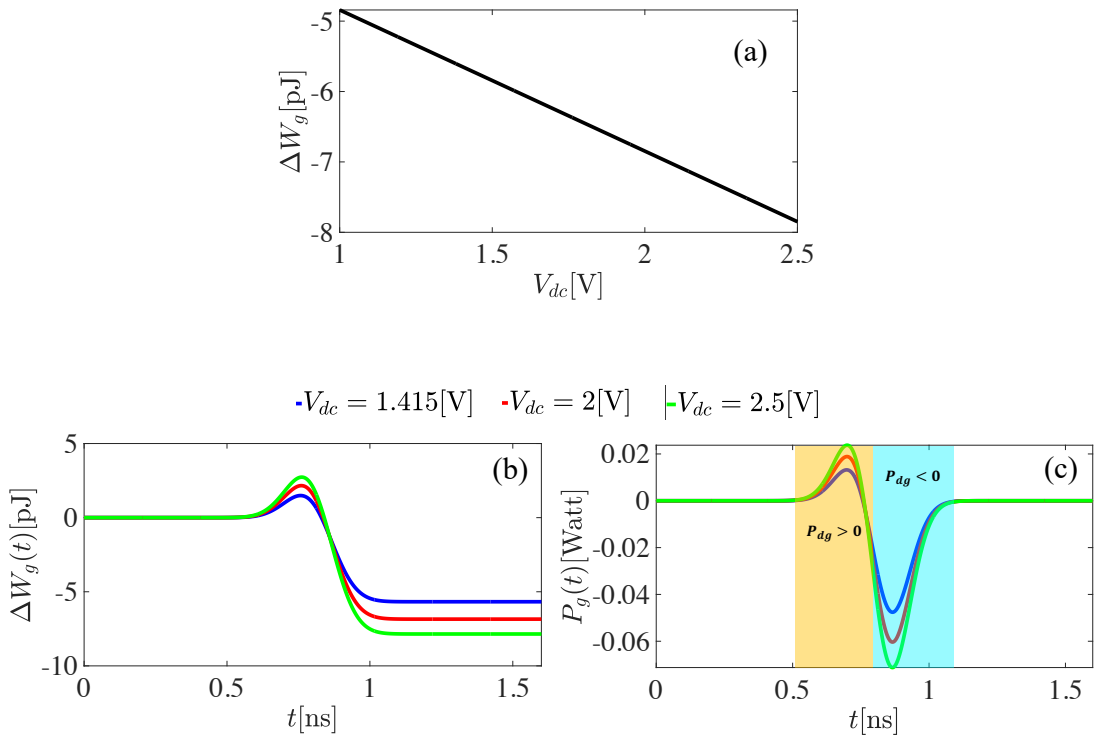

Figure 7.5: Energy exchange process of the system in Fig. 7.1 for an incoming pulse given by a Gaussian function $[v_g^+(t,z)]$ with the peak $A = 1$. (a) Energy balance as a function of the DC voltage across the capacitor. (b) Instantaneous energy balance and (c) its temporal derivative for three different values of V_{dc}, which are indicated above these panels. The results were obtained for $Z_0 = 50\Omega$, $C_i = 4$pF, $\mu = 0.8$ns, and $\sigma = 0.08$ns.

the temporal evolution of the energy balance $[\Delta W_{ng}(t)]$ and power balance $[P_{ng}(t)]$, respectively, for $V_{dc} = V_{dc}^*$. $\Delta W_{ng}(t)$ converging to zero after the transient indicates that the amount of instantaneous energy flowing from the modulation source to the system and accumulate in the DC source is equal to the energy of the pulse captured by the modulation source. This is also confirmed from the temporal profile of $P_{ng}(t)$. During the transient, the portion of the curve with $P_{ng}(t) < 0$ is the upside down image of that with $P_{ng}(t) > 0$. This symmetry implies that systems loses and gains the same amount of power, resulting in a power balance equal to zero as a whole. When the DC voltage across the capacitor is larger than V_{dc}^*, $\Delta W_{ng} > 0$ (see orangish filled box in Fig. 7.6(a)). The amount of energy pumped into the system by the

modulation source that accumulates in the DC source exceeds the energy of the pulse captured by the modulation source. Figs. 7.6(b) and (c) show the temporal evolution of $\Delta W_{ng}(t)$ and $P_{ng}(t)$, respectively, for two different values of V_{dc} larger than V_{dc}^{*} (red- and green-solid curves). $\Delta W_{ng}(t)$ exhibits higher swing for larger V_{dc} resulting in more energy accumulated by the DC source. Similar physical consideration can be made from the temporal profile of $P_{ng}(t)$, which deviates from its symmetric behavior observed for $V_{dc} = V_{dc}^{*}$. The portion of the curve with $P_{ng}(t) > 0$ increases faster than the one with $P_{ng}(t) < 0$, indicating that the modulation source pumps into the system more energy than the one that it receives from the incoming pulse. Finally, for $V_{dc} < V_{dc}^{*}$, $\Delta W_{ng} < 0$ (see cyanish filled box in Fig. 7.6(a)), which is analogous to the cases of Figs. 7.4(c) and 7.5(c). The modulation source pumps less energy into the system than it captures from the incoming pulse.

7.4 Potential Experimental Verification

Before concluding the chapter, a potential pathway for experimentally testing the theoretical phenomenon described above is briefly discussed. In the current state-of-art, two of the most common variable capacitors are represented by MEMS capacitors and varactors, which are mechanically and electronically controlled capacitors, respectively. Using these capacitors, which can typically withstand a maximum voltage of 20 volts, the envisioned experiment would follow these subsequent steps. 1) Given the pulse that needs to be absorbed, the required temporal variation of the capacitor is obtained by Eq. 3. 2) From C(t), the modulation signal that needs to be applied to the capacitor is retrieved according to the capacitor specs. For example, suppose the time-varying capacitor is implemented with a varactor diode. In that case, the modulation signal is represented by the biasing signal and can be obtained from the varactor characteristic curve that relates the capacitance as a function of the reverse bias voltage. 3) Then, the capacitor is connected to a DC voltage source. Once the capacitor is fully charged, the incoming pulse is sent, and the level of reflection is

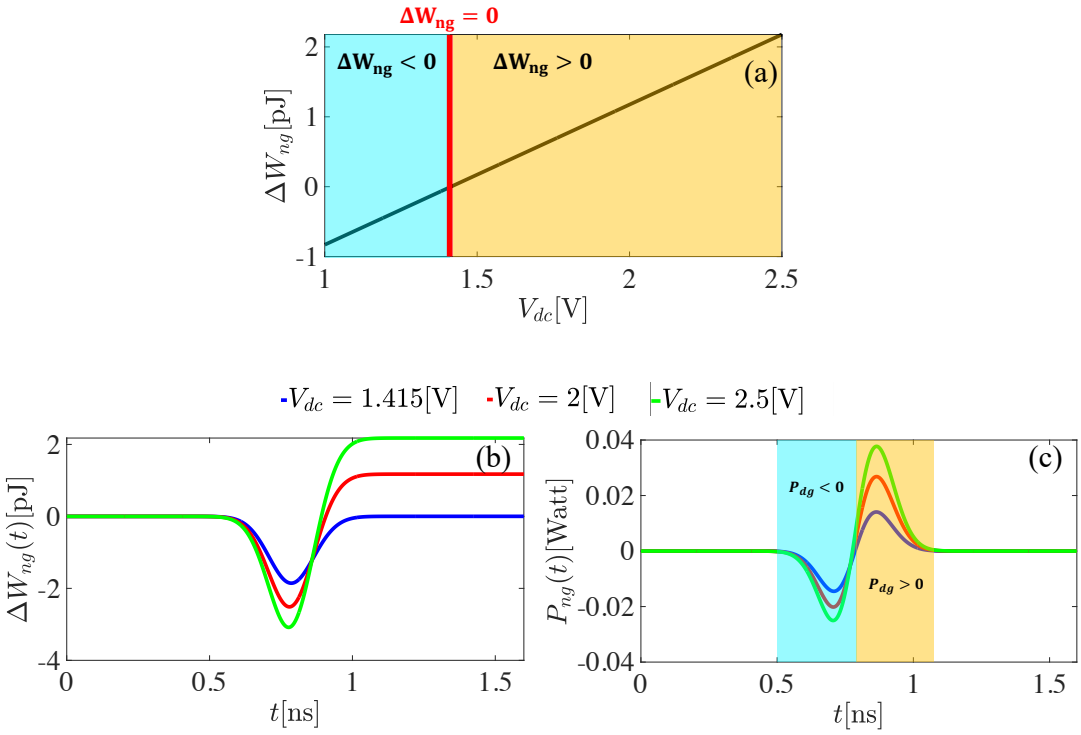

Figure 7.6: Energy exchange process of the system in Fig. 7.1 for an incoming pulse given by a Gaussian function $[v_{ng}^{+}(t,z)]$ with the peak $A=-1$. (a) Energy balance as a function of the DC voltage across the capacitor. (b) Instantaneous energy balance and (c) its temporal derivative for three different values of V_{dc}, which are indicated above these panels. The results were obtained for $Z_0 = 50\Omega$, $C_i = 4\text{pF}$, $\mu = 0.8\text{ns}$, and $\sigma = 0.08\text{ns}$.

measured.

As the equations governing the system are linear, any reflections resulting from perturbations in the system's parameters are expected to be of first order in the perturbations. Therefore, small perturbations on the incoming pulse and/or the temporal profile of the capacitance, as well as nonidealities of the capacitor, are not expected to have a significant effect on the phenomenon presented here.

In this chapter, a theoretical investigation was conducted to explore the capability of a transmission line terminated with a time-varying capacitor to eliminate reflected signals. The study demonstrated that by charging the capacitor with a DC voltage source, it is possible to derive an analytical expression for the required temporal variation of its capacitance, thus avoiding the need for extreme or negative values.

The temporal variation of the capacitance and the resulting evolution of the charge in the capacitor were discussed in detail for two different types of incoming pulses. Furthermore, the energy balance of such a reflectionless time-varying capacitor was derived from first principles, revealing that regardless of the temporal shape of the incoming pulse, its energy is transferred to the modulation source. These findings have the potential to impact a range of applications, including energy storage systems, electrically small antennas, and the conversion of electromagnetic energy into other forms, such as mechanical energy.

CHAPTER 8: CONCLUSION

This dissertation delved into the world of metasurfaces, which have gained recognition for their compactness and lightweight characteristics, promising innovative applications across various domains. These investigations expanded the horizons of metasurface utilization, driven by the potential to transform diverse fields. Whether through the enhancement of functionalities, the streamlining of system designs, or the facilitation of widespread accessibility via inventive fabrication methods, the dissertation highlights the transformative capabilities of metasurfaces.

Metasurfaces are structures highly regarded for their ability to manipulate electromagnetic waves by utilizing periodic elements significantly smaller than the wavelength. Their geometric and sinusoidal arrangement of unit cells offers precise control over properties such as polarization, phase, and wave propagation direction. These unit cells are designed to impose impedance boundary conditions, interacting with electric and magnetic fields. By investigating transverse electric and transverse magnetic waves and applying equivalent circuit theory through a parallel LC resonant circuit model, the surface impedance can be characterized using sheet reactance to account for inductive or capacitive elements. Analyzing individual unit cells results in dispersion curves that provide the necessary impedance information to create the sinusoidal surface gradient. Various analytical techniques, including the Floquet-Bloch theorem, surface impedance characterization, whether it is isotropic or anisotropic, and surface wave dispersion, serve as mathematical methods to describe the behavior of this periodic surface.

Building upon this mathematical and theoretical background, a dual-polarization metascreen was investigated. In an era characterized by a growing demand for com-

pact and multifunctional electromagnetic devices, metasurfaces have emerged as a compelling solution due to their versatile capabilities and lightweight design. Traditional reflect arrays, while effective, often suffer from bulkiness, which led to the exploration of metasurfaces as an alternative approach. In contrast to conventional single-layer metascreens, the proposed three-layer innovative design allowed for the independent control of two orthogonal polarizations, effectively doubling the device's functionality. This achievement was made possible by the metascreen's multiple layers introducing an extra degree of freedom for impedance matching. The metascreen, composed of metallic patches separated by dielectric slabs, was accurately modeled using a local transmission line approach, highlighting its capability to steer incident waves in both the x and y directions, thus introducing much-needed flexibility. The comprehensive analysis, encompassing impedance modeling, unit cell design, and numerical simulations, demonstrated the metascreen's capability to achieve its design objectives of independently steering two polarizations, even at relatively high steering angles. As the boundaries of metasurface design and engineering were continuously pushed, the metascreen held the potential to unlock exciting possibilities in connectivity, sensing, and various other applications.

Another multi-functional antenna was proposed capable of radiating at two different frequencies. The increasing demand for multifrequency medium-to-high gain antennas had spurred innovation in antenna design. Reflectarrays and transmitarrays have been explored but often require external feeds, limiting their suitability for space-constrained applications. This work has introduced a novel approach using MTS antennas with integrated feeds. By leveraging Foster's reactance theorem, the approach demonstrated the design of dual-frequency MTS antenna with a coplanar excitation, addressing the challenges of separation between two distant frequencies in a condensed space. The proposed double-layered MTS antenna had been specifically designed for cloud and precipitation radar applications, showcasing its potential

for operating at common telecommunication frequencies. This work represented a promising avenue for the development of multifrequency antennas with improved performance and versatility.

The antenna design was split into two different antennas with the first antenna investigated being a single layered, single frequency anisotropic antenna operable at W band. The key design elements included a sinusoidally modulated surface impedance described by the impedance tensor components X_{11}, X_{12}, and X_{22}. To achieve the desired impedance profiles, a database of unit cells with varying dimensions based on its spatial dispersion and orientations was created, allowing for an accurate representation of the impedance tensor across the antenna surface. Furthermore, the design process was validated through electromagnetic simulations using Ansys HFSS. The antenna exhibited excellent directivity and low sidelobes, even when operated with a radius smaller than the optimal 20λ, showcasing its potential for efficient radiative performance.

The successful design of an anisotropic MTS antenna operating at 94.05 GHz served as a stepping stone toward more intricate dual-band, dual-layered antenna configurations. Leveraging Foster's reactance theorem, an isotropic antenna was devised, featuring two isolated antennas stacked in a manner that assumed the impedance at the opposite frequency effectively acted as an open circuit, rendering it transparent. Simulation results convincingly demonstrated the efficacy of this approach, with two specific frequencies, 35.75 GHz and 94.05 GHz, chosen as illustrative examples. Reactance databases played a pivotal role in the design of patches for these frequencies, ensuring their efficient operation when integrated into the dual-layered antenna structure. Directivity analysis conclusively confirmed the antenna's capability to efficiently radiate circularly polarized waves at both frequencies, with the directivity patterns of the dual-layered antenna closely mirroring those of the single-layered counterparts.

An additional sinusoidally modulated antenna concept was proposed, featuring

fully dielectric unit cells in its construction. The antenna's design was based on a numerical approach that modeled the unit cell as a uniaxial grounded dielectric slab with an effective anisotropic permittivity. This methodology facilitated a swift and precise analysis of the unit cell's dispersion characteristics, considering various radial or height sizes of the dielectric cylindrical pins for any frequency. To validate the approach, its results were rigorously compared to those found from full-wave simulations, and an impressive level of agreement between the two methodologies was observed. Furthermore, this numerical method demonstrated its versatility by being successfully applied to design antennas for different pointing angles, offering a rapid and efficient design solution for parameter variations. This approach proved effective for designing both broadside and non-broadside radiating antennas with minimal computational time. To align with the expedited design process, the antenna was optimized for easy commercial production using 3D printing technology. This involved fine-tuning printing parameters such as speed, layer height, and temperature settings to enhance adhesion, surface smoothness, and overall print quality. Although the selected dielectric properties introduced some minor dielectric losses, the antennas displayed negligible alterations in their radiation patterns, confirming the suitability of the chosen dielectric parameters for the intended application. Overall, this study demonstrated an efficient numerical method for designing dielectric antennas and showcased the successful fabrication of these antennas using 3D printing technology.

The last project explored the idea of time-varying electromagnetic systems, specifically focusing on structures with varying parameters like permittivity and permeability. This emerging field has opened exciting possibilities for manipulating electromagnetic waves and achieving unique functionalities not attainable with time-invariant structures for various applications of time-varying systems, including topological insulators, non-reciprocal devices, and energy conversion. The subclass of time-varying networks composed of lumped elements, such as capacitors and inductors, with time-

dependent properties are more cooperative to experimental demonstrations than continuous media and offered a platform for controlling electromagnetic waves. While much research has focused on periodically modulated elements, a novel approach using aperiodic time modulation to capture the energy of arbitrary pulses is proposed.

The central focus of this chapter involved an exhaustive investigation into the prerequisites necessary to achieve reflectionless energy absorption in a transmission line, particularly when terminated with a time-varying capacitor. The equations governing the temporal variation of capacitance, a critical factor in realizing reflectionless behavior were presented. To illustrate these concepts, two compelling cases were analyzed: one involving the first-order derivative of a Gaussian pulse and the other featuring a Gaussian pulse in its entirety were shown.

The discovery stemming from this was that by orchestrating the deliberate modulation of the capacitor's characteristics over time, it becomes feasible to eradicate reflected pulses and efficiently accumulate energy. Notably, this achievement does not necessitate the deployment of impractical capacitance values, thanks to the introduction of a DC voltage source into the system. Furthermore, emphasis was placed on demonstrating the preservation of charge throughout this intricate process, casting light on the underlying physical principles at play. The approach centered on the active modulation of capacitance within the termination capacitor, enabling the elimination of pulse reflection, regardless of the temporal shape of the incoming electromagnetic pulse.

Furthermore, the research delved into the energy exchange dynamics within the system, culminating in the development of an energy balance equation. This equation served to quantify the energy absorbed by the time-varying capacitor and its subsequent transfer to the modulation source. This analysis unveiled distinct energy exchange regimes contingent upon the DC voltage applied across the capacitor and the temporal characteristics of the incoming pulse.

The time-varying capacitor and derivations open promising avenues for the development of innovative devices and systems capable of efficiently absorbing and harnessing electromagnetic energy, all while circumventing reflections. With potential applications spanning various fields, this research paves the way for the advancement of energy-efficient technologies and novel electromagnetic systems. This concept carries the potential to revolutionize various domains, ranging from RF engineering to energy harvesting and electromagnetic wave manipulation. The research commenced with the derivation of a crucial analytical expression defining the requisite temporal variation of capacitance for reflectionless absorption, offering valuable insights for practical system design.

8.1 Future Work

In the relentless pursuit of advancing the capabilities and performance of the MTS antennas, this future work section outlines a comprehensive plan for further research and development. The primary objective is to prepare the dual-band antenna for seamless integration into space-bound technology, dedicated to weather research and analysis. This progression begins with a focus on optimizing the individual layers of the antenna, achieved through the careful tapering of the modulation index. Additionally, the decision to maintain circular polarization is guided by the improved efficiency of circularly polarized antennas compared to their linearly polarized counterparts.

With optimized results, the next stage of development involves the fabrication of single band antennas, which will be thoroughly tested. This testing phase is designed to address any potential errors stemming from fabrication and the use of non-ideal materials. To tackle this challenge, a series of design iterations will be undertaken. These iterations will involve slight adjustments to the size of individual patches, both slightly larger and slightly smaller than the original design size. Although the overall dimensions of the antenna will remain constant, these minute variations in

patch size will be important in fine-tuning the design. This iterative process will be applied separately to the single band antennas and then collectively to the dual band antenna. The goal is to identify the most effective antenna design through this methodical approach.

Upon achieving a high-efficiency antenna design that has undergone fabrication and rigorous testing, the antenna technology will be ready for flight applications. This type of antenna holds a distinct advantage in the context of flight readiness due to its ease of fabrication when compared with other flight-certified materials, such as all-metal constructions. Nonetheless, it is essential to acknowledge that the use of dielectric materials, while simplifying fabrication, introduces a trade-off in the form of dielectric losses. This represents a distinction between antenna designs utilizing dielectric materials and those opting for all-metal construction. Antennas designed to be entirely metal-based do not encounter additional losses attributed to dielectrics. This trade-off is a consideration in the selection of materials and designs.

Moreover, the pursuit of a dual band antenna extends to the investigation of an antenna using an all-metal approach. This dual-band antenna targets two frequencies within the Ka band, specifically 32 GHz and 34 GHz. Given the proximity of these frequencies, the two-layer method is not applicable; instead, the design incorporates aperture sharing techniques. This all-metal, dual band antenna will follow a parallel optimization process to its dual layered counterpart. The design of the all metal antenna will evolve from a single-frequency isotropic antenna and then gradually get more complex with two frequencies, anisotropy, and tapering introduced to the impedance profile. The overarching objective remains the same with optimization of this design for maximum efficiency. Upon achieving the optimized design, it will transition to the fabrication and testing phases in preparation for flight.

The all-dielectric antenna will also undergo optimization, focusing on both efficiency and size. The first step for optimization is to determine the optimal size and

materials capable of significantly enhancing the antenna's performance. Once the design and material is finalized, the antenna will be reprinted, and additional components will be integrated, including a ground plane and an SMA connector. The SMA connector will have the center rod tailored to the correct length to ensure impedance matching with the antenna. The connector tuning enables accurate excitation of the surface wave. This antenna will then enter its testing phase to ensure the predicted results match the realized results.

In conclusion, this dissertation has explored the diverse and transformative realms of metasurfaces, multifrequency antennas, and time-varying electromagnetic systems. MTSs enable precise control over electromagnetic wave properties like polarization and phase through impedance boundary conditions, utilizing analytical methods such as equivalent circuit theory and dispersion analysis. This was first shown through a three-layer metascreen that offers independent control of two orthogonal polarizations, expanding its functionality beyond traditional single-layer metascreens. It was then demonstrated with a dual-layered, dual-frequency antenna that operates in different frequency bands for telecommunications. A second MTS antenna presented an efficient numerical approach for designing dielectric antennas with fully dielectric unit cells, successfully validated through comparisons with full-wave simulations. Lastly, MTS technology was demonstrated through investigating the prerequisites for achieving reflectionless energy absorption in transmission lines using time-varying capacitors. This comprehensive research opens exciting possibilities for advanced electromagnetic systems and their applications, promising innovation in a wide range of fields and contributing to the ongoing evolution of communication and energy technologies.

REFERENCES

[1] G. Minatti, M. Faenzi, E. Martini, F. Caminita, P. D. Vita, D. Gonzalez-Ovejero, M. Sabbadini, and S. Maci *IEEE Transactions on Antennas and Propagation*, vol. 63, no. 4, pp. 1288–1300, 2015.

[2] V. G. Veselago, "The Electrodynamics Of Substances With Simultaneously Negative Values Of And μ," *Soviet Physics Uspekhi*, vol. 10, p. 509, apr 1968.

[3] J. Pendry, A. Holden, D. Robbins, and W. Stewart, "Magnetism from conductors and enhanced nonlinear phenomena," *IEEE Transactions on Microwave Theory and Techniques*, vol. 47, no. 11, pp. 2075–2084, 1999.

[4] R. A. Shelby, D. R. Smith, and S. Schultz, "Experimental Verification of a Negative Index of Refraction," *Science*, vol. 292, pp. 77 – 79, 2001.

[5] A. Oliner and A. Hessel, "Guided Waves On Sinusoidally-Modulated Reactance Surfaces," *IRE Transactions on Antennas and Propagation*, vol. 7, no. 5, pp. 201–208, 1959.

[6] B. H. Fong, J. S. Colburn, J. J. Ottusch, J. L. Visher, and D. F. Sievenpiper, "Scalar and Tensor Holographic Artificial Impedance Surfaces," *IEEE Transactions on Antennas and Propagation*, vol. 58, no. 10, pp. 3212–3221, 2010.

[7] S. Maci, G. Minatti, M. Casaletti, and M. Bosiljevac, "Metasurfing: Addressing Waves on Impenetrable Metasurfaces," *IEEE Antennas and Wireless Propagation Letters*, vol. 10, pp. 1499–1502, 2011.

[8] G. Minatti, S. Maci, P. De Vita, A. Freni, and M. Sabbadini, "A Circularly-Polarized Isoflux Antenna Based on Anisotropic Metasurface," *IEEE Transactions on Antennas and Propagation*, vol. 60, no. 11, pp. 4998–5009, 2012.

[9] G. Peeler and H. Coleman, "Microwave Stepped-Index Luneberg Lenses," *IRE Transactions on Antennas and Propagation*, vol. 6, no. 2, pp. 202–207, 1958.

[10] K. Sato and H. Ujiie, "A Plate Luneberg Lens With The Permittivity Distribution Controlled by Hole Density," *Electronics and Communications in Japan (Part I: Communications)*, vol. 85, no. 9, pp. 1–12, 2002.

[11] L. Xue and V. Fusco, "24 GHz Automotive Radar Planar Luneburg Lens," *Microwaves, Antennas & Propagation, IET*, vol. 1, pp. 624–628, 07 2007.

[12] L. Xue and V. F. Fusco, "Printed holey plate Luneburg Lens," *Microwave and Optical Technology Letters*, vol. 50, no. 2, pp. 378–380, 2008.

[13] Young-Jin Park and Herschlein, A. and Wiesbeck, W., "A Photonic Bandgap (PBG) Structure for Guiding and Suppressing Surface Waves in Millimeter-Wave Antennas," *IEEE Transactions on Microwave Theory and Techniques*, vol. 49, no. 10, pp. 1854–1859, 2001.

[14] Casaletti, M. and Caminita, F. and Maci, S., "A Luneburg Lens Designed by Using a Variable Artificial Surface," in *2010 IEEE Antennas and Propagation Society International Symposium*, pp. 1–4, 2010.

[15] Bosiljevac, Marko and Casaletti, Massimiliano and Caminita, Francesco and Sipus, Zvonimir and Maci, Stefano, "Non-Uniform Metasurface Luneburg Lens Antenna Design," *IEEE Transactions on Antennas and Propagation*, vol. 60, no. 9, pp. 4065–4073, 2012.

[16] Parikshit Moitra and Yunzheng Wang and Xinan Liang and Li Lu and Alyssa Poh and Tobias W. W. Mass and Robert E. Simpson and Arseniy I. Kuznetsov and Ramon Paniagua-Dominguez, "Tunable Wavefront Control in the Visible Spectrum Using Low-Loss Chalcogenide Phase Change Metasurfaces," 2022.

[17] Yatooshi, Takumi and Ishikawa, Atsushi and Tsuruta, Kenji, "Terahertz Wavefront Control by Tunable Metasurface Made of Graphene Ribbons," *Applied Physics Letters*, vol. 107, 8 2015.

[18] Pfeiffer, Carl and Grbic, Anthony, "Millimeter-Wave Transmitarrays for Wavefront and Polarization Control," *IEEE Transactions on Microwave Theory and Techniques*, vol. 61, no. 12, pp. 4407–4417, 2013.

[19] Monticone, Francesco and Estakhri, Nasim Mohammadi and Alu, Andrea, "Full Control of Nanoscale Optical Transmission with a Composite Metascreen," *Phys. Rev. Lett.*, vol. 110, p. 203903, May 2013.

[20] Nguyen, Quang and Zaghloul, Amir I., "Design of Beam Steering Patch Arrays Using Self-Phased Metasurface Pixels," in *2020 IEEE International Symposium on Antennas and Propagation and North American Radio Science Meeting*, pp. 909–910, 2020.

[21] Qi, Jiaran and Xiao, Shanshan and Yin, Zhiying and Qiu, Jinghui, "Beam-Steering Multi-Layer Metasurface at 35GHz," in *2016 International Symposium on Antennas and Propagation (ISAP)*, pp. 462–463, 2016.

[22] D. Sheen, D. McMakin, and T. Hall, "Three-Dimensional Millimeter-Wave Imaging for Concealed Weapon Detection," *IEEE Transactions on Microwave Theory and Techniques*, vol. 49, no. 9, pp. 1581–1592, 2001.

[23] S. Raman, N. Barker, and G. Rebeiz, "A w-band dielectric-lens-based integrated monopulse radar receiver," *IEEE Transactions on Microwave Theory and Techniques*, vol. 46, no. 12, pp. 2308–2316, 1998.

[24] G. Floquet, "Sur les équations différentielles linéaires à coefficients périodiques," *Annales scientifiques de l'École Normale Supérieure*, vol. 2e série, 12, pp. 47–88, 1883.

[25] F. Bloch, "Ãber die Quantenmechanik der Elektronen in Kristallgittern," *Zeitschrift fur Physik*, vol. 52, pp. 555–600, July 1929.

[26] D. F. Sievenpiper, *Modern Antenna Handbook*. John Wiley Sons, Inc, 2008.

[27] H. Kaouach, L. Dussopt, J. Lanteri, T. Koleck, and R. Sauleau, "Wideband Low-Loss Linear and Circular Polarization Transmit-Arrays in V-Band," *IEEE Transactions on Antennas and Propagation*, vol. 59, no. 7, pp. 2513–2523, 2011.

[28] N. T. Nguyen, R. Sauleau, and L. Le Coq, "Reduced-Size Double-Shell Lens Antenna With Flat-Top Radiation Pattern for Indoor Communications at Millimeter Waves," *IEEE Transactions on Antennas and Propagation*, vol. 59, no. 6, pp. 2424–2429, 2011.

[29] E. Carrasco, M. Barba, J. A. Encinar, and J. Perruisseau-Carrier, "Reflectarray Element for Beam Scanning With Polarization Flexibility," in *2012 International Symposium on Antennas and Propagation (ISAP)*, pp. 551–554, 2012.

[30] Y. Li, Z. H. Jiang, X. Tong, F. Wu, N. Shen, R. Sauleau, and W. Hong, "Wideband Dual-Circularly-Polarized Reflect-Arrays Based on Dual-Functional-Layer Cells With Berry-Phase Compensation at X-Band," *IEEE Transactions on Antennas and Propagation*, vol. 70, no. 10, pp. 9924–9929, 2022.

[31] F. A. C. S. Lucena, M. R. T. de Oliveira, C. P. N. Silva, T. L. Pedrosa, and M. T. de Melo, "Controlled Directivity and Gain of Antenna Using Square Loop RFSS Based on PIN Diode," in *2017 SBMO/IEEE MTT-S International Microwave and Optoelectronics Conference (IMOC)*, pp. 1–4, 2017.

[32] E. Vassos and A. Feresidis, "Dual-Band Millimetre-wave Phase Shifting Metasurface Element Enabled by Air-Bridged Schottky Diodes," in *2022 16th European Conference on Antennas and Propagation (EuCAP)*, pp. 1–4, 2022.

[33] G. Minatti, F. Caminita, E. Martini, M. Sabbadini, and S. Maci, "Synthesis of Modulated-Metasurface Antennas With Amplitude, Phase, and Polarization Control," *IEEE Trans. Antennas Propag.*, vol. 64, no. 9, pp. 3907–3919, 2016.

[34] M. Faenzi, D. Gonzalez-Ovejero, F. Caminita, and S. Maci, "Dual-Band Self-Diplexed Modulated Metasurface Antennas," in *12th European Conference on Antennas and Propagation (EuCAP 2018)*, pp. 1–4, 2018.

[35] C. Huang, C. Zhang, J. Yang, B. Sun, B. Zhao, and X. Luo, "Reconfigurable Metasurface for Multifunctional Control of Electromagnetic Waves," *Advanced Optical Materials*, vol. 5, no. 22, p. 1700485, 2017.

[36] C. Pfeiffer and A. Grbic, "Millimeter-Wave Transmitarrays for Wavefront and Polarization Control," *IEEE Transactions on Microwave Theory and Techniques*, vol. 61, no. 12, pp. 4407–4417, 2013.

[37] A. Ranjbar and A. Grbic, "Broadband, Multiband, and Multifunctional All-Dielectric Metasurfaces," *Phys. Rev. Appl.*, vol. 11, p. 054066, May 2019.

[38] M. Chen and G. V. Eleftheriades, "Omega-Bianisotropic Wire-Loop Huygensâ Metasurface for Reflectionless Wide-Angle Refraction," *IEEE Transactions on Antennas and Propagation*, vol. 68, no. 3, pp. 1477–1490, 2020.

[39] D. M. Pozar, *Microwave engineering; 3rd ed.* Hoboken, NJ: Wiley, 2005.

[40] M. R. Chaharmir, J. Shaker, N. Gagnon, and D. Lee, "Design of Broadband, Single Layer Dual-Band Large Reflectarray Using Multi Open Loop Elements," *IEEE Trans. Antennas Propag.*, vol. 58, no. 9, pp. 2875–2883, 2010.

[41] L. Guo, P.-K. Tan, and T.-H. Chio, "Single-Layered Broadband Dual-Band Reflectarray With Linear Orthogonal Polarizations," *IEEE Trans. Antennas Propag.*, vol. 64, no. 9, pp. 4064–4068, 2016.

[42] R. S. Malfajani and Z. Atlasbaf, "Design and Implementation of a Dual-Band Single Layer Reflectarray in X and K Bands," *IEEE Trans. Antennas Propag.*, vol. 62, no. 8, pp. 4425–4431, 2014.

[43] C. Han, J. Huang, and K. Chang, "A High Efficiency Offset-Fed X/Ka-Dual-Band Reflectarray Using Thin Membranes," *IEEE Trans. Antennas Propag.*, vol. 53, no. 9, pp. 2792–2798, 2005.

[44] Z. Hamzavi-Zarghani and Z. Atlasbaf, "A New Broadband Single-Layer Dual-Band Reflectarray Antenna in X- and Ku-Bands," *IEEE Trans. Antennas Propag.*, vol. 14, pp. 602–605, 2015.

[45] S.-W. Qu, Q.-Y. Chen, M.-Y. Xia, and X. Y. Zhang, "Single-Layer Dual-Band Reflectarray With Single Linear Polarization," *IEEE Trans. Antennas Propag.*, vol. 62, no. 1, pp. 199–205, 2014.

[46] R. Y. Wu, Y. B. Li, W. Wu, C. B. Shi, and T. J. Cui, "High-Gain Dual-Band Transmitarray," *IEEE Trans. Antennas Propag.*, vol. 65, no. 7, pp. 3481–3488, 2017.

[47] S. A. Matos, E. B. Lima, J. S. Silva, J. R. Costa, C. A. Fernandes, N. J. G. Fonseca, and J. R. Mosig, "High Gain Dual-Band Beam-Steering Transmit Array for Satcom Terminals at Ka-Band," *IEEE Trans. Antennas Propag.*, vol. 65, no. 7, pp. 3528–3539, 2017.

[48] K. T. Pham, R. Sauleau, E. Fourn, F. Diaby, A. Clemente, and L. Dussopt, "Dual-Band Transmitarrays With Dual-Linear Polarization at Ka-Band," *IEEE Trans. Antennas Propag.*, vol. 65, no. 12, pp. 7009–7018, 2017.

[49] T. K. Pham, L. Guang, D. Gonzalez-Ovejero, and R. Sauleau, "Dual-Band Transmitarray With Low Scan Loss for Satcom Applications," *IEEE Trans. Antennas Propag.*, vol. 69, no. 3, pp. 1775–1780, 2021.

[50] A. Aziz, F. Yang, S. Xu, M. Li, and H.-T. Chen, "A High-Gain Dual-Band and Dual-Polarized Transmitarray Using Novel Loop Elements," vol. 18, no. 6, pp. 1213–1217, 2019.

[51] Y.-M. Cai, K. Li, W. Li, S. Gao, Y. Yin, L. Zhao, and W. Hu, "Dual-Band Circularly Polarized Transmitarray With Single Linearly Polarized Feed," *IEEE Trans. Antennas Propag.*, vol. 68, no. 6, pp. 5015–5020, 2020.

[52] B. H. Fong, J. S. Colburn, J. J. Ottusch, J. L. Visher, and D. F. Sievenpiper, "Scalar and Tensor Holographic Artificial Impedance Surfaces," *IEEE Trans. Antennas Propag.*, vol. 58, no. 10, pp. 3212–3221, 2010.

[53] A. M. Patel and A. Grbic, "A Printed Leaky-Wave Antenna Based on a Sinusoidally-Modulated Reactance Surface," *IEEE Trans. Antennas Propag.*, vol. 59, no. 6, pp. 2087–2096, 2011.

[54] G. Minatti, M. Faenzi, E. Martini, F. Caminita, P. De Vita, D. Gonzalez-Ovejero, M. Sabbadini, and S. Maci, "Modulated Metasurface Antennas for Space: Synthesis, Analysis and Realizations," *IEEE Trans. Antennas Propag.*, vol. 63, no. 4, pp. 1288–1300, 2015.

[55] G. Minatti, F. Caminita, E. Martini, and S. Maci, "Flat Optics for Leaky-Waves on Modulated Metasurfaces: Adiabatic Floquet-Wave Analysis," *IEEE Trans. Antennas Propag.*, vol. 64, no. 9, pp. 3896–3906, 2016.

[56] D. Gonzalez-Ovejero, G. Minatti, G. Chattopadhyay, and S. Maci, "Multibeam by Metasurface Antennas," *IEEE Trans. Antennas Propag.*, vol. 65, no. 6, pp. 2923–2930, 2017.

[57] D. Gonzalez-Ovejero, N. Chahat, R. Sauleau, G. Chattopadhyay, S. Maci, and M. Ettorre, "Additive Manufactured Metal-Only Modulated Metasurface Antennas," *IEEE Trans. Antennas Propag.*, vol. 66, no. 11, pp. 6106–6114, 2018.

[58] E. Martini, F. Caminita, and S. Maci, "Double-Scale Homogenized Impedance Models for Periodically Modulated Metasurfaces," *EPJ Appl. Metamat.*, vol. 7, p. 12, 2020.

[59] S. Maci, M. Caiazzo, A. Cucini, and M. Casaletti, "A Pole-Zero Matching Method for EBG Surfaces Composed of a Dipole FSS Printed on a Grounded Dielectric Slab," *IEEE Trans. Antennas Propag.*, vol. 53, no. 1, pp. 70–81, 2005.

[60] M. Bodehou, C. Craeye, and I. Huynen, "Multifrequency Band Synthesis of Modulated Metasurface Antennas," vol. 19, no. 1, pp. 134–138, 2020.

[61] M. Faenzi, D. Gonzalez-Ovejero, and S. Maci, "Overlapped and Sequential Metasurface Modulations for Bi-Chromatic Beams Generation," *Applied Physics Letters*, vol. 118, no. 18, p. 181902, 2021.

[62] J. Budhu, E. Michielssen, and A. Grbic, "The Design of Dual Band Stacked Metasurfaces Using Integral Equations," *IEEE Trans. Antennas Propag.*, vol. 70, no. 6, pp. 4576–4588, 2022.

[63] S. P. Nagaraja, R. R. Monje, and R. Cofield, "Dual Frequency Feed Horn Design for a Compact Cloud and Precipitation Radar Operating at Ka- and W-band," in *2021 International Conference on Electromagnetics in Advanced Applications (ICEAA)*, pp. 257–260, 2021.

[64] O. Luukkonen, C. Simovski, G. Granet, G. Goussetis, D. Lioubtchenko, A. V. Raisanen, and S. A. Tretyakov, "Simple and Accurate Analytical Model of Planar Grids and High-Impedance Surfaces Comprising Metal Strips or Patches," *IEEE Trans. Antennas Propag.*, vol. 56, no. 6, pp. 1624–1632, 2008.

[65] M. Mencagli, E. Martini, and S. Maci, "Surface Wave Dispersion for Anisotropic Metasurfaces Constituted by Elliptical Patches," *IEEE Transactions on Antennas and Propagation*, vol. 63, no. 7, pp. 2992–3003, 2015.

[66] M. Mencagli, E. Martini, and S. Maci, "Transition Function for Closed-Form Representation of Metasurface Reactance," *IEEE Trans. Antennas Propag.*, vol. 64, no. 1, pp. 136–145, 2016.

[67] Minatti, Gabriele and Caminita, Francesco and Martini, Enrica and Maci, Stefano, "Flat Optics for Leaky-Waves on Modulated Metasurfaces: Adiabatic Floquet-Wave Analysis," *IEEE Transactions on Antennas and Propagation*, vol. 64, no. 9, pp. 3896–3906, 2016.

[68] G. Minatti, E. Martini, and S. Maci, "Efficiency of Metasurface Antennas, year=2017, volume=65, number=4, pages=1532-1541, doi=10.1109/TAP.2017.2669728," *IEEE Transactions on Antennas and Propagation.*

[69] Faenzi, Marco and Minatti, Gabriele and Gonzalez-Ovejero, David and Caminita, Francesco and Martini, Enrica and Della Giovampaola, Cristian and Maci, S., "Metasurface Antennas: New Models, Applications and Realizations," *Scientific Reports*, vol. 9, 07 2019.

[70] S. Maci and A. Cucini, *FSS-Based EBG Surfaces*, ch. 13, pp. 351–376. John Wiley & Sons, Ltd, 2006.

[71] G. Minatti, F. Caminita, M. Casaletti, and S. Maci *IEEE Transactions on Antennas and Propagation*, vol. 59, no. 12, pp. 4436–4444, 2011.

[72] R. King, D. Thiel, and K. Park *IEEE Transactions on Antennas and Propagation*, vol. 31, no. 3, pp. 471–476, 1983.

[73] D. Gonzalez-Ovejero, C. Jung-Kubiak, M. Alonso-delPino, T. Reck, and G. Chattopadhyay, "Design, Fabrication and Testing of a Modulated Metasurface Antenna at 300 GHz," in *2017 11th European Conference on Antennas and Propagation (EUCAP)*, pp. 3416–3418, 2017.

[74] S. K. Podilchak, L. Matekovits, A. P. Freundorfer, Y. M. M. Antar, and M. Orefice, "Controlled Leaky-Wave Radiation From a Planar Configuration of Width-Modulated Microstrip Lines," *IEEE Transactions on Antennas and Propagation*, vol. 61, no. 10, pp. 4957–4972, 2013.

[75] M. Bosiljevac, M. Casaletti, F. Caminita, Z. Sipus, and S. Maci, "Non-Uniform Metasurface Luneburg Lens Antenna Design," *IEEE Transactions on Antennas and Propagation*, vol. 60, no. 9, pp. 4065–4073, 2012.

[76] S. K. Podilchak, A. P. Freundorfer, and Y. M. M. Antar, "Planar Surface-Wave Sources and Metallic Grating Lenses for Controlled Guided-Wave Propagation," *IEEE Antennas and Wireless Propagation Letters*, vol. 8, pp. 371–374, 2009.

[77] S. A. Maier, S. R. Andrews, L. Martín-Moreno, and F. J. García-Vidal, "Terahertz Surface Plasmon-Polariton Propagation and Focusing on Periodically Corrugated Metal Wires," *Phys. Rev. Lett.*, vol. 97, p. 176805, Oct 2006.

[78] D. Ramaccia, A. Toscano, and F. Bilotti, "A New Accurate Model of High-Impedance Surfaces Consisting of Circular Patches," *Progress in Electromagnetics Research M*, vol. 21, pp. 1–17, 2011.

[79] O. Luukkonen, C. Simovski, G. Granet, G. Goussetis, D. Lioubtchenko, A. Raisanen, and S. Tretyakov, "Simple and Accurate Analytical Model of Planar Grids and High-Impedance Surfaces Comprising Metal Strips or Patches," *IEEE Transactions on Antennas and Propagation*, vol. 56, pp. 1624–1632, 2008.

[80] Z. Wang, H. Wu, J. Chen, Z. Wu, and Y. Feng, "An Ultralow-Profile Lens Antenna Based on All-Dielectric Metasurfaces," in *2016 IEEE 5th Asia-Pacific Conference on Antennas and Propagation (APCAP)*, pp. 367–368, 2016.

[81] A. Yahyaoui, H. Rmili, T. Aguili, and R. Mittra, "Experimental Characterization of a Circular Polarizer with All-Dielectric Chiral Metasurface," in *2018 International Symposium on Antennas and Propagation (ISAP)*, pp. 1–2, 2018.

[82] D. G. Ovejero, M. Faenzi, A. Mahmoud, M. Ettorre, R. Sauleau, N. Chahat, G. Chattopadhyay, and S. Maci, "Some Recent Developments on Modulated Metasurface Antennas," in *2019 IEEE MTT-S International Microwave and RF Conference (IMARC)*, pp. 1–3, 2019.

[83] M. Mrnka and Z. Raida, "An Effective Permittivity Tensor of Cylindrically Perforated Dielectrics," *IEEE Antennas and Wireless Propagation Letters*, vol. 17, no. 1, pp. 66–69, 2018.

[84] P. Mondal and K. Wu, "A Leaky-Wave Antenna Using Periodic Dielectric Perforation for Millimeter-Wave Applications," *IEEE Transactions on Antennas and Propagation*, vol. 64, no. 12, pp. 5492–5495, 2016.

[85] C. Kittel, *Introduction to Solid State Physics*. Wiley, 8 ed., 2004.

[86] A. Shahvarpour, A. A. Melcon, and C. Caloz, "Bandwidth Enhancement and Beam Squint Reduction of Leaky Modes in a Uniaxially Anisotropic Meta-Substrate," in *2010 IEEE Antennas and Propagation Society International Symposium*, pp. 1–4, 2010.

[87] G. Boussatour, P.-Y. Cresson, B. Genestie, N. Joly, and T. Lasri, "Dielectric Characterization of Polylactic Acid Substrate in the Frequency Band 0.5-67 GHz," *IEEE Microwave and Wireless Components Letters*, vol. 28, no. 5, pp. 374–376, 2018.

[88] N. Lindner, G. Refael, and V. Galitski, "Floquet Topological Insulator in Semiconductor Quantum Wells," *Nature Phys.*, vol. 7, no. 12, pp. 490–495, 2011.

[89] Y. T. Katan and D. Podolsky, "Modulated Floquet Topological Insulators," *Phys. Rev. Lett.*, vol. 110, p. 016802, 2013.

[90] E. Lustig, Y. Sharabi, and M. Segev, "Topological Aspects of Photonic Time Crystals," *Optica*, vol. 5, pp. 1390–1395, Nov 2018.

[91] Z. Yu and S. Fan, "Complete Optical Isolation Created by Indirect Interband Photonic Transitions," *Nature Photon.*, vol. 3, no. 12, pp. 91–94, 2009.

[92] N. A. Estep, D. L. Sounas, J. Soric, and A. Alu, "Magnetic-Free Non-Reciprocity and Isolation Based on Parametrically Modulated Coupled-Resonator Loops," *Nature Phys.*, vol. 10, no. 12, pp. 923–927, 2014.

[93] D. L. Sounas and A. Alu, "Non-Reciprocal Photonics Based on Time Modulation," *Nature Photon.*, vol. 11, no. 12, pp. 774–784, 2017.

[94] M. J. Mencagli, D. L. Sounas, M. Fink, and N. Engheta, "Static-to-Dynamic Field Conversion with Time-Varying Media," *Phys. Rev. B*, vol. 105, p. 144301, Apr 2022.

[95] A. Shlivinski and Y. Hadad, "Beyond the Bode-Fano Bound: Wideband Impedance Matching for Short Pulses Using Temporal Switching of Transmission-Line Parameters," *Phys. Rev. Lett.*, vol. 121, p. 204301, Nov 2018.

[96] G. Ptitcyn, M. S. Mirmoosa, and S. A. Tretyakov, "Time-Modulated Meta-Atoms," *Phys. Rev. Res.*, vol. 1, p. 023014, Sep 2019.

[97] C. Caloz and Z.-L. Deck-Leger, "Spacetime MetamaterialsâPart I: General Concepts," *IEEE Trans. Antennas Propag.*, vol. 68, no. 3, pp. 1569–1582, 2020.

[98] V. Pacheco-Peña and N. Engheta, "Antireflection Temporal Coatings," *Optica*, vol. 7, no. 4, pp. 323–331, 2020.

[99] V. Pacheco-Peña and N. Engheta, "Spatiotemporal Isotropic-to-Anisotropic Meta-Atoms," *New J. Phys*, vol. 23, p. 095006, Sep 2021.

[100] X. Wang, V. S. Asadchy, S. Fan, and S. A. Tretyakov, "Space-Time Metasurfaces for Power Combining of Waves," *ACS Photon.*, vol. 8, no. 3, pp. 3034–3041, 2021.

[101] Z. Wu, C. Scarborough, and A. Grbic, "Space-Time-Modulated Metasurfaces with Spatial Discretization: Free-Space N-Path Systems," *Phys. Rev. Appl.*, vol. 14, p. 064060, 2020.

[102] N. Engheta, "Metamaterials with High Degrees of Freedom: Space, Time, and More," *Nanophotonics*, vol. 10, no. 1, pp. 639–642, 2021.

[103] P. Huidobro, M. Silveirinha, E. Galiffi, and J. Pendry, "Homogenization Theory of Space-Time Metamaterials," *Phys. Rev. Appl.*, vol. 16, p. 014044, Jul 2021.

[104] A. Darabi, X. Ni, M. Leamy, and A. Alù, "Reconfigurable Floquet Elastodynamic Topological Insulator Based on Synthetic Angular Momentum Bias," *Sci. Adv.*, vol. 6, no. 29, 2020.

[105] R. Fleury, A. Khanikaev, and A. Alu, "Floquet Topological Insulators for Sound," *Nat. Commun.*, vol. 7, no. 12, p. 11744, 2016.

[106] V. Bacot, M. Labousse, A. Eddi, M. Fink, and E. Fort, "Time Reversal and Holography with Spacetime Transformations," *Nature Phys.*, vol. 12, no. 12, pp. 972–977, 2016.

[107] A. K. Kamal, "A Parametric Device as a Nonreciprocal Element," *Proc. IRE*, vol. 48, no. 8, pp. 1424–1430, 1960.

[108] B. Anderson and R. Newcomb, "On Reciprocity and Time-Variable Networks," *Proceedings of the IEEE*, vol. 53, no. 10, pp. 1674–1674, 1965.

[109] A. Cullen, "Theory of the Travelling-Wave Parametric Amplifier," *Proc. IEE, B Electron. Commun. Eng. UK*, vol. 107, no. 32, p. 101, 1960.

[110] E. Cassedy, "Waves Guided by a Boundary with Time-Space Periodic Modulation," *Proc. Inst. Electr. Eng. UK*, vol. 112, no. 2, p. 269, 1965.

[111] A. Kord, D. L. Sounas, and A. Alu, "Magnet-Less Circulators Based on Spatiotemporal Modulation of Bandstop Filters in a Delta Topology," *IEEE Trans. Microw. Theory. Tech.*, vol. 66, no. 2, pp. 911–926, 2018.

[112] X. Wang, G. Ptitcyn, V. S. Asadchy, A. Diaz, M. S. Mirmoosa, S. Fan, and S. A. Tretyakov, "Nonreciprocity in Bianisotropic Systems with Uniform Time Modulation," *Phys. Rev. Lett.*, vol. 125, p. 266102, Dec 2020.

[113] M. Mirmoosa, G. Ptitcyn, V. Asadchy, and S. Tretyakov, "Time-Varying Reactive Elements for Extreme Accumulation of Electromagnetic Energy," *Phys. Rev. Appl.*, vol. 11, p. 014024, Jan. 2019.

[114] D. L. Sounas, "Virtual Perfect Absorption Through Modulation of the Radiative Decay Rate," *Phys. Rev. B*, vol. 101, p. 104303, Mar 2020.